UNIVERSITY OF CALIFORNIA
RIVERSIDE

Multifunctional Fiber-Reinforced Composites Inspired by the Shell of a Bioluminescent Marine Gastropod

A Dissertation submitted in partial satisfaction
of the requirements for the degree of

Doctor of Philosophy

in

Chemical and Environmental Engineering

by

Christopher Louis Salinas

March 2016

Dissertation Committee:
Dr. David Kisailus, Chairperson
Dr. Ruoxue Yan
Dr. Cheryl Hayashi

The Dissertation of Christopher Louis Salinas is approved:

_____

_____

_____

Committee Chairperson

University of California, Riverside

ACKNOWLEDGEMENTS

This research is sponsored in part by the NASA space grant, UCR dissertation year fellowship, and AFSOR during the duration of the dissertation research.

I would like to acknowledge my advisor, Dr. David Kisailus, for his support and insights over the many years. I would like to thank my lab mates and collaborators, for the many thoughtful discussions on the structure and nature of biomineralized materials. In particular I would like to thank the Steven Herrera, Nicholas Yaraghi, and Dr. Garret Milliron, for the many late discussion on the mechanics of natural materials. This work would not have been possible without the help of Dr. Dimitri Deheyn who provided *Hinea brasiliana* specimens.

I would also like to thank my father and mother, Lou and Vicki Salinas, who have worked hard to allow me this great opportunity along with their unwavering support through all my academic adventures.

ABSTRACT OF THE DISSERTATION

Multifunctional Fiber-Reinforced Composites Inspired by the Shell of a Bioluminescent Marine Gastropod

by

Christopher Louis Salinas

Doctor of Philosophy, Chemical and Environmental Engineering
University of California, Riverside, March 2016
Dr. David Kisailus, Chairperson

Due to increasing predatory pressure over hundreds of millions of years, gastropods have evolved hard calcified shells with novel microstructures to increase the toughness of their shells and to protect their soft body. Initially, prismatic forms of these shells were dominant, which evolved to layered nacre-like structures. However, during the Mesozoic marine revolution (~250MYa) this arms race between gastropods and durophagus predators, yielded the evolutionary newest shell structure, the crossed lamellar microstructure. This structure arose as the dominant shell architecture found in the majority of the 60,000 extant specimens of gastropods. The primary advantage of this structure was that it enabled toughening, four orders of magnitude greater than the mineral from which it is constructed, calcium carbonate. The crossed lamellar structure also allowed for the diversification of shell morphologies, resulting in a range of adaptations to further the success of gastropods in many different ecological niches. A very recent anti-predation adaption (<50MYa) that has occurred in the gastropod Hinea

brasiliana is the ability to bioluminesce and diffuse the produced light over the surface of their shell. We investigated the ultrastructure and optical properties of the shell of *H.brasiliana* and to uncover the structural origins of the optical diffusion and found *H.brasiliana* shell to be typical for caenogastropoda. The diffusion of light in the shells of numerous other non-luminescent gastropods were studied, in which pigmentation is In addition we investigated the anisotropy in the indentation fracture properties of the crossed lamellar structure using nanoindentation. We used these design cues obtained to develop multifunctional fiber-reinforced composites with tunable mechanical and optical properties.

Table of Contents

Table of Figures

1. Utilizing Mollusk Shells for Tougher Composites

Abstract

The need to protect soft vulnerable vital organs from damage is a common problem amongst most organisms. While *Homo sapiens* have been making hard rigid armors for few thousands of years, gastropods have been evolving tough armors to defend themselves and thrive against numerous predators for many millions of years. In the early Cambrian period (544 to 485.4 mya), mollusks gained mineralized shells and soon thereafter, during the Cambrian explosion when durophagous predators began to appear, gastropods shell microstructures evolved into both the nacreous and the crossed Lamellar architectures. Later, during the Mesozoic marine revolution (300 to 250 mya), there was an arms race between predator and prey. As predators became more sophisticated and stronger, the crossed lamellar architecture of gastropod shells became dominant, and thus, numerous adaptions evolved to resist the threats of increasingly more capable predators.

1.1. Introduction

For thousands of years, humans have developed a wide range of structural materials designed as armor to withstand impacts sustained during battle. From the development of *Lorica segmentata* worn by the Roman Legions in the 1st century A.D., the steel Cuirass worn during the Middle Ages to present day armor that utilizes advanced polymer-ceramic technologies (Figure 1-1), the strategy has

been to employ a hard external casing backed by an energy absorbing layer. However, these composites still fail under specific loading conditions. Take for example, the Small Arms Protective Insert (SAPI), a standard issue of the U.S. Army for body armor (Figure 1-1 d). Although this SAPI plate was designed to withstand impact from a high velocity round, it is inherently weak (note the “handle with care” label).

Figure 1-1 Roman Segmentata armor from 1st century (a)(*1*). French Cuirass 1800’s (b)(*1*) Modern plate carrier 2000’s (c)(*1*) SAPI insert for plate carrier (d)(*1*).

Although humans have been struggling to develop optimized composite materials, organisms have utilized the past few hundreds of millions of years to evolve new structures designed for specific functions. Mammals, arthropods, and mollusks have all developed hard and tough defensive structures for protection against predation. One specific class within the Mollusca phylum, the gastropods (snails and slugs) have developed the ability to survive in a diverse range of ecological niches through hundreds of millions of years of evolution, initially spurred by the diversification of durophagous predators during the Mid-Paleozoic revolution, 400-500 million years ago (mya) (*2*). These snails are both terrestrial

and aquatic, being found in both marine and fresh waters. The largest diversity of gastropods is found in the oceans, where evolutionary pressures have yielded calcified shells with a broad range of architectural features.

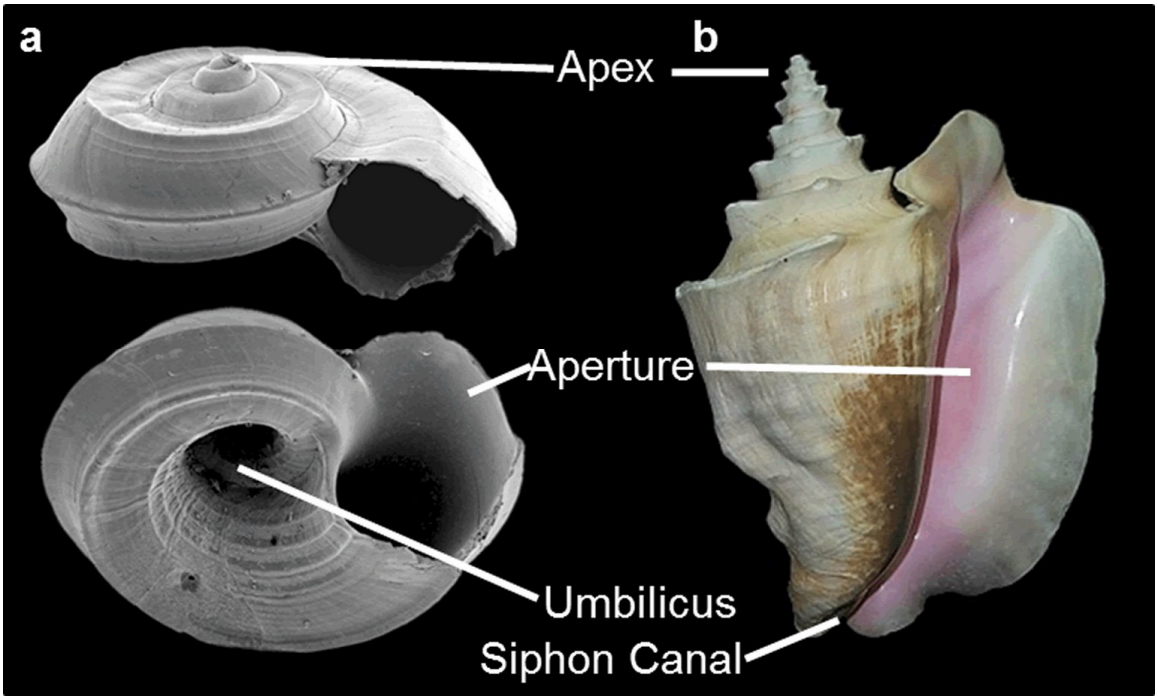

Figure 1-2 Planispiral *Cyclostremiscus mohicanus*, with umbilicus present (*3*)(a). High-spire *Strombus gigas*, not the lack of umbilicus and extensive broadening of the aperture and ribbing on the exterior of the shell (*4*)(b).

Gastropod external shells have afforded greater protection in response to a significant increase in different modes of predation: smashing, drilling, crushing, and being consumed whole. Mollusks developed hard structures early in the Paleozoic period (550-250 mya) (*5*). Archaeogastropods flourished during the Paleozoic period; their shells were frequently larger, broader, planispiral, and contained an umbilicus, the gap at the base of the shell where whorls do not fully overlap (Figure 1-2 a) (*5*). During the Mesozoic period (250 – 65 mya), a vast diversification of gastropods and gastropod-based predators was observed, and

has subsequently been termed the Mesozoic Marine Revolution (*5*). The shells of the now highly dominant mesogastropods and neogastropods are typically tightly coiled, high-spired, sculpted, and lacking an umbilicus (Figure 1-2 b). Gastropods with the planispiral shell structure are greatly reduced in size and typically found in environments without shell-crushing predators (*5*). The absence of an umbilicus and an increased frequency and variety of shell sculptures have resulted from an increased ability to remodel the interior structures of the shell, enabling the formation of shells with short spires, narrow apertures, strong external sculptures, and an apertural dentition. The shells of archaeogastropods lacked many of these geometrical defensive features (*5*).

Gastropod shells are primarily composed of an aragonitic calcium carbonate as well as minor secondary organic phases. In order to overcome the brittle nature of the calcium carbonate, the shells are composed of fracture mitigating structures, with features spanning from the nano- to the macro-scale (*6, 7*). Investigations into the micro and nanostructural aspects of these hierarchically assembled biological composites have revealed a wide variety of structures and provided insight into the evolutionary pressures and behavior of different species. The shells are most commonly composed of either nacreous or crossed-lamellar microstructures. The nacreous structure was shown to be mechanically superior (*8*), but is a more ancient structure and only occurs in archaeogastropods. Here, we describe how this “primitive” structure affords mechanical superiority by examining the different design strategies used in these two materials, and what

lessons can be gleaned for the development of advanced ceramics and composites. We also discuss attempts at mimicking these structures and what remains to be achieved.

1.2. Nacre

Nacre is a biological composite that exhibits a brick and mortar architecture (Figure 1-3) and consists of ~ 95% stiff aragonitic tablets, and 5% organic macromolecules (polysaccharides and polypeptides) found between (*9*) and recently, within the mineral (*10*). Nacre is found in two varieties: columnar nacre (found in marine gastropods such as the red abalone) and sheet nacre (commonly occurring in fresh water bivalves) (*11*). In columnar nacre, the edges of mineral tablets are aligned in alternating layers whereas the edges of mineral tablets in sheet nacre are randomly distributed (Figure 1-3 b). The mechanical properties of nacre have been studied using various loading methods and different strain rates. These investigations have revealed the underlying mechanism responsible for the dramatic increase in the ductility of nacre, while retaining the majority of the hardness and elastic modulus of aragonite. It is not the simple brick and mortar nature of the nacreous structure that affords it superior mechanical properties, but rather a combination of nano- and micro-structural features (that have yet to be duplicated in mimetic systems) that make this inherently brittle material incredibly tough. Typically when the shells are loaded (e.g., during an impact from a predator), the nacreous layer is exposed to tensile stresses. In this mode of loading, tablets in nacre will slide past each other, providing the primary

mechanism for energy dissipation. The resulting structure of nacre has an elastic modulus of approximately 60-75 GPa (*12*) (*13*) and a work of fracture (WOF) 3 orders of magnitude greater than geologic aragonite (1,240 J m^{-2} (*12*) and 1,650 J m^{-2} (*14*)). During the mineralization process of the nacreous structure, polysaccharides (*i.e.*, ß-chitin fibrils) (*9*) are secreted with acidic polypeptides (*15*). These organics provide a framework that templates the nucleation and guides the growth of mineral. The organic subsequently gets incorporated within the nacreous structure, surrounding each tablet, and provides a softer interface between tablets, effectively redirecting cracks penetrating through the structure. Thus, this brick and mortar structure provides a tougher composite (versus the bulk material) due to a large fraction of mineral-organic interfaces. The polyhedral mineral tablets, composed of 32 nm (*16, 17*) crystallites of $CaCO_3$, are 200 – 300 nm thick and are 10 - 15 µm in diameter (*8*). A number of nano and microstructural features have been revealed over the past 40 years (*17, 18*) that may provide significant toughening beyond the aforementioned interfaces. The surfaces of the tablets are rough, covered in nanoscale mineral “bumps” known as asperities (Figure 1-3 c)(*18*). Asperities that grow into a tablet above are known as mineral bridges (*18*) and provide a pathway for crystallographic alignment (*i.e.*, tablets stacked on each other have the same c-axis orientation). Recent investigations of the nacreous structure revealed that the tablets are not flat (*19*), but that their thickness varies from one end of the tablet to the other (*i.e.*, tablets are wavy). This wavy structure

leads to an interlocking (Figure 1-3 d) with adjacent layers and provides another level of toughening (*20, 21*).

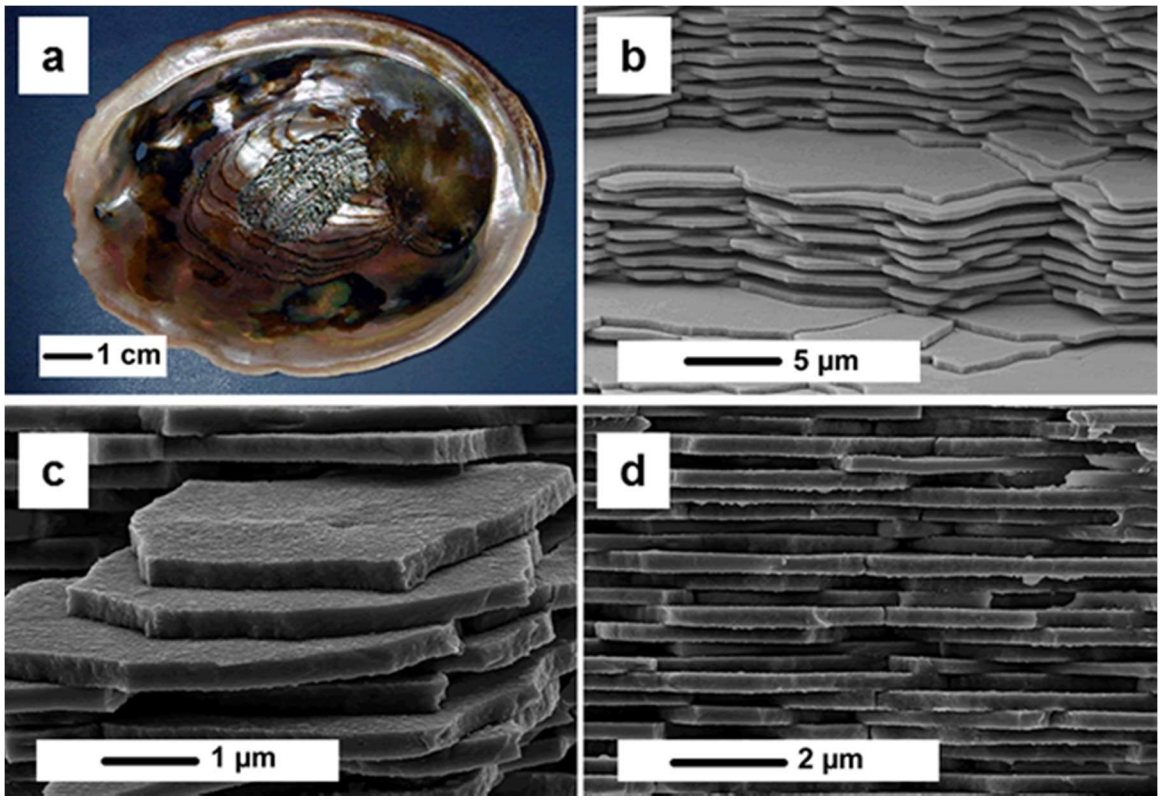

Figure 1-3 California red abalone (*Haliotis rufescens*) with pearlescent interior of nacre (a). Fracture surface of nacre, displaying the well-organized brick and mortar structure (b). The surface of nacre tablets is not smooth, and features mineral asperities (c). The tablets show a slight waviness, being thicker on the edges than in the middle (d).

Before the tablets can slide past each other, they first must sever the mineral bridges that link one tablet to another (either directly above or below). This provides a stiff linkage until displacements of 15-20 nm (*22*) afford failure of these bridges (*18*). In addition to the mineral bridges, incompletely formed bridges (*i.e.*, asperities) afford the tablet surface with a high level of nano-roughness. These 10 – 30 nm mineral asperities are distributed across the surface of the tablets, providing increasing resistance until a critical loading point - after which they

provide constant resistance (*13*). The minor dove-tailing or waviness (*19*) of the tablets causes an increase in the inter-tablet forces as the tablets are displaced from one another (*23*). At greater displacements, the organic macromolecules found between tablets begin to unfold (*24*). In addition, these inter-lamellar organics act to redirect cracks propagating through brittle tablets, effectively dissipating more energy. Finally, the macroscopic arrangement of the shell is designed for protection, with the hard exterior of prismatic calcite, providing protection against puncture, and a tough interior of aragonite (nacre) to dissipate energy (*6, 25*).

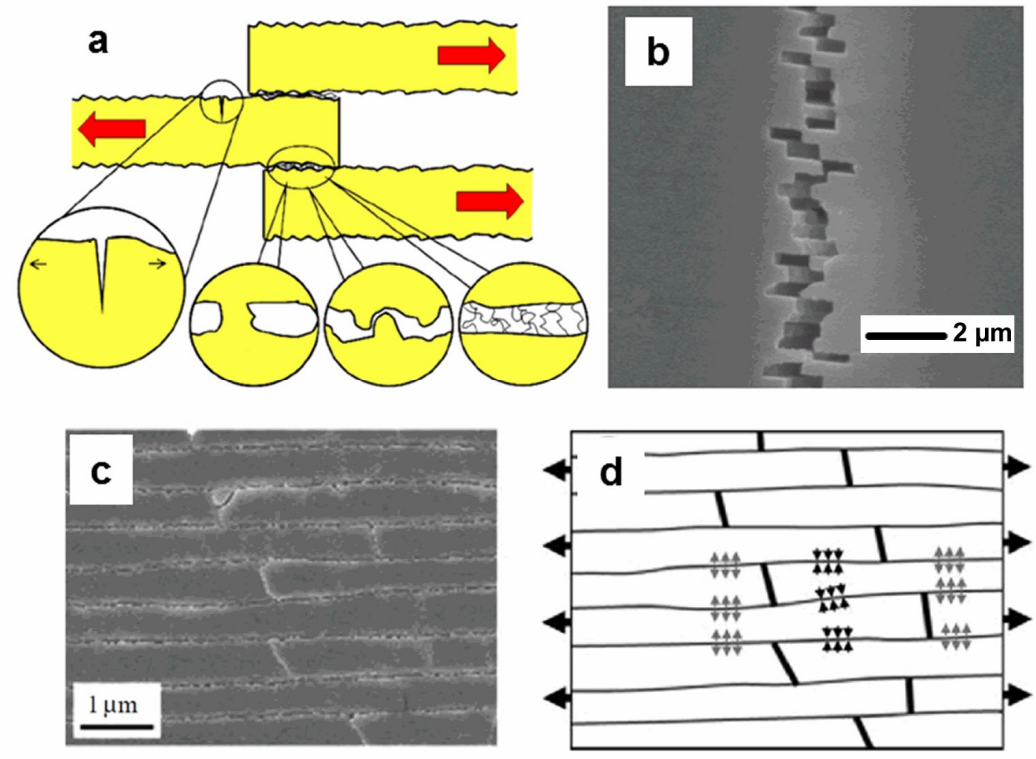

Figure 1-4 Four possible mechanisms for energy release for tablets in shear (in increasing energy required): (i) Fracture of aragonitic tablets, (ii) severing of mineral bridges, (iii) tablet sliding over surface asperities, and (iv) shearing of the organic matrix (*26*) (a). Resulting tablet pull out from nacre specimen under tension (*26*) (b). Role of dove-tailing to delocalize strain, and produce progressive hardening (*19*)(c). Schematic of vertical displacement due to shearing (*19*) (d).

1.3. Crossed-Lamellar

In addition to the nacreous structure, gastropods have been found to have a crossed-lamellar structure. The crossed-lamellar structure is comprised of sub-micron aragonitic planks embedded in an organic matrix whose overall structure resembles that of plywood. It is the most common microstructure, found in 90% of living gastropods (*27*). It is a hierarchical structure, consisting of five distinct levels of ordering (*28*). The shells are typically constructed of multiple laminated layers, commonly the outer, middle, and inner layers. Each layer is composed of 1st-order lamellae in which the direction of each layer varies (0° - 90° - 0°) from each other (*29*) (Figure 1-5 a). The 1st order lamellae are further composed of 2nd order lamellae that alternate direction (± 45°) between adjacent 1st order lamellae (*30*). The 2nd order lamellae are further composed of single crystal aragonitic planks that are 200nm wide by several microns in length (3rd order) (*31*) (Figure 1-5 d). The 3rd order lamellae are coated with a thin (1 - 2nm) organic layer (conchiolin) (*32*), which is likely utilized as a framework or scaffold during biogenic synthesis. The higher order structures (*i.e.*, 1st and 2nd order) do not seem to contain additional organic coatings at their interfaces (*28*), however further investigation is needed to confirm this. The 3rd order lamellae have been shown to consist of a finely twinned structure. Younis *et al.* (*28*) showed that the 3rd order lamellae are formed from 4th order nanoplatelets. Unlike the organic material found within nacre tablets, there

has since been no evidence for the presence of organic within the 3rd order lamellae. However, this may be limited by the current characterization techniques.

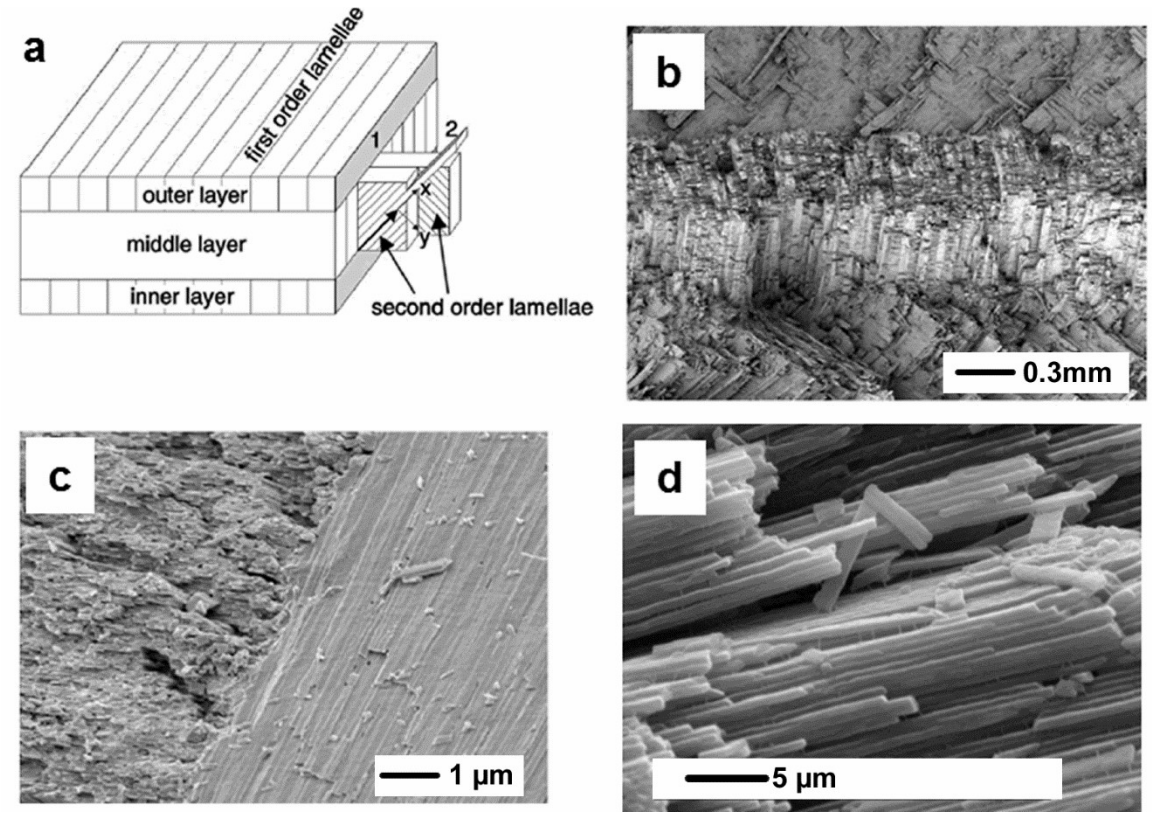

Figure 1-5 Crossed lamellar structure is composed of multiple layers of varying 1st order direction (*30*) (a). The outer and inner layer are perpendicular to the middle layer, the 1st order lamellae in the middle layer are clearly visible (*30*) (b). The 2nd order lamellae in two adjacent 1st order lamellae are approximately perpendicular to each other, and composed of 3rd order plank-like lamellae (*30*) (c). 3rd order lamellae are smooth and rectangular (d).

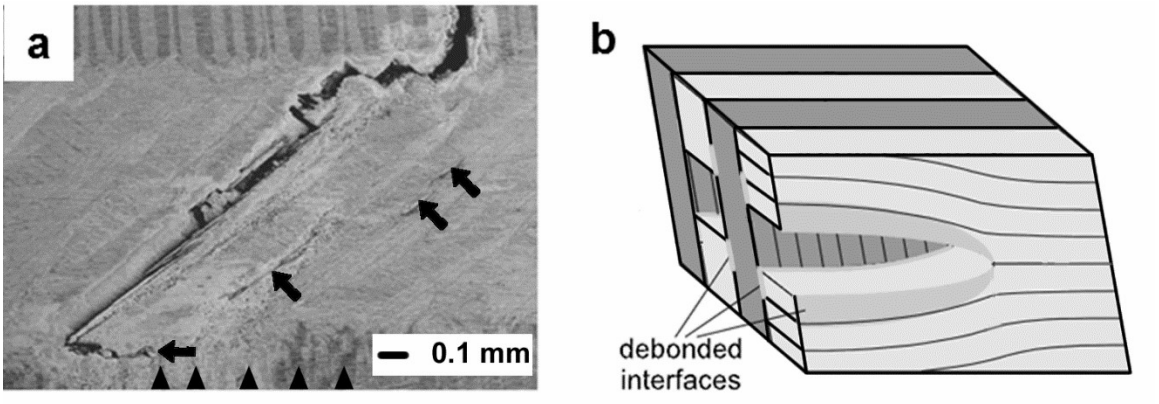

Figure 1-6 Crack is shown traveling straight through the "weak" direction and being deflected within the next shell macro layer (*30*) (a). As a crack delaminates the 2nd order lamellae (light grey), the adjacent lamellae bridge the gap (dark gray), providing resistance to fracture propagation adapted from (*30*) (b).

The mechanical properties in a variety of crossed-lamellar gastropod species have been investigated (*8, 29, 30*) (*33-36*) (*37-39*). During loading (e.g., from an impacting predator), the primary mode of energy dissipation is in the redirection/generation of cracks within the shell. As a growing crack approaches an aragonitic plank it can either (i) travel along the length of the planks, causing them to delaminate (*i.e.*, weak/easy direction of propagation) or (ii) propagate through the lamella causing brittle fracture. As cracks propagate through lamellae, the material is able to maintain its structural integrity via crack bridging (*29, 30*). The toughness of the macroscopic layers alternates from weak to tough and back to weak. The resulting laminated structure, comprised of alternating directions of planks, can cause crack redirection at the interfaces, because each of the shell layers is perpendicular to the adjacent layer. Thus, when a crack propagates along the easy direction of one layer, it is redirected at the interface of the next layer. In the other case, when cracks propagate through 1st order lamellae, the fracture

surface consist of an alternating rough and then smooth pattern, from the fracturing through and the delamination of 2nd order lamella respectively (*30*). The orientation and arrangement of the 1st order lamellae and the macroscopic layering within the shell are responsible for the enhancement of the enhanced work of fracture over a monolithic material (*30*).

There are multiple energy dissipation mechanisms within crossed-lamellar shells that contribute to the observed superior work of fracture. Kamat *et al.* modeled the role of multiple "tunnel" cracks formed in the weak inner layers of the *Strombus gigas* (queen conch) shell and identified that the cracks are formed with relatively low total loads, and could only account for a fraction of the total energy required to fracture the shell (*30*). The tunnel cracks form at the 1st order lamellar interfaces within the weak layer, and propagate until the crack reaches the interface of the tough middle layer (Figure 1-6 a), after which new tunnel cracks are generated within the weak layer (*30*). The work of fracture and the crack density at failure are correlated to the ratio of the toughness of the "tough" layer to the weak layer (*39*). To produce multiple tunnel cracks within the weak inner layer, the ratio of toughness between the layers must be greater than 2 (*30*). The toughness ratio for the crossed-lamellar structure within *Strombus gigas* has been experimentally determined to be between 2.5-3.0 (*29, 30*). The formation of multiple tunneling cracks in the weak layer is responsible for an order of magnitude increase in toughness. The toughness gained from the formation of multiple tunnel cracks due to a difference in layer strengths is limited by the crack density

saturation, which inhibits the formation of new tunnel cracks within the layer (*30*). To understand the mechanism of tunnel crack formation, Kamat *et al.* modeled the shell as a bilayer composite with both weak and tough layers.

Within the tough middle layer, crack bridging and microcracking are responsible for a significantly greater amount of the dissipated energy during fracture. When a fracture propagates through the middle layer, it travels between the 2nd order lamellae, causing them to delaminate (Figure 1-6 b). The other direction of 2nd order lamellae bridge the fracture, providing resistance to growth of the fracture, until these bridging lamellae fail in a manner similar to the fiber pullout mechanism commonly observed in composites (*30*) (*40-42*). Furthermore, the physical properties controlling the bridging of the fracture are such that they avoid the critical stress suggested by Aveston-Cooper-Kelly (*43*), which determines when catastrophic failure occurs. Kamat *et al.* modeled the effect of multiple tunneling cracks in the weak layer and fracture bridging in the tough layer to produce a toughness 330 times greater than aragonite alone (*30*).

The crossed-lamellar structure is the most prevalent microstructure in gastropods and is found in shells that display a wide variety of shell morphologies. However, due to the complexity of the microstructure, there is a lack of information regarding the mechanical and physical properties of these shells. Many of the shells that have been investigated are quite large, such as in *Strombus gigas*, so that suitable test specimens can be produced from a uniform region. However, the smaller (and more numerous) shells provide new challenges for mechanical testing

and crystallography. The crossed-lamellar structure is once again able to retain the rigidity of calcium carbonate, while allowing for inelastic deformation within the structure. The two main mechanisms responsible for this are multiple tunnel crack formation within the weak layers and crack bridging within the middle layer.

1.4. Biomimetics

For millennia, humans have been utilizing the unique physical properties of biomaterials for the production of tools and body armor. Currently, engineering ceramics are typically very strong but very brittle. Yet, for hundreds of millions of years, gastropods have been evolving shells also using brittle components but assembling these into complex microstructures with multiple interfaces to overcome these material limitations. By applying the novel designs and toughening mechanisms found in gastropods along with modern high strength ceramics, it is possible to develop a new generation of ceramics that are both strong and tough. A number of efforts have been made to replicate the micro/macro structural elements found in both nacre and crossed-lamellar structures, which will be described below.

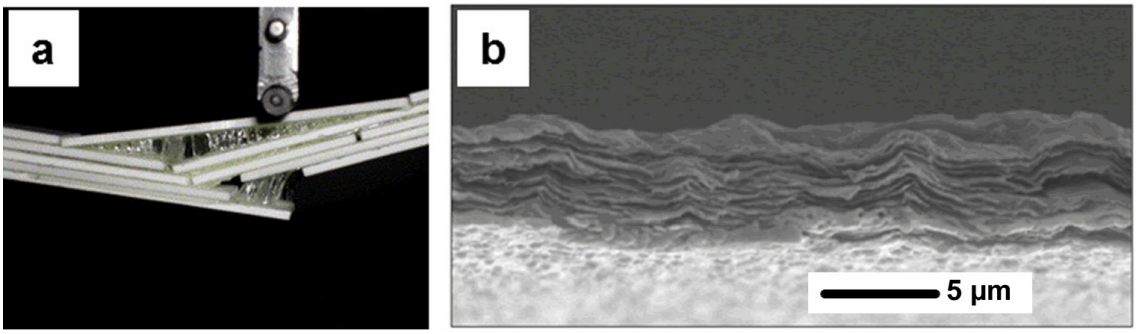

Figure 1-7 Millimeter scale hard ceramic plates bonded with a weak interface that mimic the crack deflection observed in nacre (*44*) (a). Well-aligned clay tablets, produced through repeated electrostatic deposition (*45*) (b).

The brick and mortar structure of nacre, with its initial appearance as a rather simplistic and uniform design, has been mimicked at many different length scales. Rim *et al.* determined the optimal geometry of platelet-reinforced composites that mimic the mechanical properties of nacre (*46*). Laminates composed of rather large ceramic tiles have been used to study effect of the interfacial strength (*47, 48*) (*12, 44*). Clegg (*47, 48*) used silicon carbide plates as the mineral tablets and graphite to simulate a weak inter-tablet interface, cracks where extensively deflected increasing the fracture toughness from 3.6 $MPa \cdot m^{1/2}$ to 17.7 $MPa \cdot m^{1/2}$. Espinosa *et al.* (*49*) produced artificial nacre from ABS using rapid prototyping. In their model, they were able to incorporate slight dovetailing on the tablets to simulate the interlocking waviness found in natural nacre. The authors were thus able to determine the effects of tablet aspect ratio (length to thickness) and θ (dovetail angle) during material failure due to softening/pullout, brittle fracture, or hardening/fracture (as in nacre).

To produce mimics with smaller tablet sizes, approaching the 200 nm thick x 10 μm diameter tablets found in nacre, significant challenges are presented in precise control of tablet alignment and position. In addition to platelet alignment, achieving relatively high inorganic loading and even dispersion of the organic material has proved quite difficult. A number of studies have been performed to deposit tablet-like materials in an organized structure using a layer-by-layer approach (*45, 50-53*). Montmorillonite clay tablets (MMT) have been used in electrostatic layer-by-layer deposition with polyelectrolytes (*45*),. The clay tablets and polyelectrolyte are deposited in alternating layers through a cyclic dip coating process. Due to the high aspect ratio of the tablets, the large facets of the platelets aligned parallel to the substrate surface, maximizing their attractive forces. When tested in tension, the composite material underwent plastic deformation followed by hardening; this was attributed to the initial unraveling of the polymer phase, followed by debonding.

A bottom up approach has been used to template the nacre structure (*54-56*). Deville *et al.* used ice templating to form a laminated porous alumina structure, which was subsequently infilled with epoxy. Their resulting structure was able to replicate the mineral bridges found in between layers in nacre, and demonstrated an ability to tune the dimensions of the pores in the scaffold by controlling the freeze rate (*55*).

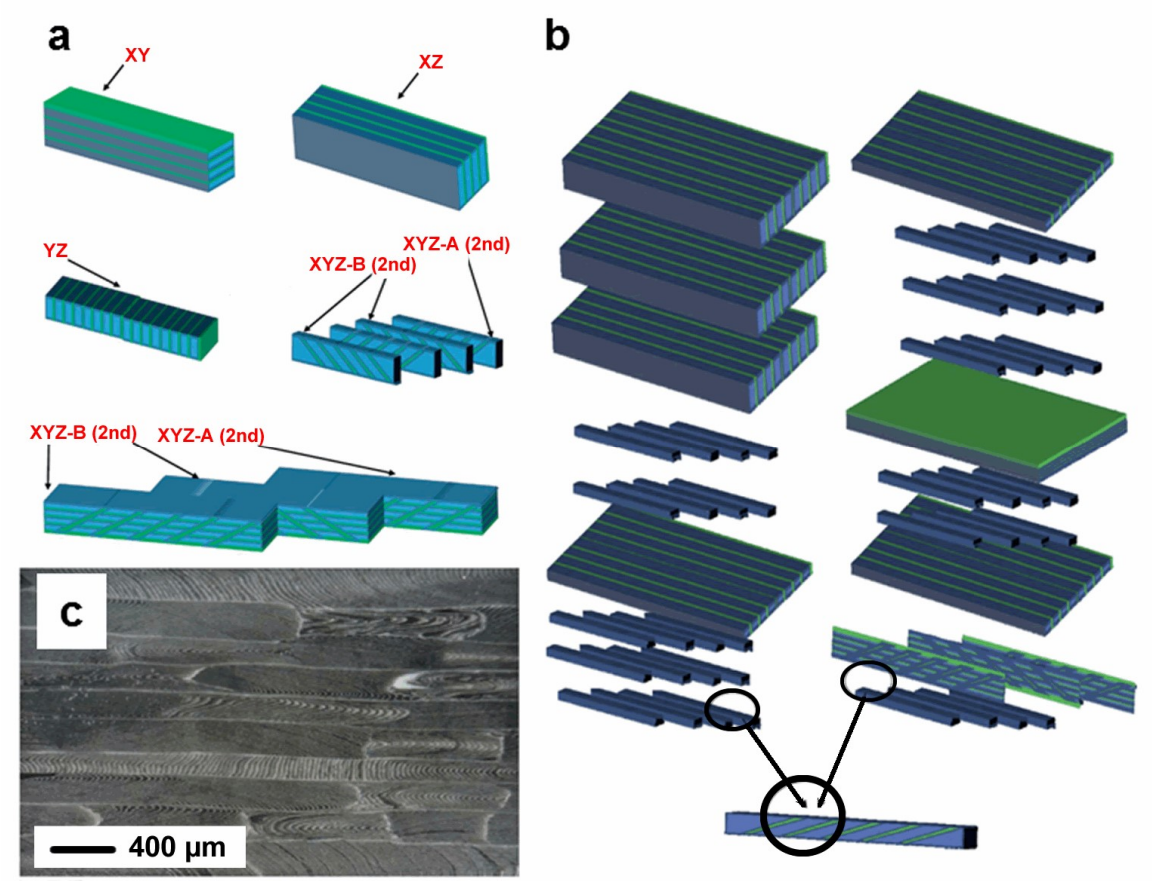

Figure 1-8 Orientation of Si_3N_4 and h-BN laminates (*57*) (a). Test microstructures of Si3N4 and h-BN laminated composites (*57*) (b). Resulting microstructure with rectangular 1st order lamellae and 2nd order features visible (*57*) (c).

The crossed-lamellar structure has many fundamental similarities to fiber-reinforced composites, with the 1st order lamella arranged as a bi-directional laminate. Attempts to replicate multiple hierarchical elements of the crossed-lamellar structure are rather limited. The 1st and 2nd order structures, along with inner middle and outer ultrastructures, were created using MEMS fabrication techniques (*58*). Chen *et al.* fabricated mimics from polysilicon and photoresist to simulate the aragonitic and organic structures found in crossed lamellar shells. A 36-fold increase in ductility was observed, primarily due to crack bridging in the

middle layers. However, due to limitations in fabrication of the 3rd order lamellae, channel cracks failed to form and instead, delamination was observed. Karamabelas *et al.* (*57*) produced a more complete mimic of the architecture of *Strombus gigas*, which they have deemed “Sequential Hierarchical Engineered Layer Lamination” or SHELL. They used a co-extruded Si_3N_4 and h-BN to simulate the aragonite and organic, to produce laminated structures, that were then furthered sectioned, aligned, and laminated to produce a final assembly (Figure 1-8). Using this method, they were able to produce multiple macroscopic layers with up to 3 orders of internal hierarchy that displayed significant increases in work of fracture compared to fibrous monolithic Si_3N_4/h-BN (3620 J m^{-2} compared to 2860 J m^{-2} for fibrous monolithic Si_3N_4/h-BN). In addition the structures showed remarkable damage tolerance (DT-50 of 0.79 for the biomimetic compared to 0.095 for monolithic Si_3N_4).

The crossed-lamellar architecture possesses formidable challenges for composite mimics, due to the complexity and multiple levels of hierarchical design. The limited mimetic structures that have been produced have shown that consideration must be given to both the construction of individual layers of material and the positioning of those layers.

The beauty of nature has inspired man for millennia, modern characterization advancements has revealed that this beauty is not just skin deep. Through millions of years of the evolutionary process nature has created composites which exhibit a large degree of complexity. By understanding the

architectures by which these inherently weak materials achieve such outstanding physical properties, we can begin to construct materials that meet or exceed the benchmark set by nature using engineered materials. However, the ultimate challenge still remains to guide this architecture at the length scales and complexity that Nature utilizes.

1.5. Outlook

The crossed lamellar microstructure is the most common shell microstructure of found in gastropods, which are currently the most abundant and diverse clade within Mollusca. However this microstructure is uncommonly investigated, and even more rarely mimicked for engineering applications. Crossed lamellar structures offer many evolutionary adaptations to study. We investigate the optical and mechanical properties in light of new insights into the structure and nature of the material.

References

1. C. Salinas, D. Kisailus, Fracture Mitigation Strategies in Gastropod Shells. *Jom-Us* **65**, 473-480 (2013).

2. P. W. Signor III, C. E. Brett, The mid-Paleozoic precursor to the Mesozoic marine revolution. *Paleobiology*, 229-245 (1984).

3. A. Kouchinsky, Shell microstructures in Early Cambrian molluscs. *Acta Palaeontol Pol* **45**, 119-150 (2000).

4. C. Salinas, D. Kisailus, Fracture Mitigation Strategies in Gastropod Shells. *Jom-Us* **65**, 473-480 (2013).

5. G. J. Vermeij, The Mesozoic marine revolution: evidence from snails, predators and grazers. *Paleobiology*, 245-258 (1977).

6. M. Sarikaya, I. A. Aksay, "Biomimetics. Design and Processing of Materials," (DTIC Document, 1995).

7. G. Mayer, Rigid biological systems as models for synthetic composites. *Science* **310**, 1144-1147 (2005).

8. J. Currey, J. Taylor, The mechanical behaviour of some molluscan hard tissues. *J Zool* **173**, 395-406 (1974).

9. Y. Levi-Kalisman, G. Falini, L. Addadi, S. Weiner, Structure of the nacreous organic matrix of a bivalve mollusk shell examined in the hydrated state using cryo-TEM. *Journal of structural biology* **135**, 8-17 (2001).

10. M. Rousseau *et al.*, Multiscale structure of sheet nacre. *Biomaterials* **26**, 6254-6262 (2005).

11. S. W. Wise, *Microarchitecture and mode of formation of nacre (mother of pearl) in pelecypods, gastropods, and cephalopods*. (Birkhäuser, 1970).

12. A. Jackson, J. Vincent, R. Turner, The mechanical design of nacre. *Proceedings of the Royal society of London. Series B. Biological sciences* **234**, 415-440 (1988).

13. R. Wang, Z. Suo, A. Evans, N. Yao, I. Aksay, Deformation mechanisms in nacre. *J Mater Res* **16**, 2485-2493 (2001).

14. J. Currey, Mechanical properties of mother of pearl in tension. *Proceedings of the Royal Society of London. Series B. Biological Sciences* **196**, 443-463 (1977).

15. R. A. Metzler *et al.*, Probing the organic-mineral interface at the molecular level in model biominerals. *Langmuir* **24**, 2680-2687 (2008).

16. A. G. Checa *et al.*, Crystallographic control on the substructure of nacre tablets. *Journal of structural biology* **183**, 368-376 (2013).

17. X. Li, W.-C. Chang, Y. J. Chao, R. Wang, M. Chang, Nanoscale structural and mechanical characterization of a natural nanocomposite material: the shell of red abalone. *Nano Lett* **4**, 613-617 (2004).

18. F. Song, A. K. Soh, Y. L. Bai, Structural and mechanical properties of the organic matrix layers of nacre. *Biomaterials* **24**, 3623-3631 (2003).

19. F. Barthelat, Biomimetics for next generation materials. *Philos Trans A Math Phys Eng Sci* **365**, 2907-2919 (2007).

20. K. S. Katti, D. R. Katti, S. M. Pradhan, A. Bhosle, Platelet interlocks are the key to toughness and strength in nacre. *J Mater Res* **20**, 1097-1100 (2005).

21. K. S. Katti, D. R. Katti, Why is nacre so tough and strong? *Materials Science and Engineering: C* **26**, 1317-1324 (2006).

22. A. Evans *et al.*, Model for the robust mechanical behavior of nacre. *J Mater Res* **16**, 2475-2484 (2001).

23. F. Barthelat, H. Tang, P. Zavattieri, C. Li, H. Espinosa, On the mechanics of mother-of-pearl: A key feature in the material hierarchical structure. *J Mech Phys Solids* **55**, 306-337 (2007).

24. B. L. Smith *et al.*, Molecular mechanistic origin of the toughness of natural adhesives, fibres and composites. *Nature* **399**, 761-763 (1999).

25. P. Fratzl, Biomimetic materials research: what can we really learn from nature's structural materials? *J R Soc Interface* **4**, 637-642 (2007).

26. A. Y.-M. Lin, M. A. Meyers, Interfacial shear strength in abalone nacre. *J Mech Behav Biomed* **2**, 607-612 (2009).

27. B. Pokroy, E. Zolotoyabko, Microstructure of natural plywood-like ceramics: a study by high-resolution electron microscopy and energy-variable X-ray diffraction. *J Mater Chem* **13**, 682-688 (2003).

28. S. Younis, Y. Kauffmann, B. Pokroy, E. Zolotoyabko, Atomic structure and ultrastructure of the Murex troscheli shell. *Journal of structural biology* **180**, 539-545 (2012).

29. S. Kamat, X. Su, R. Ballarini, A. H. Heuer, Structural basis for the fracture toughness of the shell of the conch Strombus gigas. *Nature* **405**, 1036-1040 (2000).

30. S. Kamat, H. Kessler, R. Ballarini, M. Nassirou, A. H. Heuer, Fracture mechanisms of the Strombus gigas conch shell: II - Micromechanics analyses of multiple cracking and large-scale crack bridging. *Acta Mater* **52**, 2395-2406 (2004).

31. J. G. Carter, *Skeletal biomineralization: patterns, processes and evolutionary trends*. (Wiley Online Library, 1990), vol. 1.

32. S. Uozumi, K. Iwata, Y. Togo, The ultrastructure of the mineral in and the construction of the crossed-lamellar layer in molluscan shell. *Journal of the Faculty of Science, Hokkaido University. Series 4, Geology and mineralogy= 北海道大學理學部紀要* **15**, 447-477 (1972).

33. L. T. KuhnSpearing *et al.*, Fracture mechanisms of the Strombus gigas conch shell: Implications for the design of brittle laminates. *J Mater Sci* **31**, 6583-6594 (1996).

34. J. Currey, Further studies on the mechanical properties of mollusc shell material. *J Zool* **180**, 445-453 (1976).

35. J. Gabriel, Differing resistance of various mollusc shell materials to simulated whelk attack. *J Zool* **194**, 363-369 (1981).

36. L. Romana *et al.*, Use of nanoindentation technique for a better understanding of the fracture toughness of Strombus gigas conch shell. *Materials Characterization* **76**, 55-68 (2013).

37. N. Neves, J. Mano, Structure/mechanical behavior relationships in crossed-lamellar sea shells. *Materials Science and Engineering: C* **25**, 113-118 (2005).

38. T. Filetin, I. Žmak, S. Šolić, S. Jakovljević, in *International Conference on Innovative Technologies IN-TECH*. (2010).

39. H. Kessler, R. Ballarini, R. L. Mullen, L. T. Kuhn, A. H. Heuer, A biomimetic example of brittle toughening .1. Steady state multiple cracking. *Comp Mater Sci* **5**, 157-166 (1996).

40. S. Spearing, A. G. Evans, The role of fiber bridging in the delamination resistance of fiber-reinforced composites. *Acta Metall Mater* **40**, 2191-2199 (1992).

41. B. Cox, D. Marshall, Concepts for bridged cracks in fracture and fatigue. *Acta Metall Mater* **42**, 341-363 (1994).

42. G. Bao, Z. Suo, Remarks on crack-bridging concepts. *Applied Mechanics Reviews* **45**, 355-366 (1992).

43. J. Aveston, G. Cooper, A. Kelly, in *Conference proceedings*. (IPC Science and Technology Press Hellertown, PA, 1971), vol. 15.

44. G. Mayer, New classes of tough composite materials—lessons from natural rigid biological systems. *Materials Science and Engineering: C* **26**, 1261-1268 (2006).

45. Z. Tang, N. A. Kotov, S. Magonov, B. Ozturk, Nanostructured artificial nacre. *Nat Mater* **2**, 413-418 (2003).

46. J. E. Rim, P. Zavattieri, A. Juster, H. D. Espinosa, Dimensional analysis and parametric studies for designing artificial nacre. *J Mech Behav Biomed* **4**, 190-211 (2011).

47. W. J. Clegg, The fabrication and failure of laminar ceramic composites. *Acta Metall Mater* **40**, 3085-3093 (1992).

48. W. Clegg, K. Kendall, N. M. Alford, T. Button, J. Birchall, A simple way to make tough ceramics. (1990).

49. H. D. Espinosa *et al.*, Tablet-level origin of toughening in abalone shells and translation to synthetic composite materials. *Nat Commun* **2**, 173 (2011).

50. C.-A. Wang, B. Long, W. Lin, Y. Huang, J. Sun, Poly (amic acid)–clay nacrelike composites prepared by electrophoretic deposition. *J Mater Res* **23**, 1706-1712 (2008).

51. W. Lin, C.-a. Wang, H. Le, B. Long, Y. Huang, Special assembly of laminated nanocomposite that mimics nacre. *Materials Science and Engineering: C* **28**, 1031-1037 (2008).

52. B. Long, C.-A. Wang, W. Lin, Y. Huang, J. Sun, Polyacrylamide-clay nacre-like nanocomposites prepared by electrophoretic deposition. *Compos Sci Technol* **67**, 2770-2774 (2007).

53. V. Vertlib *et al.*, Fast assembly of bio-inspired nanocomposite films. *J Mater Res* **23**, 1026-1035 (2008).

54. A. Sellinger *et al.*, Continuous self-assembly of organic–inorganic nanocomposite coatings that mimic nacre. *Nature* **394**, 256-260 (1998).

55. S. Deville, E. Saiz, R. K. Nalla, A. P. Tomsia, Freezing as a path to build complex composites. *Science* **311**, 515-518 (2006).

56. I. Aksay *et al.*, Biomimetic pathways for assembling inorganic thin films. *SCIENCE-NEW YORK THEN WASHINGTON-*, 892-897 (1996).

57. G. Karambelas, S. Santhanam, Z. N. Wing, Strombus gigas. inspired biomimetic ceramic composites via SHELL-Sequential Hierarchical Engineered Layer Lamination. *Ceramics International* **39**, 1315-1325 (2013).

58. L. Chen, R. Ballarini, H. Kahn, A. H. Heuer, Bioinspired micro-composite structure. *J Mater Res* **22**, 124-131 (2007).

2. Structure Function Investigation of *Hinea brasiliana* and Optical Characterization of the Crossed Lamellar Structure

Abstract

Hinea brasiliana (Lamarck 1822) is a marine gastropod found along the coast of New South Wales, Australia. It has a thick and robust shell that is capable of diffusing the bioluminescent light produced by a series of specialized cells on the surface of the animal's body, which remains within the shell. The light acts as a potential defensive mechanism to ward away predators. The *H. brasiliana* shell structure is typical for Caenogastropoda (recent gastropods), primarily consisting of three crossed-lamellar layers and additional inner and outer surface layers. The shell is composed of 99% calcium carbonate, solely in the aragonite phase, with a minor (1-2% by weight) constituent of organic material. Within the inner crossed-lamellar layer, the c-axis of the aragonite mineral is preferentially aligned in two groups, ±15° from the radial direction of the shell. From nanoindentation of the shell, the inner layer was revealed to have both the highest hardness and modulus of 5.5 GPa and 120 GPa, respectively. The diffusion of light through the shell was investigated and determined to be enabled by the architecture of the crossed lamellar structure. The ability to diffuse optical light was observed in many other crossed-lamellar non-bioluminescent gastropod shells. We further investigated the mineral/organic relationship of the optical properties of another marine gastropod, *Strombus gigas*, in which we found that light is diffused along the direction of the

2nd order lamellae from each 1st order lamellae, and that upon thermal degradation a significant loss of optical properties occurs at 150°C and almost complete absorption by 200°C.

2.1. Introduction

2.1.1. Diversity of Gastropod Morphology and Shell Microstructure

Since the Paleozoic period, gastropods have been evolving mineralized shells with a diverse range of morphological adaptions to resist the increased threat from smashing, peeling, and crushing predators. These shells are calcified bio-composites, composed primarily of a mineral phase of calcium carbonate, typically aragonite, along with a minor secondary organic/protein phase, which controls the growth and the fine organization of the mineral structure. Gastropod and other mollusks, following the Cambrian explosion, evolved numerous shell microstructures within a relatively short period. It is believed that originally the prismatic structure evolved, and by the mid-Cambrian had diversified into primarily the plate-like nacre (Figure 2-1B) and plank-like crossed lamellar structures (Figure 2-1C), which have been the two most common shell microstructures for over the last 400 million years (*2*). In gastropods, the nacre microstructure is almost solely found in the clade Vetigastropoda, while members of Caenogastropoda typically have shells with the crossed lamellar microstructure (*3*). 300 to 250 millions of years ago (MYA), there was an evolutionary arms race between gastropods and their predators that had become significantly stronger and more sophisticated, which resulted in the Mesozoic Marine Revolution (*4*). During this

time period, the dominant shell microstructure of gastropods switched from the organic-rich (5% wt) nacreous structure to the crossed lamellar microstructure, which has a significantly lower organic fraction (1-2% wt) and is found in the majority of extant gastropods (*4, 5*). The adoption of the more energy economic crossed lamellar structure, being both faster and metabolically cheaper to produce (*5*), allowed for the evolution of a vast number of strategies for gastropods to resist the threat from increasingly more aggressive and sophisticated predators. These strategies include a wide range of geometric adaptions, such as spines, ribs, and broad flared outer lips, and diverse shell architectures, such as reduced **umbilicuses**, higher spired shells, and narrowed shell apertures (Figure 2-2 C,D,E; (*4-6*).

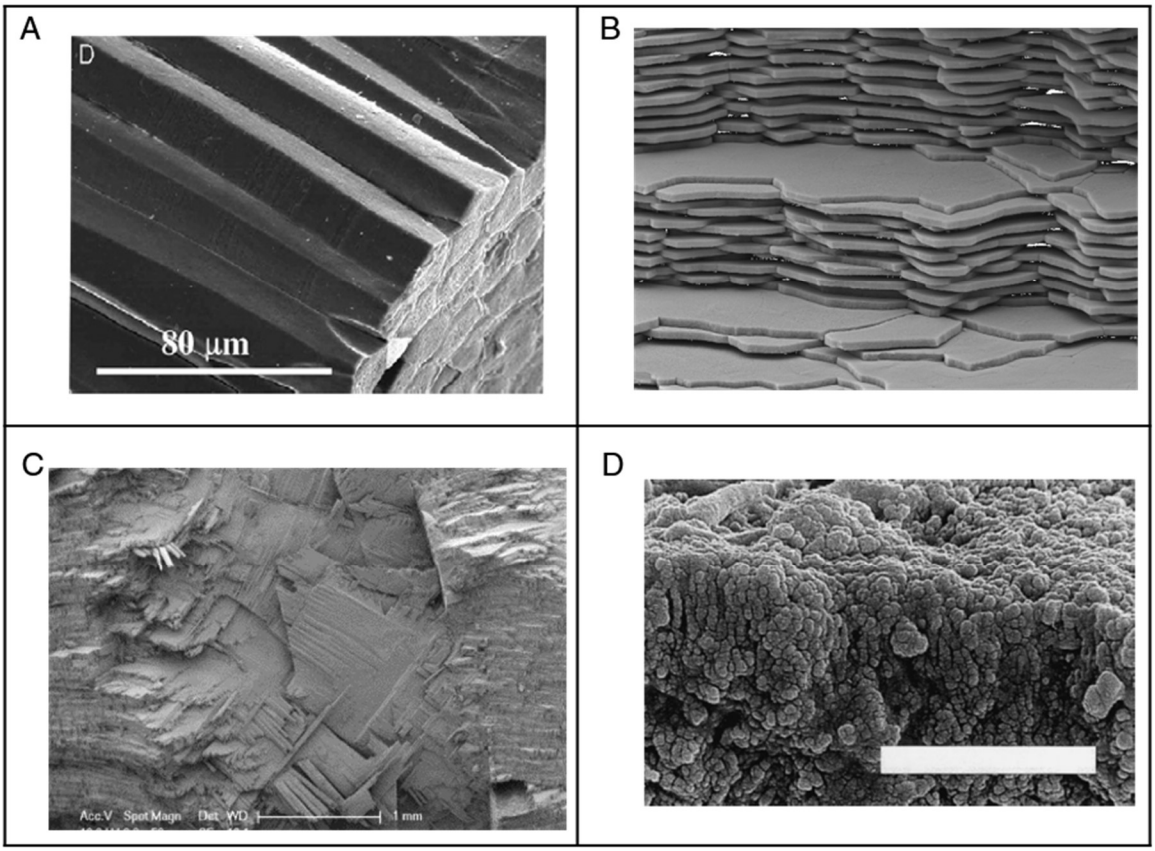

Figure 2-1. Common gastropod microstructures. Prismatic composed of long hexagonal rods (A). Nacre, thin sheets of hexagonal plates (B). Crossed Lamellar, Alternating layers of fine semi-rectangular rods. (C). Homogenous, irregular dense clustering of spheroid shape particles. Image from Chateigner, Hedegaard and Wenk (*7*), scale bar = 5 µm (D).

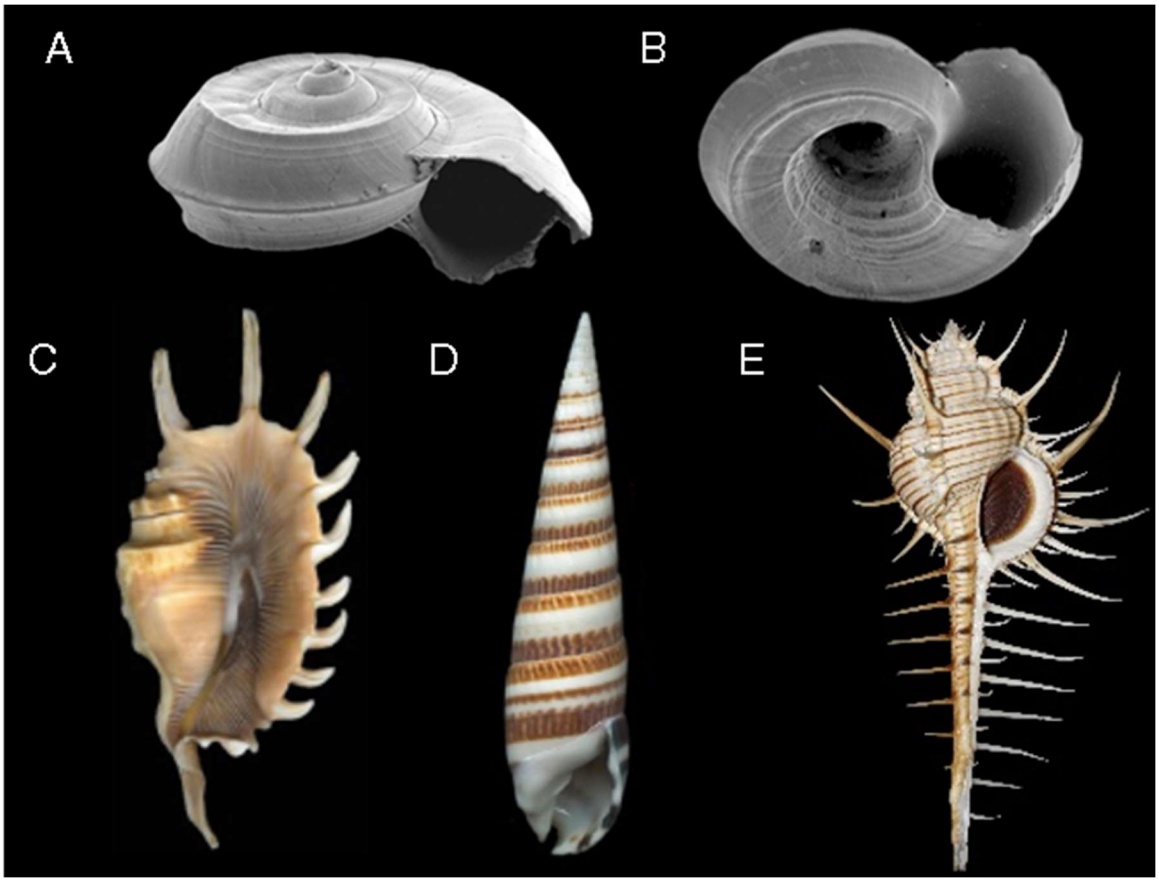

Figure 2-2. Diversity of gastropod shell morphologies. Flat spiral (A),circular apertures (A,B), and unfilled umbilicus (B), were common characteristic of planispiral shells from before the Mesozoic Marine Revolution (MMR), 490-290MYA. After the MMR a number of geometric adaptions occurred in gastropod shells. Broad flared shell lips increase the effective size of the shell, providing defense from crushing and pealing predators (C). High spired shells increase the handling time required for a predator to reach the soft body of the animal which has retracted deep into the shell (D). Long thin spines provides defense from drilling predators (E).

2.1.2. **Diversity of Bioluminescence in Nature**

The phylogenetic distribution of bioluminescence among extant organisms is quite large (Figure 2-3). It is estimated that bioluminescent organisms are some of the most abundant species on earth. While bioluminescence can be found throughout Bacteria and Eucarya, but not Archaea, there is a great diversity in the mechanism and role of bioluminescence among different taxa. Bioluminescent

species are present in both terrestrial and fresh water environments, but are most prevalent in marine life.

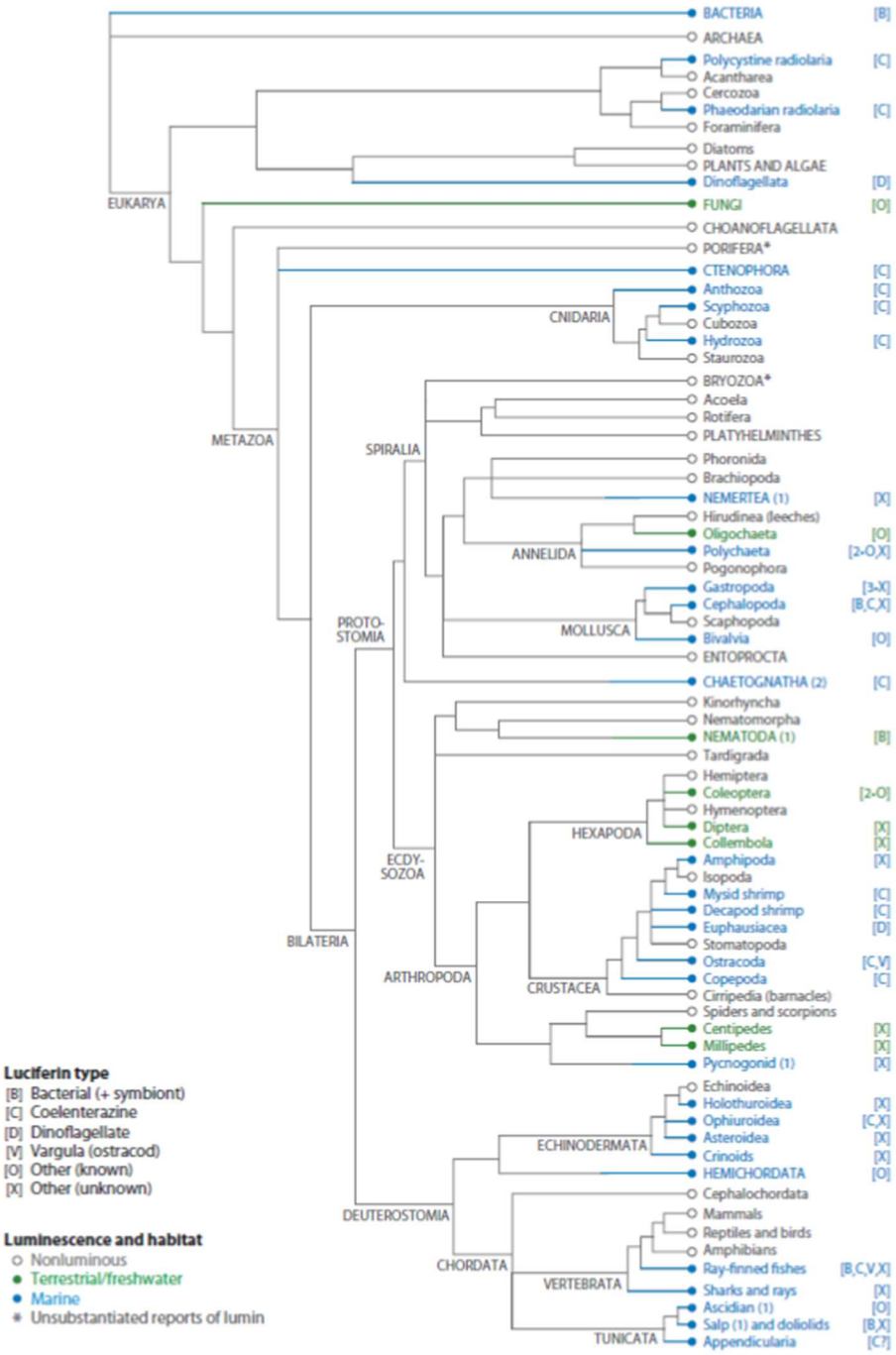

Figure 2-3. Distribution of bioluminescence in the Tree of Life (*1*)

The frequency of bioluminescent taxa within a taxonomic group varies greatly. For example, in arrow worms (Chaetognatha), bioluminescence is rare and occurs in only a few distantly related species (Figure 2-4a). In other clades, however, bioluminescence is common and only a few species are non-luminescent (Figure 2-4b)

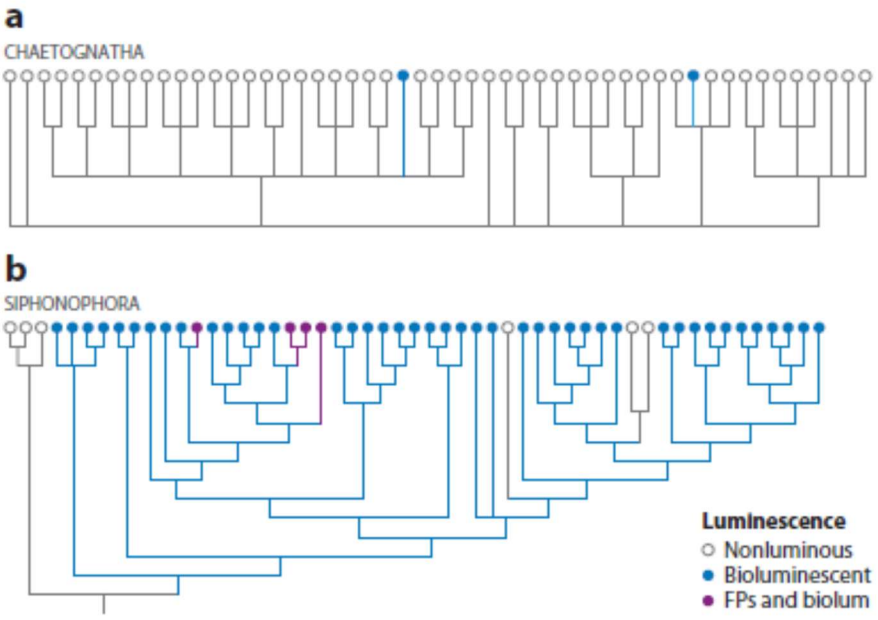

Figure 2-4. Distribution of bioluminescence in two exemplar taxa. Very few chaetognath (a) are luminous, while in siphonophores (b) bioluminescence is frequent (*1*).

The wide phylogenetic distribution of bioluminescence (Figure 2-3) could be explained by a single (or few) originations or rampant convergent evolution of bioluminescence. Given that 35 unique mechanisms have been described, the evidence is consistent with bioluminescence having independently evolved numerous times.

Bioluminescence has been utilized for both defensive and offensive purposes. Some examples of bioluminescent defensive measures are counter illumination for camouflage, flashing light to startle, a “burglar alarm” to attract bigger predators, and misdirection. The bioluminescent display can also be used to lure and illuminate prey (Figure 2-5)

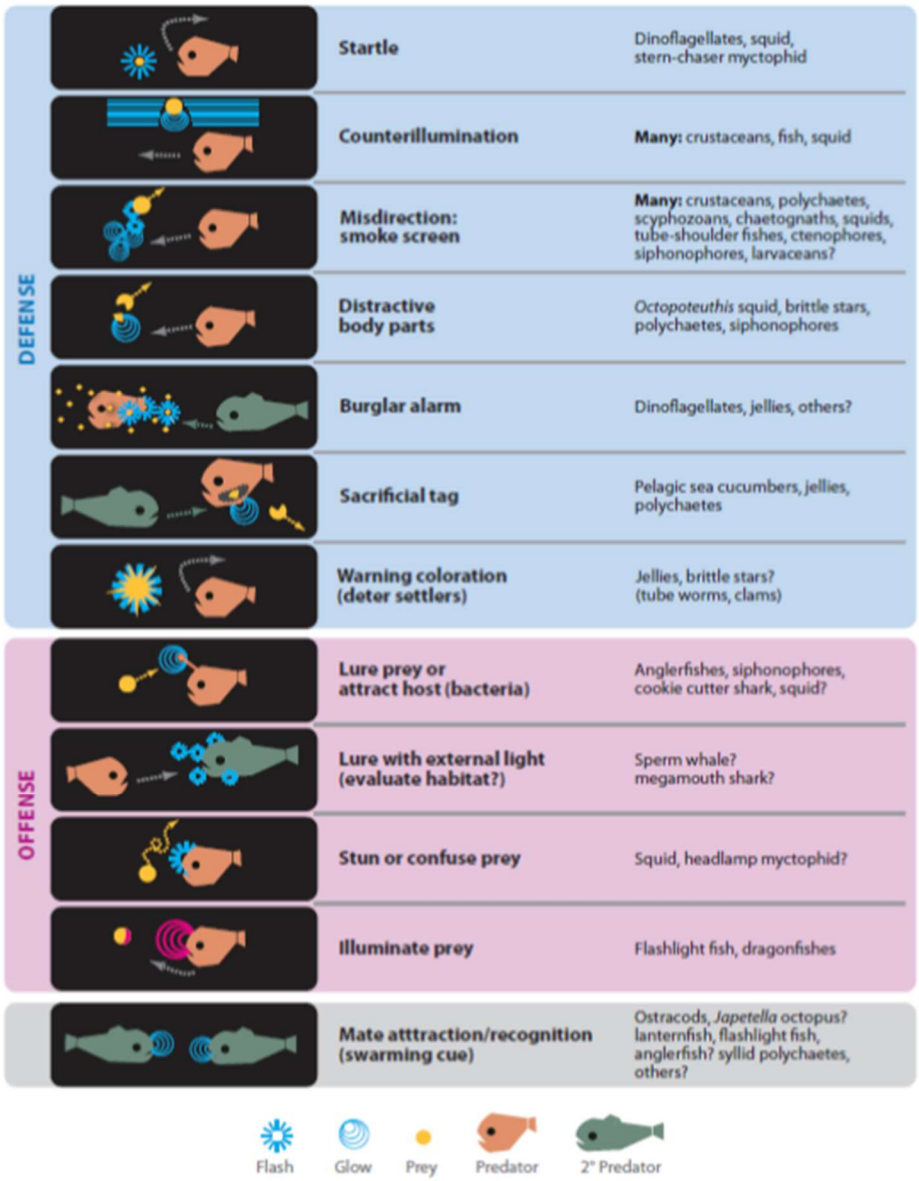

Figure 2-5. Natural utilization of bioluminescence in marine life. It has roles in defense, offense, and mating in many taxa.(*1*)

2.1.3. Bioluminescent Gastropods

Despite the numerous varieties of gastropods and diversity of ecological adaptions, only a relatively small number of species have evolved the ability to bioluminesce. Bioluminescence is a relatively recent adaptation that is found across many different taxa, both aquatic and terrestrial, and has evolved independently numerous times for a wide range of applications including; attracting prey, mating displays, camouflage, and defense from predators (*1, 8*). In the majority of the bioluminescent species, the luminescing organs are typically contained within thin or non-mineralized translucent structures. Rarely has bioluminescence been observed to transmit through densely mineralized structure (*9*). In gastropods, bioluminescence has been reported in the distantly related terrestrial *Dyakia* (*10*), the fresh water *Latia neritoides (11)*, numerous nudibranchs (*12*), and in at least five species belonging to Planaxidea, which have luminescent organs composed of many parallel folds located on the dorsal region of the mantle (*13*).

2.1.4. *Hinea brasiliana* has Spatial Amplification of Bioluminescent Display

Hinea brasiliana (Figure 2-6 A) is a bioluminescent planaxid which possesses a thick and opaque shell that is capable of diffusing bioluminescent light. This light is produced by specialized luminous organs located on the body of the animal, that remains within the shell (*14, 15*); Figure 2-7). We explore the microstructure of the

shell of the *H. brasiliana* and determine the structure-function relationship of the diffusion of light through the shell.

The luminescent organs are located on a patch of the main body of the animal that remains within the shell's interior at all times. The luminescent cells are found in a folded structure typical of luminescent planaxids. The bioluminescent light produced by *H. brasiliana* has a maximum intensity at 518nm. When a spectrum of white light transmitted directly through the shell is measured, a minimum at 518nm is observed. Deheyn *et al.(15)* argued that this minimum is due to the shell preferentially diffusing 518nm over a larger area, reducing the intensity of light directly transmitted. The diffusion of light through the shell of *H. brasiliana* is far greater than that of closely related *P. sulcatus*, which does not allow light to transmit through its shell.

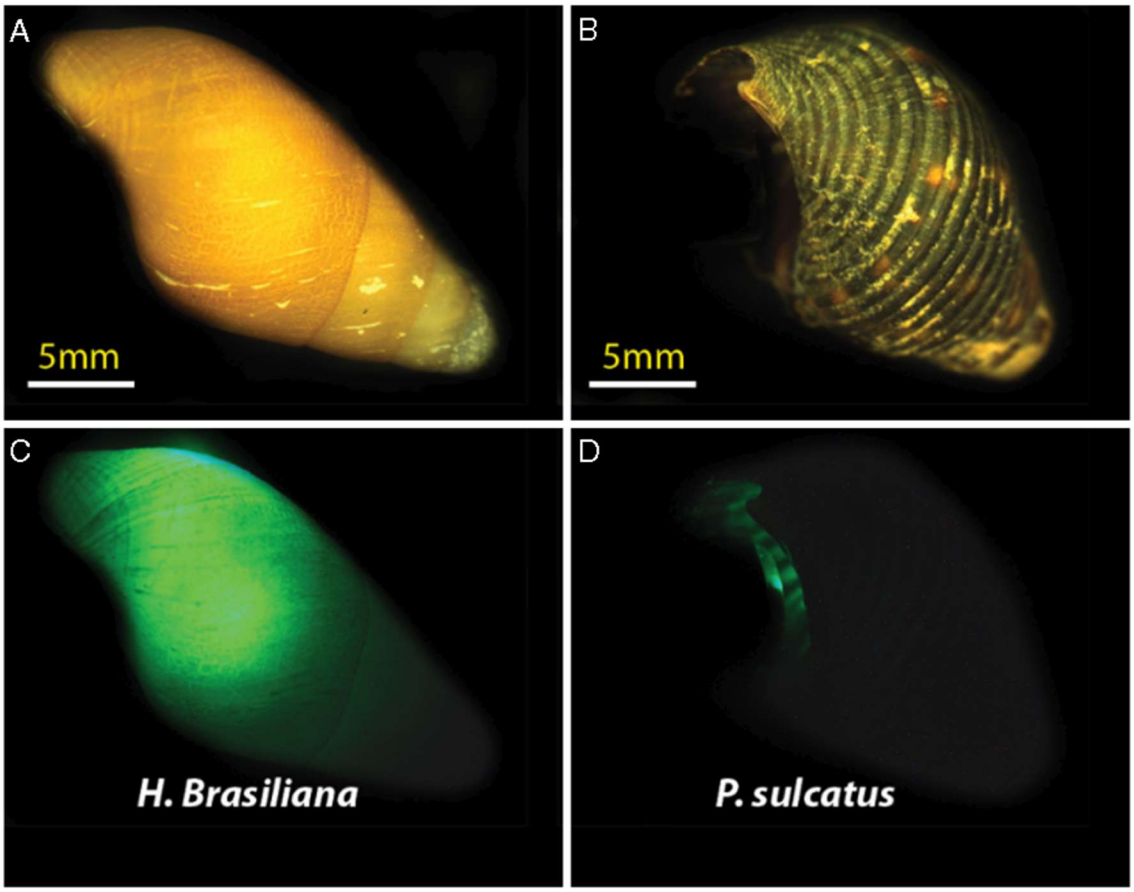

Figure 2-6. Optical images of the shells of *Hinea brasiliana* (A) and *Planaxis sulcatus* (B). When the shells are illuminated from within using a 518nm light source the entirety of the *H. brasiliana* shell (C) is illuminated, while the shell of *P. sulcatus* (D) does not allow light to transmit.

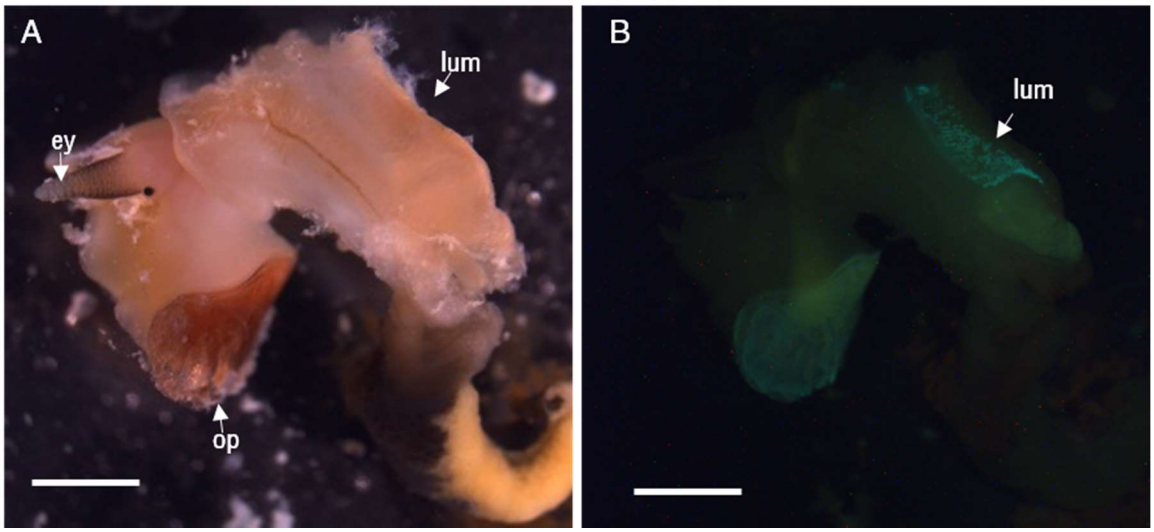

Figure 2-7. Body of the *H. brasiliana* extracted from its shell, luminescent patches (lum), operculum (op), eye stalks (ey) Scale bar = 2mm (A). Treatment with KCl triggers a bioluminescent response; bioluminescent cells are contained within a folded structure located on the posterior of the body (B).

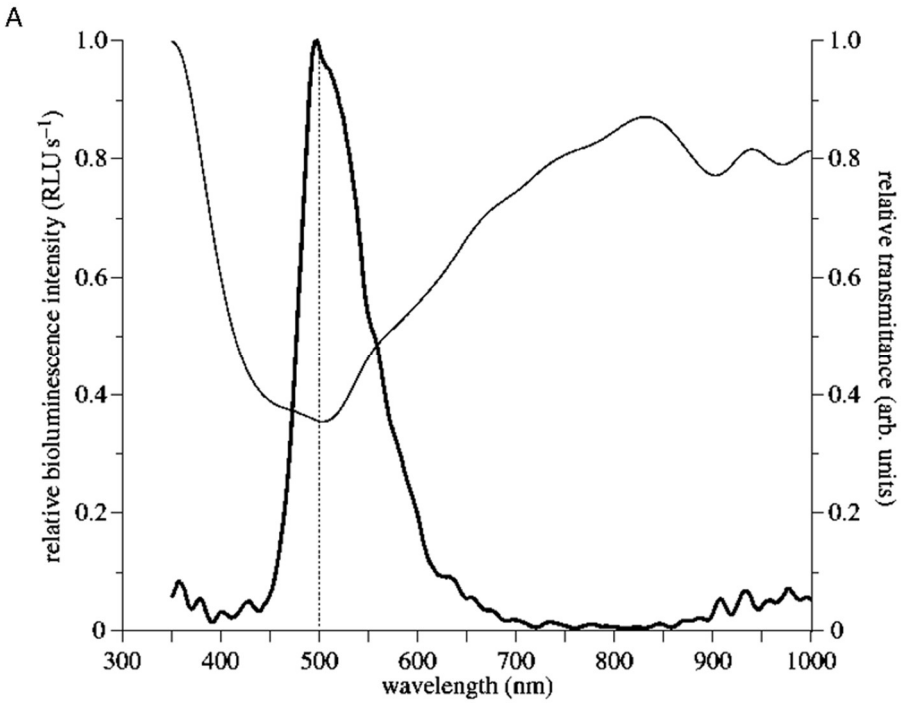

Figure 2-8. Spectrum of the bioluminescent light produced by the *H. brasiliana* (heavy line) and absorbance of white light by its shell (light line). (*15*)

2.2. Ultrastructural Investigation of the Shell from *Hinea brasiliana*

Hinea brasiliana has a thick conical shaped shell that can reach lengths of up to 20mm. The shell interior and exterior are smooth and white in color, with the shell exterior covered by a thick yellow-brown periostracum. The edge of the outer lip is thin, however the region just beyond the edge is significantly thicker, and there are numerous parallel lirea (fine fibs) on the interior at the thickest section of the shell lip (14) (Figure 2-9). Elemental analysis of the shells revealed significant amounts of calcium and oxygen, with trace amounts of silicon, magnesium, and potassium (Figure 2-10). Calcium carbonates are typical for gastropod shells and the low concentrations of minor elemental components are primarily dependent on their local abundance and environmental conditions during shell mineralization (*16*).

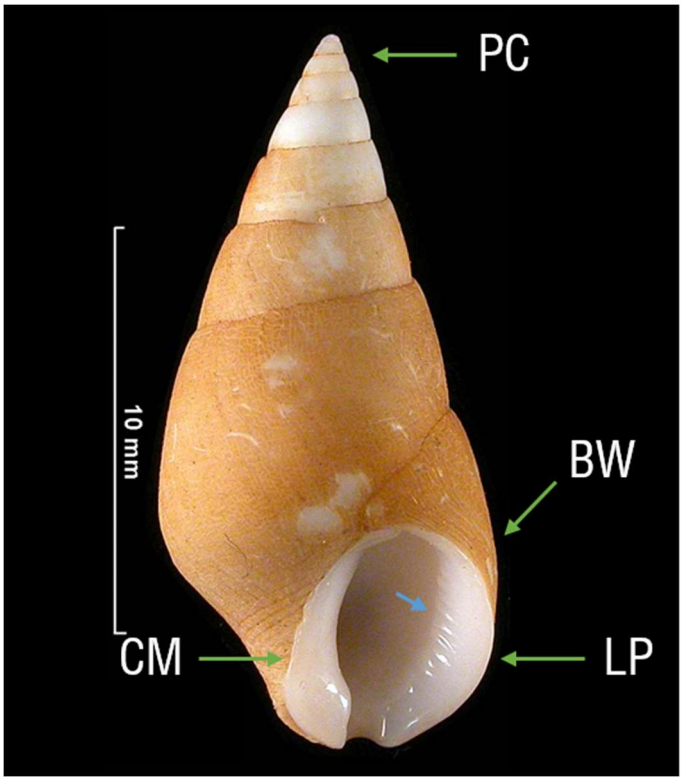

Figure 2-9. View of the *Hinea brasiliana* shell aperture. Protoconch (PC), Body Whorl (BW), Lip (LP), Columella (CM), Lirea (blue arrow) (source: Des Beechey 2008).

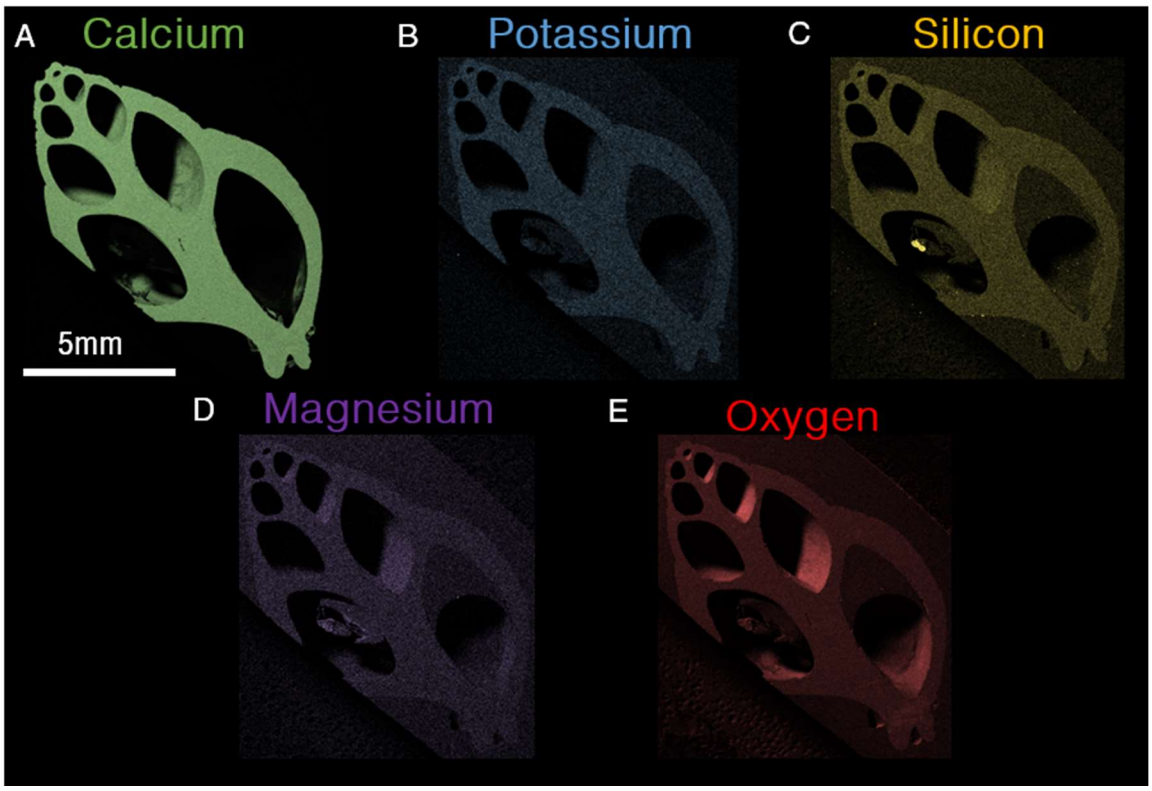

Figure 2-10. Qualitative atomic composition mapping for Calcium (A), Potassium (B), Silicon (C), Magnesium (D), and Oxygen (E).

2.2.1. **Shell Macrostructure**

The shell of *H. brasiliana* consists of five distinct layers: inner surface, inner crossed lamellar, middle crossed lamellar, outer crossed lamellar, and an outer surface (Figure 2-11 A). The inner and outer crossed lamellar layers are composed of commarginal crossed lamellar. The middle crossed lamellar layer is radial crossed lamellar, and is perpendicular to the inner and outer crossed lamellar layers (Figure 2-11 C, D, E). The thickness of the three shell layers varies significantly along both the marginal and growth directions. The shell is thickest near the shell aperture. The inner and outer layers range from 50μm to over 100μm near the lip, the middle layer is typically significantly thicker than the other two

layers, and the overall thickness of the shell can reach up to 1.2mm (Figure 2-12 A). The inner surface layer consists of fine mineral fibers, coated with a proteinaceous sheet, which is in contact with the soft body of the animal. The outer surface layer is composed of a dense organic cuticle, the periostracum, and underlying homogenous/fibrillar mineral structure, which grades into the outer crossed lamellar layer.

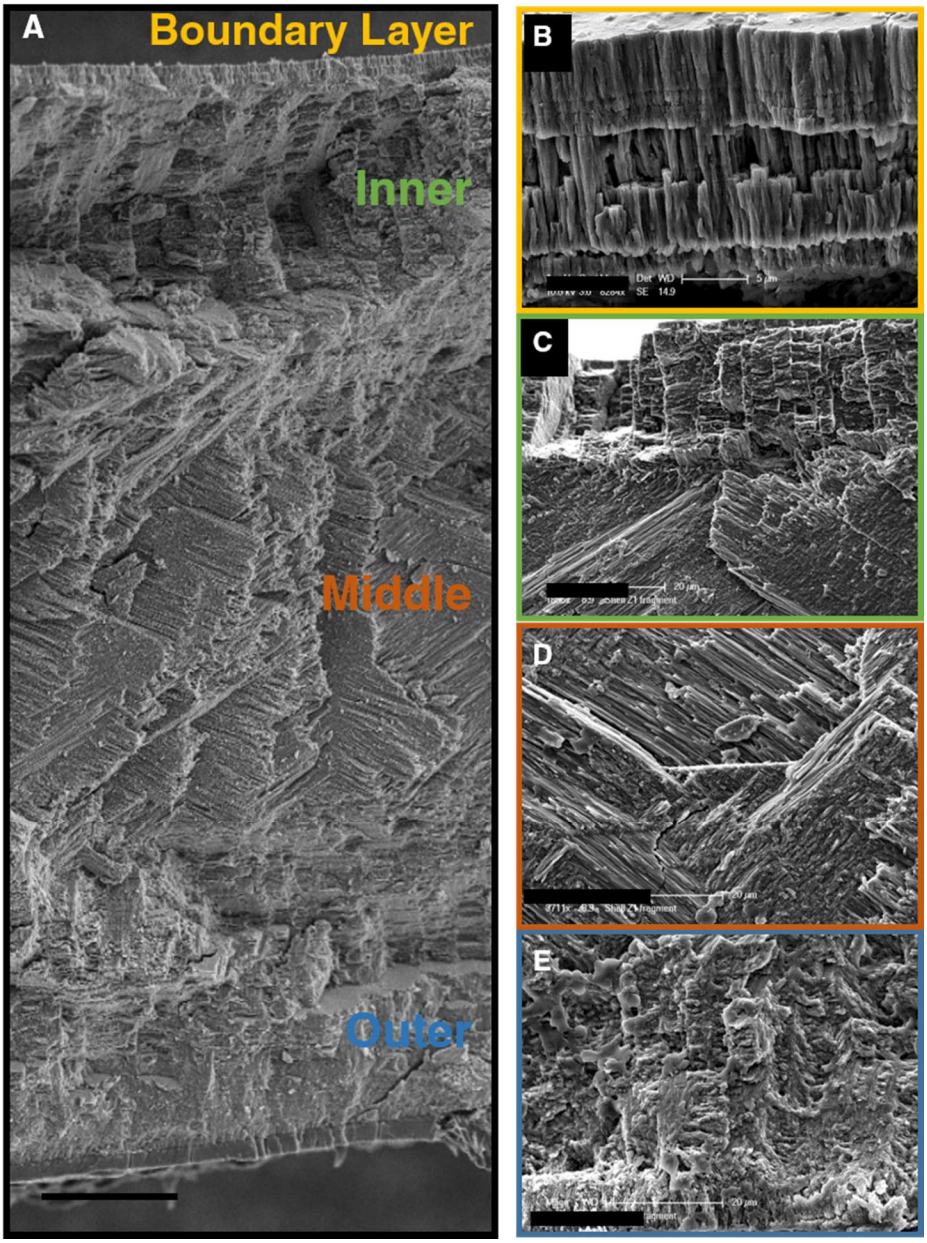

Figure 2-11. Overview of fracture section from the 1st whorl of *H. brasiliana,* showing 5 distinct layers, boundary layer on the inner shell surface, three crossed lamellar layers of orthogonal orientation (Inner, Middle, and Outer), and an organic rich outer layer (periostracum)(A). The boundary layer is composed of radially aligned rods, approximately 1 µm in diameter and 5 µm in length (B). The inner layer is composed of commarginal crossed lamellar(C). In the crossed lamellar structure the 3rd order lamellae are aligned at nearly ±45° from the radial direction, between each macro layer there is typically a 90° rotation along the radial direction. This can be observed in the transition from the inner layer to the middle layer (D). The outer layer has a similar orientation to the inner layer, but is more organic rich indicated by the significant non-mineral structures observed in this region. The increase in present organic fraction could be a result of high mineralization rates in the initial stages of shell deposition (E).

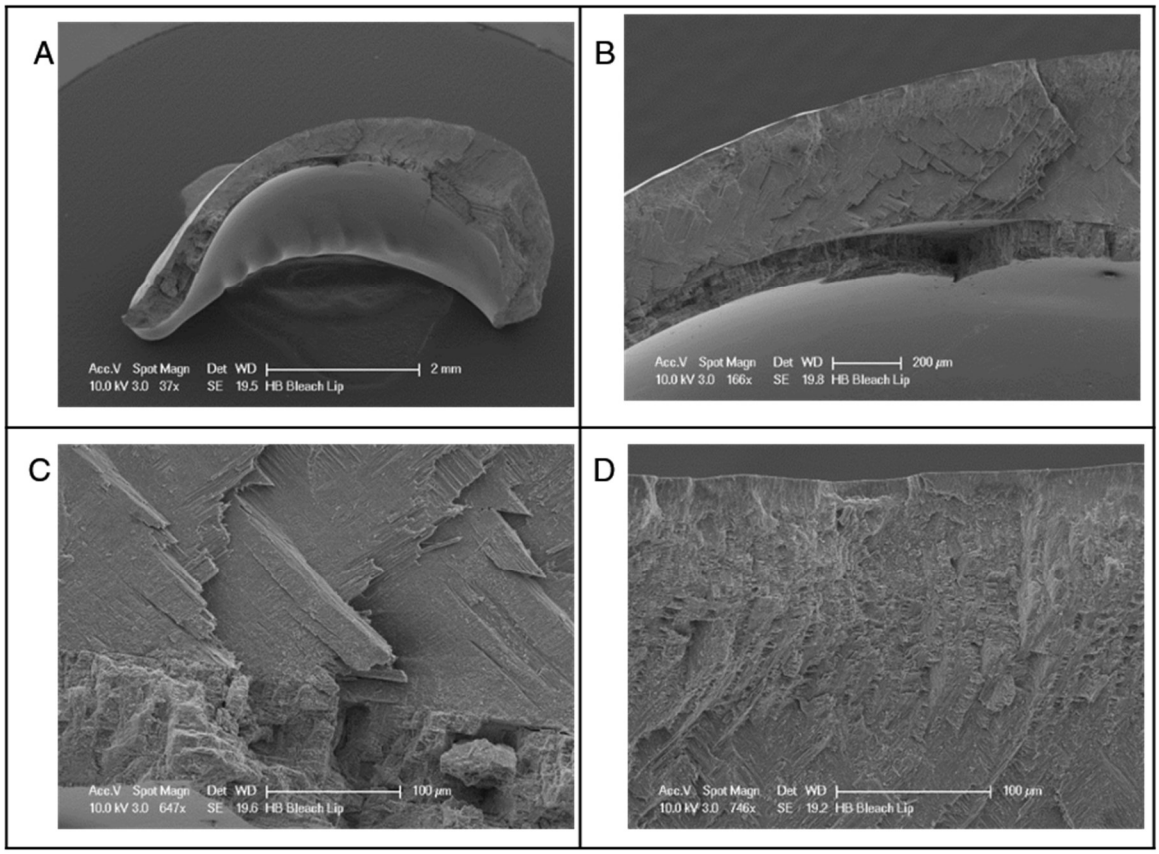

Figure 2-12. Fractured lip of the *H. brasiliana* shell showing the region from the siphon canal to the suture. Interior ribbing is present near the termination of the shell. The shell section was treated with sodium hypochlorite to remove soluble organic material (A). The thickness of the three crossed lamellar layers vary significantly along the marginal direction of the shell, with the middle crossed lamellar growing the largest in the region near the suture (B). Between the inner and middle crossed lamellar layer there is a sudden rotation of the 0th order orientation however there is no distinct interface is present (C). The middle crossed lamellar layer gradual rotates into the outer crossed lamellar layer, 1st order lamellae appear continuous during the 90° rotation between layers (D).

2.2.2. **Crossed Lamellar Microstructure of *Hinea brasiliana***

The crossed lamellar microstructure found in three of the five layers of the *Hinea brasiliana* shell, is a hierarchical structure composed of at least 5 orders of hierarchy. The individual crossed lamellar layers within the shell; the inner, middle, and outer, are the 0th order lamellae. Each 0th order lamella is composed of laminated sheets with an alternating dark and light appearance. The orientation of

the 0^{th} order lamellae is defined by the normal to the surface formed by the laminations within the 0^{th} order lamellae (Figure 2-13 A). In general, the direction of the 0^{th} order in the commarginal inner and outer crossed lamellar layers is along the shell marginal direction (M). In the middle layer the direction of 0^{th} order lamellae is approximately aligned with the shell growth direction (G). The individual laminations of the 0^{th} order are sheets (1^{st} order) composed of unidirectional rectangular bundles (2^{nd} order) of mineral planks (3^{rd} order) (Figure 2-13 B, C, D). The direction of the 2^{nd} order lamellae alternates between two coplanar and nearly orthogonal directions. The 3^{rd} order lamellae are rectangular mineral planks, 100-200nm thick by 150-300nm wide, and several μm in length. The 2^{nd} order bundles are composed of a semi-regular packing of 3^{rd} lamellae. The 3^{rd} order lamellae only extend for a few μm (~5 μm), numerous 3^{rd} order lamellae assemble end on to span the length of the long 2^{nd} order bundles.

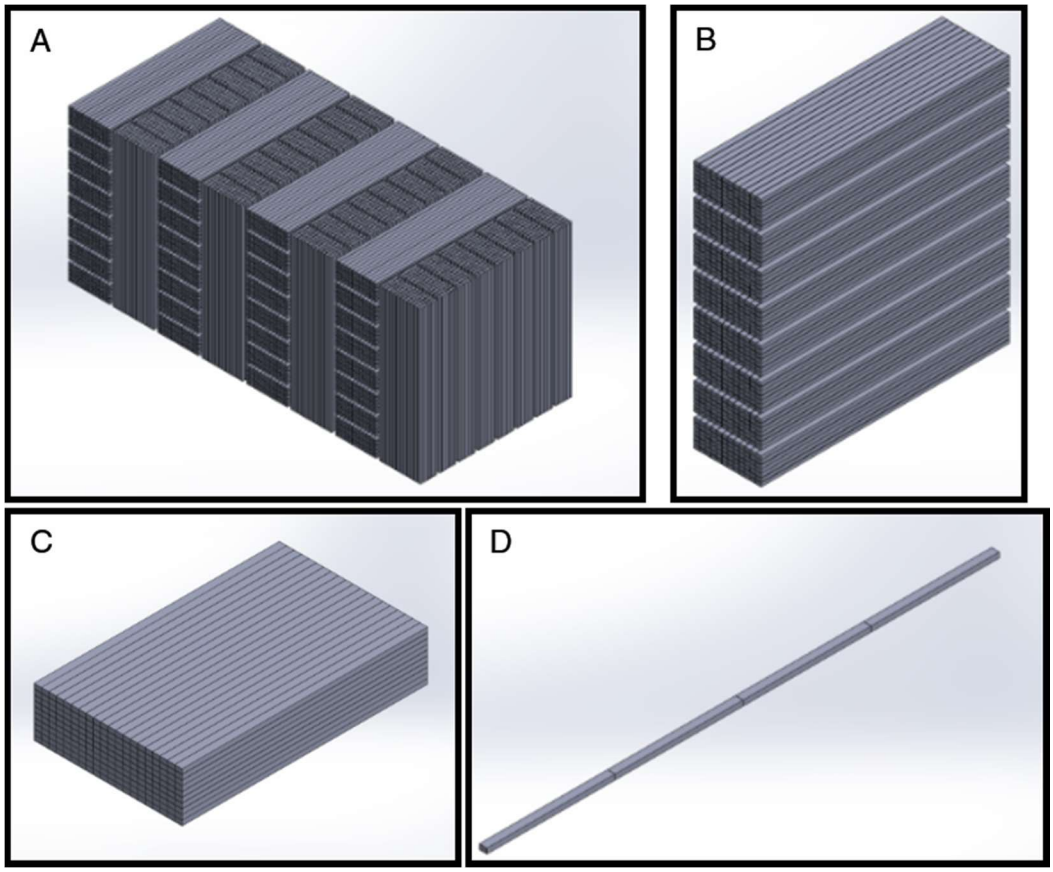

Figure 2-13. Primitive 3D-CAD model of the hierarchy in crossed lamellar structure created. A single crossed lamellar layer (0^{th} order or Macro layer) (A), is a laminate composed of multiple 1^{st} order lamellae (B), with alternating orthogonal (nearly) "fiber" direction which is responsible for the light and dark striations observed in the structure. The 1^{st} order lamellae are sheets composed of a single unidirectional layer of long rectangular 2^{nd} order lamellae (C), which are stacked along their thickness. The 2^{nd} order lamellae are composed of rectangular array of 3^{rd} order planks (D).

The size, shape, organic composition, and definition of the different order crossed lamellar features varies significantly from layer to layer, in the different spatial and temporal regions of the shell, and from specimen to specimen. The region of the shell in the middle of the body whorl is far enough away from shell sculptures to contain sections of relatively uniform and flat crossed lamellar microstructure, which aids in the identification of the many microstructural features. The different orientations of 0^{th} and 1^{st} order lamellae are visible when the shell is

fractured (Figure 2-14 A). The 2nd order lamellae are aligned ±45° from the radial direction of the shell. The alignment of the 2nd order lamellae is evident from fractures that delaminate the structure along the 1st order boundary, by the presence of crossed fibers forming an X pattern. When the crossed lamellar structure is fracture normal to the 1st order sheets, the fracture travels along an alternating path, producing the dark and light effect (Figure 2-14 B). The 1st order lamellae within the middle crossed lamellar layer vary in thickness from 5-25μm. The 2nd order lamellae are approximately 5μm thick.

Modifications to the crossed lamellar structure are found in regions where the shell geometry is modified. Examples of such areas are near sutures, where a newer shell whorl attaches to an older whorl, and in areas that change in curvature. In such regions, the different crossed lamellar layer and curve and deform to accommodate the modified shell geometry. The 2nd order lamellae within a 1st order sheet show a long scale curvature, while they remain relatively collinear with their neighboring lamellae (Figure 2-15 B). In addition, the 0th order orientation varies along the marginal axis of the shell. The 3rd order planks in these regions shows a large degree of curvature while still appearing smooth and continuous (Figure 2-15 D).

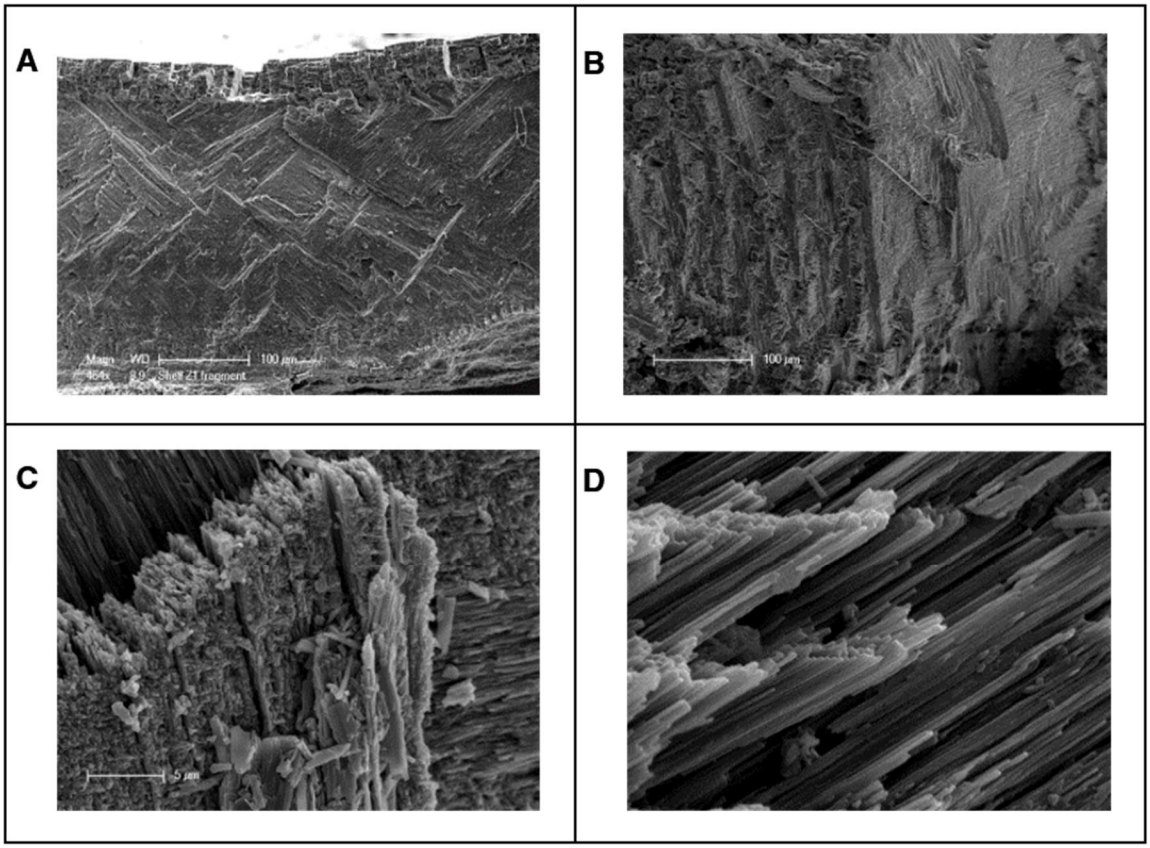

Figure 2-14. SEM micrographs of the different level of hierarchy observed in fractured *Hinea brasiliana* shell. The shell contains three 0th order layers (A). Within each 0th order layer, 1st order lamellae are visible due to the alternating dark and light contrast (B). The fine continuous interface between adjacent 2nd order lamellae from within one 1st order (C). The 3rd order planks are locally parallel (D).

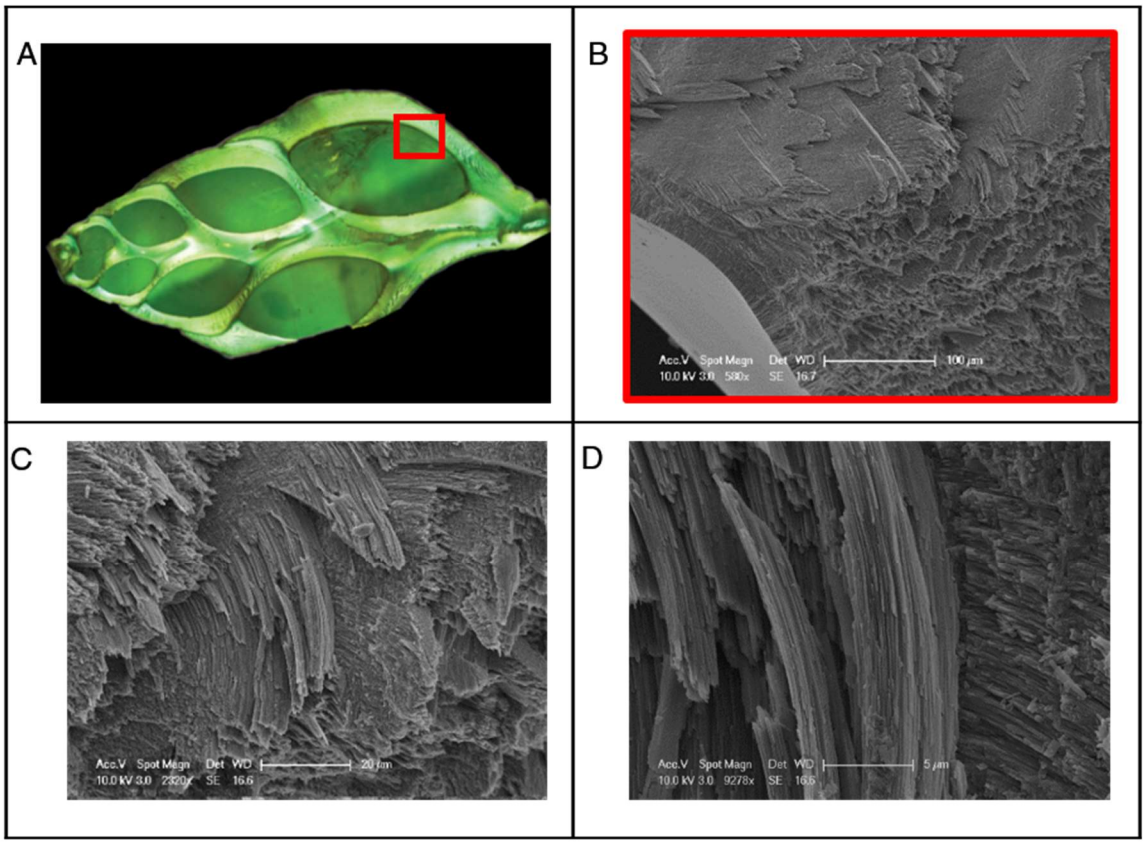

Figure 2-15. Crossed lamellar structure in curved regions of the *H. brasiliana* shell (A). Curvature is accounted for by at least two methods in the crossed lamellar structure, by changing the 1st order layer thickness, and by changing the direction of the 2nd order lamelllae within a 1st order lamellae (B). Local regions of the 1st order lamellae have parallel 2nd order dirrections (C). The 3rd order lamellae within the curved regions still apear smooth and continous (D).

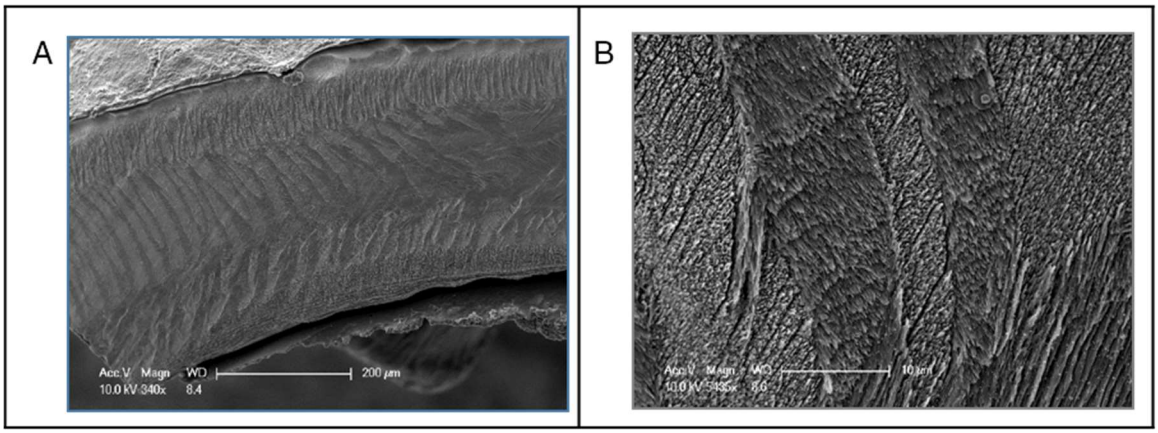

Figure 2-16. The shell of *H. brasiliana* after demineralization with RDO. Gradual gradiation from inner to middle layer is apparent. Thick, remnant organic sheats are present at the inner and outer surfaces of the shell (A). Within the middle layer, large 2nd order boundary are not present. The 2nd order lamellae maybe thin (<5µm) or non-existant in this region (B).

2.2.3. **Outer Surface (Periostracum)**

The periostracum of *Hinea brasiliana* is yellow-brown and thick. The periostracum is composed of a dense mat of radially aligned organic fibrils that form a dense cuticle protecting the shells exterior (Figure 2-16 A, Figure 2-17 A). The periostracum is believed to be involved with the origins of mineralized shells in gastropods, and functions to aid in controlling the mineralization of calcium carbonate in the shell. Directly below the periostracum is a mineral surface formed by a random homogenous arrangement of spherical mineral and organic clusters 100-400nm in diameter (Figure 2-17 D). The spherical particles gradually grade into loosely formed radial fibers before the start of the outer crossed lamellar layer (Figure 2-18).

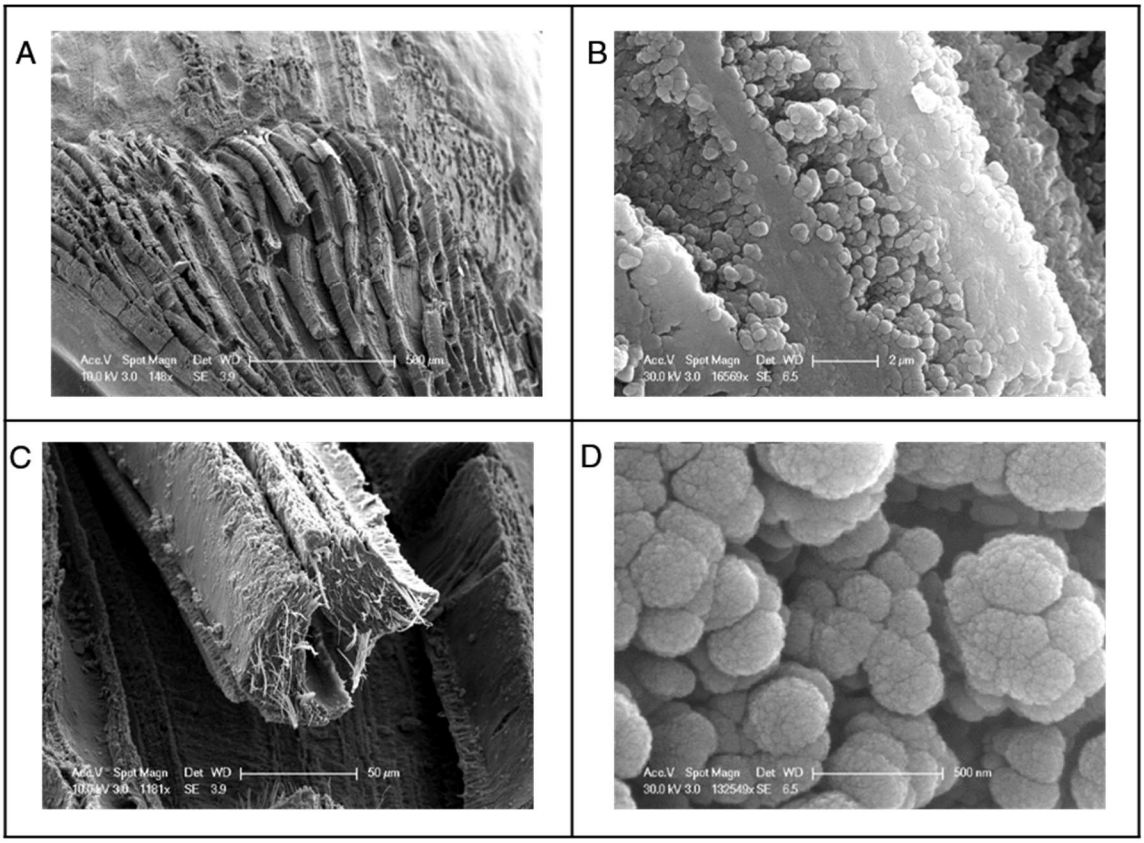

Figure 2-17. Outer surface of *Hinea brasiliana* shell. Periostracum is colored a deep yellow and is easy to flake (A). Mineralized outer surface, smooth striation are remnants of the ribbed organic cuticle (B). Ribs are composed of fine fibers, in this micrograph the rib has begun to delaminate pulling the substrate along with it (C). Spheroid particles on the exterior of the shell, diameter 200-500nm, with <60nm sub-particles (D).

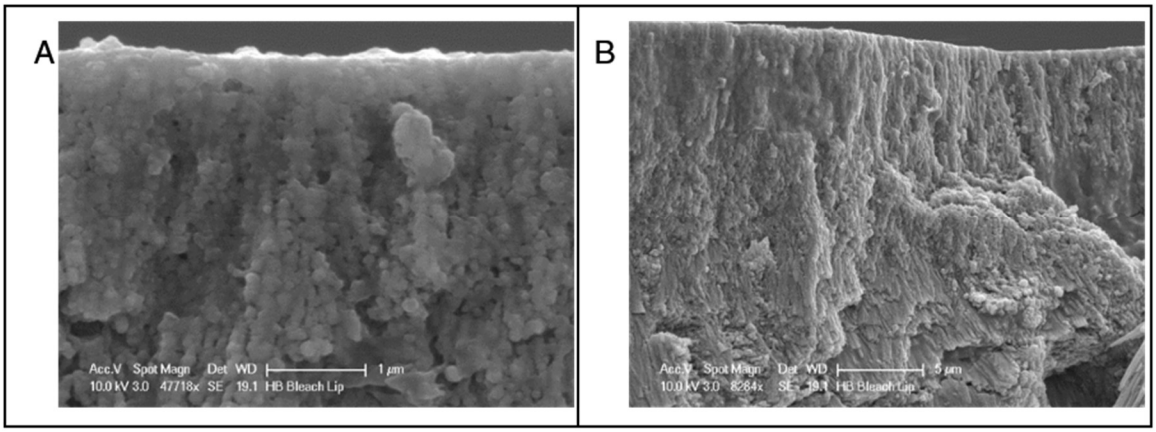

Figure 2-18. Outer surface of the *H. brasiliana* shell after treatment with sodium hypochlorite to remove soluble organic material. Outer surface layer is composed of radially aligned fibers, with a dense organic cuticle on the exterior (Periostracum). The outer surface fibers are composed of linear agglomeration of spherical particles (approximately 50-100nm) (A). The transition from the outer surface layer to the outer crossed lamellar layer is gradual and there is no well-defined boundary. In both layers the structure features are obscured by a significantly higher fraction of interlamellar organic material (B).

2.2.4. **Inner Surface**

The inner surface layer of the shell is the region between the soft body of the animal and the inner crossed lamellar layer. It is composed of a thin veneer of densely packed, well-formed, radially aligned rods that are approximately 3-5µm in length. The inner surface is composed of multiple layers veneers, representing seasonal or sporadic growth of the shell. The surface of this layer is coated with a thick proteinaceous sheet that caps the ends of the mineral rods leaving a smooth surface. Evidence of the continued deposition of the inner surface layer is apparent in the new growth region near the lip of the shell. In this region, a terraced mineral front can be observed that represents the boundary of the newest layer. At the edge of this boundary of spherical particles, the fundamental gastropod mineral structural units are observed (Figure 2-19 E).

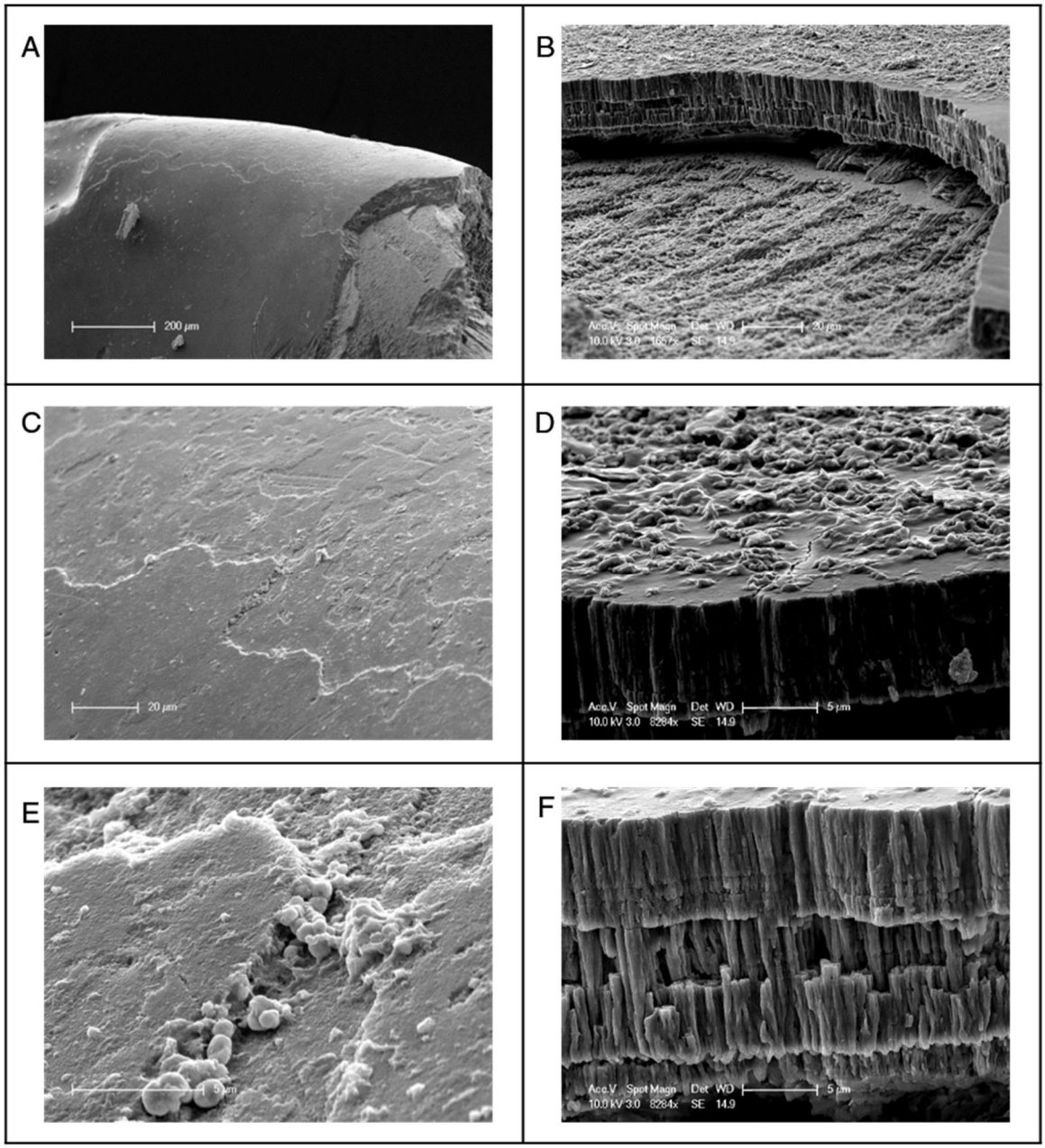

Figure 2-19. Fracture section of the interior surface of the *H. brasiliana* shell near the lip. Thick inner surface layer is visible with a terraced growth front parallel to the lip edge and perpendicular to the growth direction (A). The inner surface forms a thick (5-20µm) layer that caps the inner crossed lamellar layer (B). At the terraced growth front near the lip, the formation of an additional layer of radially aligned rods on top of the existying inner surface layer (C). The surface of the inner surface layer is smooth and coated with an organic film (D). At the boundry of the new growth terraces, spherical particals are present (E). The inner surface layer is composed of sheets of radially aligned rods. Bands are present in the inner surface layer that indicate periodic growth (F).

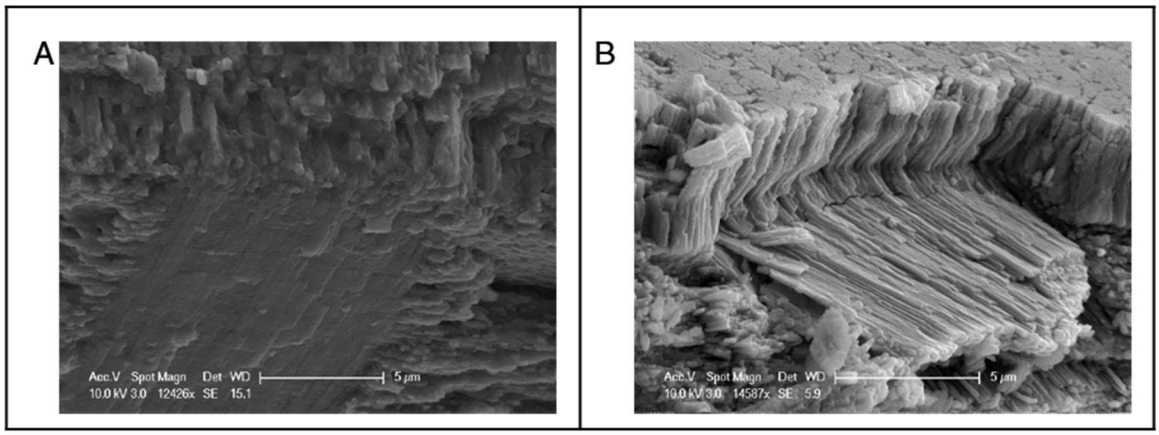

Figure 2-20. Interface between the inner surface layer and the inner crossed lamellar layer in the *H. brasiliana* shell. No distinct interface is present between the two layers; fibers of each layer blend into each other (A). Gradual transition is present in other areas, with a small region of rods existing at an intermediate angle between the two layers, intermediate angle present is dependent on the dip angle of the adjacent 1st order lamellae (B).

The dense arrangement of fibers in the inner surface layer does not show evidence of ordering along the pattern of the 1st order lamellae from the adjacent shell layer. At the transition from the inclined 3rd order lamellae from the inner crossed lamellar layer to the radially aligned rods of the inner surface layer, no distinct organic interface can be observed, instead the 3rd order rods undergo a redirection from inclined to radially aligned (Figure 2-21 B).

In comparison, the inner surface layer from the shell of *Planaxis sulcatus* is composed of 3-5µm rods that are slightly inclined from the radial direction (Figure 2-21 A). The inner surface rods of *P. sulcatus* are patterned from the 1st order lamellae from the adjacent crossed lamellar layer. The inclination of the inner surface layer is opposite of the crossed lamellar dip direction and alternates with the 1st order lamellae. The inner surface is lacking the thick proteinaceous sheet and the ends of the rods form a rough surface.

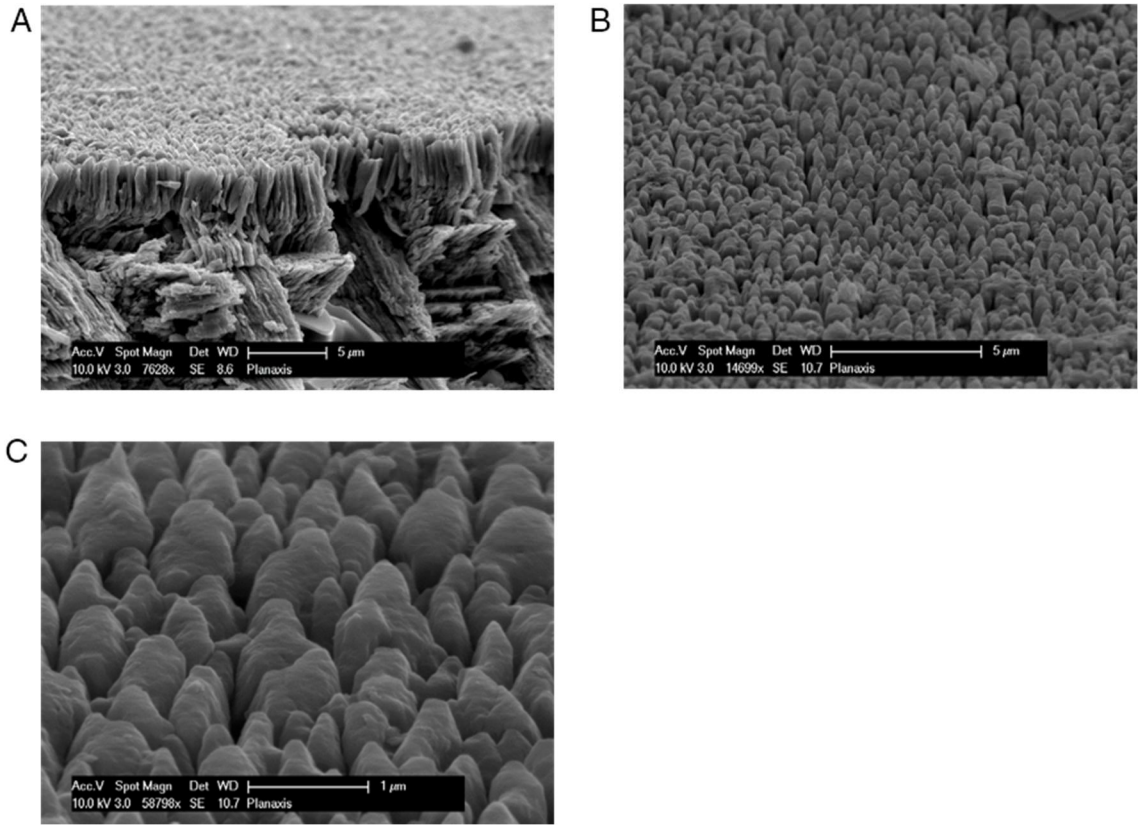

Figure 2-21. Inner surface layer of *Planaxis sulcatus*, a close relative of *H. brasiliana*. A single layer of rods is present. The rods are slightly inclined from the radial direction with the angle of inclination dependent on the dip direction of the adjacent 1st order lamellae in the inner crossed lamellar layer (A). View of the inner surface of the shell, showing the "1st order" layers within the inner surface layer (B). The inner surface is rough and composed of rods with tapered ends; unlike in *H. brasiliana*, thick sheets of organic material were not observed on the surface of this layer (C).

2.2.5. **Crossed Lamellar from Select Species**

The organization of the crossed lamellar microstructure in the *Hinea brasiliana* shell has many commonalities with the crossed lamellar structure from other members of family Planaxidea and other caenogastropods. Caenogastropods typically have shells composed of multiple crossed lamellar layers, most commonly composed of three layers that are a combination of commarginal and radial

crossed lamellar. In the shells of other planaxids, for example *Planaxis nigra* (Figure 2-22 A), the number, thickness, and orientation of crossed lamellar layers are similar to those found in the shell of *H. brasiliana*.

The size and shape of the higher order crossed lamellar features varies significantly among crossed lamellar gastropods, in both close and distantly related species. The 3rd order lamellae in the inner crossed lamellar layer of the *Planaxis nigra* shell are well-formed rectangular planks with a relatively consistent cross section (Figure 2-22 B). The 2nd order lamellae in crossed lamellar from *H. brasiliana* and other planaxids are thinner and less well defined than the 2nd order lamellae reported for other common crossed lamellar gastropods. There are two possible explanations for the absence of visible, well-defined 2nd order interface. One possibility is that interface is obscured because the 2nd order bundles are thin (<1μm) and similar in length scale to the thickness of 3rd order lamellae. Another possibility is that the 2nd order interface is thinner, and contains less organic rich interfacial material. The 2nd order interfaces in the shell of the casket nassa (*Nassarius acrularius*) are well-defined and spaced every 5-10μm (Figure 2-23 D). The casket nassa shell is composed of only two orthogonal crossed lamellar layers (Figure 2-22 C).

The inner surface layer of many other members of the genus *Hinea* have an inner surface layer that is composed of radially aligned mineral rods and is similar to that of *Hinea brasiliana*. The inner surface layer of the *Hinea inepta* shell has a smooth surface and residual organic material was present (Figure 2-22 E

and F). Inner surface layers composed of radially aligned rods have been reported in other gastropods. The inner surface layer could potentially have a role in the termination of mineral growth on the interior of the shell.

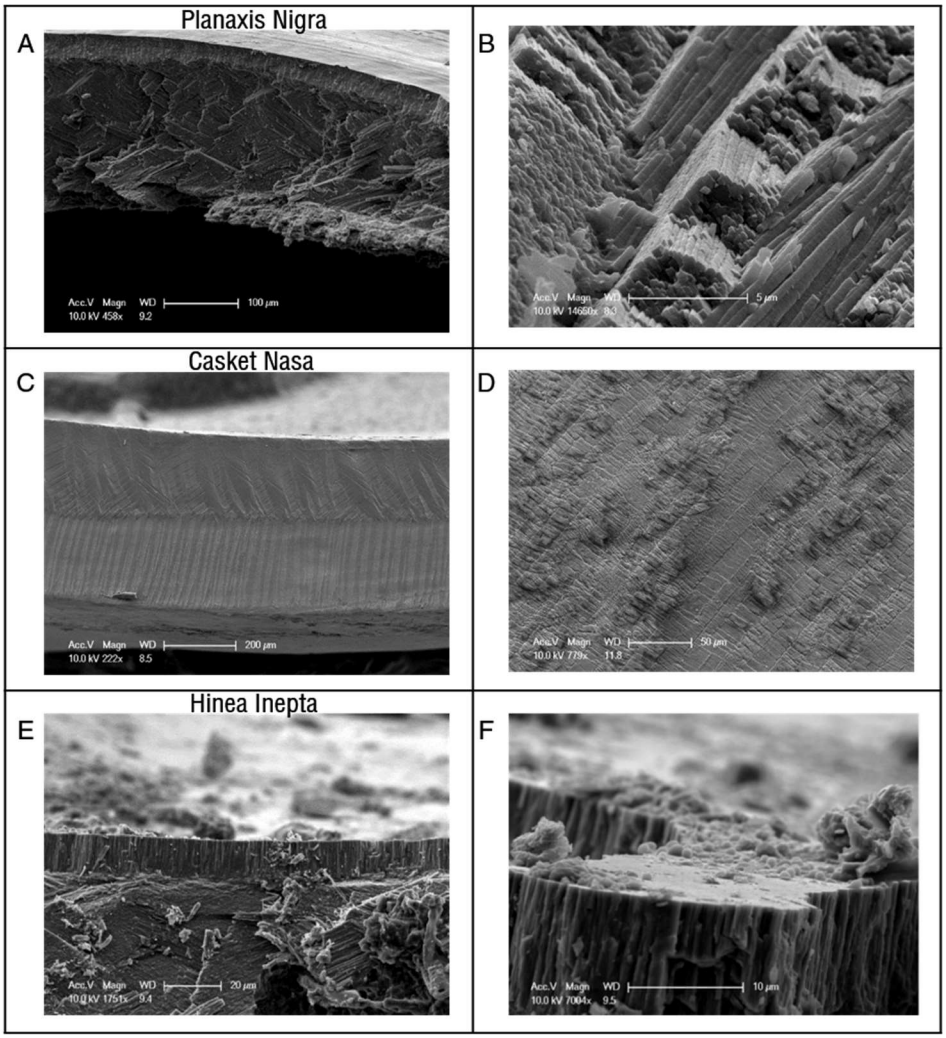

Figure 2-22. Fracture section from various caenogastropods. *Planaxis nigra* has a similar microstructure as *H. brasiliana* with three crossed lamellar layers (A). However the 3rd order lamellae in this specimen are regular in their rectangular cross section (B). The shell of the casket nassa (*Nassarius arcularius*) with only two crossed lamellar layers (C). In the inner layer of the casket nassa, the 2nd order lamellae have a "thin" 2nd order lamellae, larger than what is present in *H. brasiliana* but smaller than those typically found in *S. gigas* (D). In the shell of *Hinea inepta*, there is only one crossed lamellar layer, however the inner surface layer is composed of radially aligned rods with a smooth organic coated interior surface, similar to what is observed in *H. brasiliana* (F).

2.2.6. **Interfaces 0th Order**

The 0th order interfaces are the boundaries between the individual shell layers, forming planer sheets that are normal to the radial direction of the shell. There are three kinds of 0th order interfaces observed in the *Hinea brasiliana* shell, inner surface to inner crossed lamellar (Figure 2-23 A), crossed lamellar to crossed lamellar (Figure 2-23 B and C), and crossed lamellar to outer homogenous (Figure 2-23 D). The strength of the interface between shell layers is vital in resisting shell fracture by durophagous predators through the redirection and twisting of fracture through the interface and avoiding delamination failure along the shell layers. The 3rd order plank/rod features appear morphologically continuous at from the inner surface to the inner crossed lamellar, transmission electron microscopy of similar structures in other gastropods has shown that the structure is crystallographically continuous across this interface (*17*). There is a gradual transition from the outer crossed lamellar to the outer surface homogenous layer, and the interface between these two layers is not well defined. Random clusters of spheroid mineral agglomerates, which are similar in size and morphology to 4th order lamellae that compose a 3rd order lamella, form semi-linear fibers, which incline to form the 3rd order lamellae of the outer crossed lamellar layer (Figure 2-18 A and B).

The interfaces between crossed lamellar layers couple two orthogonal crossed layers. Each crossed lamellar layer is composed of a number of “dark” and “light” 1st order lamellae with perpendicular fiber directions. At the interface between crossed lamellar layers, some 1st order lamellae continue across the 0th

order interface and transition into the other crossed lamellar layer, while other 1st order lamellae appear to end at the 0th order interface (Figure 2-23 B and C). The 1st order lamellae that cross the interface undergo a gradual rotation to adopt the dip directions of their new layer. This rotation suggests that during construction the 0th order layers are related by a rotation and do not share a mirror plane symmetry. The lack of symmetry results in the discontinuation of some 1st order lamellae at the 0th order interface, where they form an interlocking pattern with 1st order from both layers (Figure 2-24 A and B). The continuation of 1st order lamellae between shell layers aids in the toughening of the shell by causing the fracture to twist at the interface between layers.

The quality of the interface between layers can vary significantly in local regions along the shell. In numerous fracture sections, occasional failure is observed along local smooth flat interfaces between layers (Figure 2-12 B). The presence of these interfaces in not regular within the shells, and it is not clear if they have a mechanical significance or if they are an artifact of the shell mineralization process.

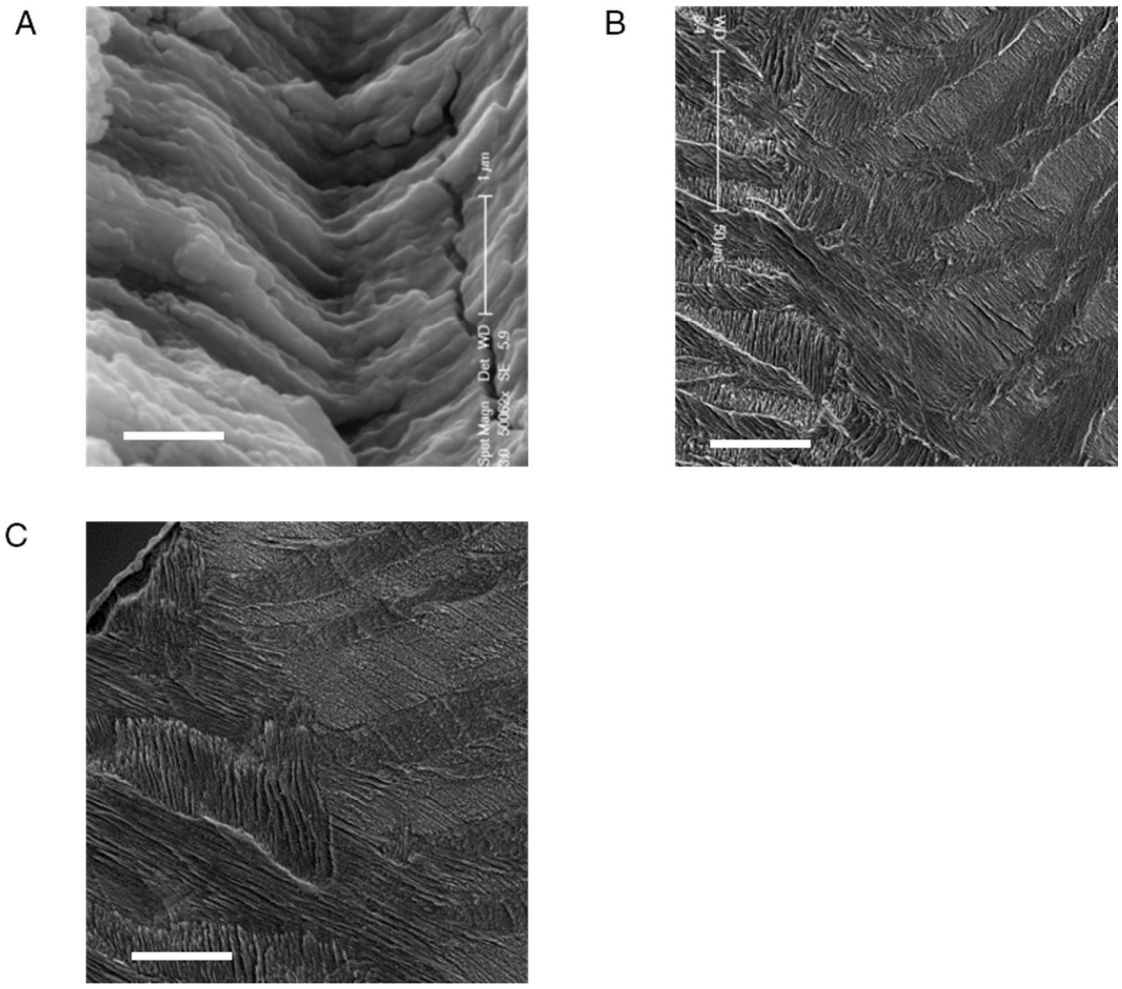

Figure 2-23. Transitions between layers in the *H. brasiliana* shell. Inner surface transition to the inner crossed lamellar layer. Radially aligned rods go through 2 steps of slight redirection before the interface with the inner crossed lamellar layer. The fracture that runs vertical through the micrograph was most likely caused by the fracture preparation method, as it does not appear to follow any distinct morphological feature. The rods/planks of the inner surface layer appear continuous during their transition between layers (scale bar = 1 μm) (A). The interface between inner and middle crossed lamellar layer in a polished and demineralized (RDO) sample. 1st order lamellae from the inner layer appear to cross the boundary between the inner and middle crossed lamellar layers (scale bar = 25 μm) (B). A similar phenomena is observed at the interface between the middle and outer crossed lamellar layers, signified by the lack of distinctly interface between the "dark" 1st order layers of the two adjacent 0th order crossed lamellar structures (scale bar = 25 μm) (C).

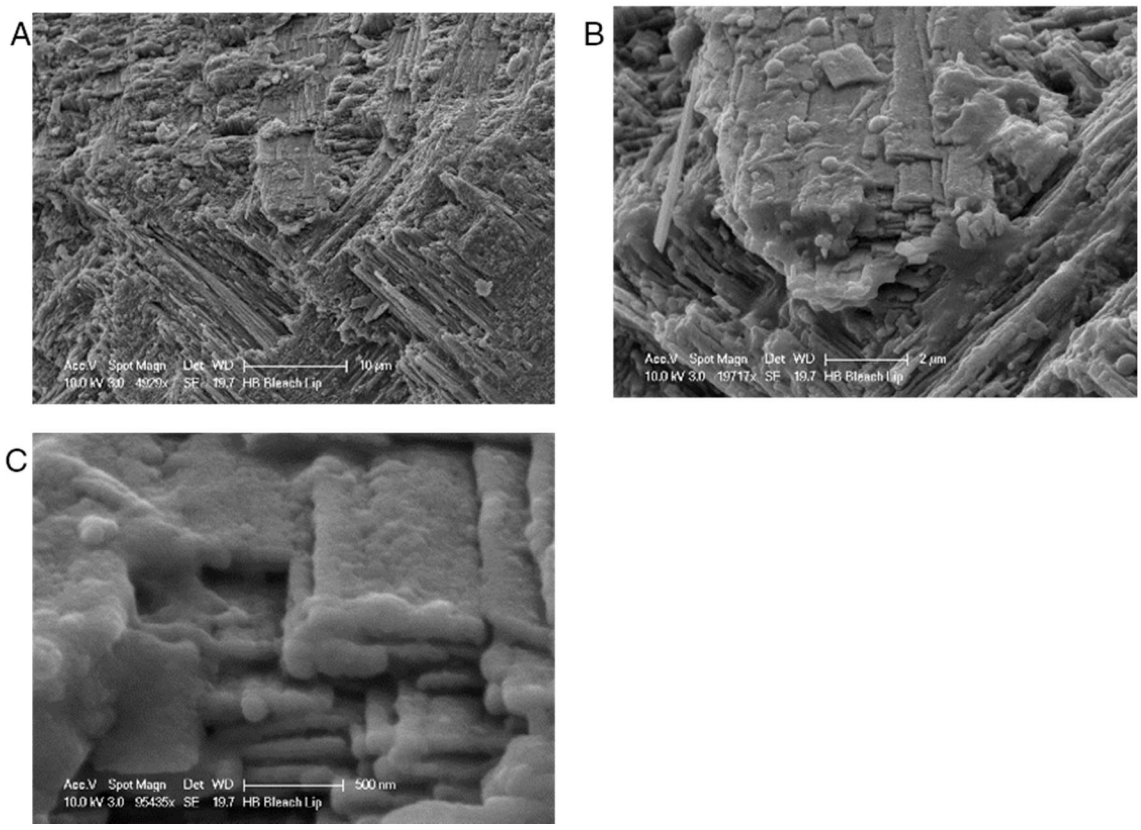

Figure 2-24 The transition from middle to outer crossed lamellar layers in a *H. brasiliana* shell, fractured near lip and treated with sodium hypochlorite to remove soluble organic material (A). At the interface between 0th order crossed lamellar layers, 2nd order lamellae interpenetrate each other forming a complex woven interface (B). At the ends of interpenetrating 3rd order lamellae there is an agglomeration of 4th order, thickening the 3rd order rod. There are additional 4th order spheroids present that fill the void space in this region (C).

2.2.7. **Interfaces 1st Order**

The individual crossed lamellar shell layer, the 0th order, is composed of numerous 1st order sheets. Fracture within 0th order lamellae is described by two directions, the easy and the hard. The hard direction is load applied in the plane of the 1st order lamellae, with a component of the force acting along the length of the 2nd order lamellae. The weak direction is orthogonal to 1st order lamellae, and acts to separate the 1st order sheets. The interfaces between 1st order lamellae are responsible for resisting delamination during loading and acts to transfer load

between 1st order lamellae. In the *H. brasiliana* shell, a number of different 1st order interfacial morphologies are observed and represent differing degrees of interpenetration between 1st order layers (Figure 2-25) At small to moderate displacements, the 1st order lamellae interlock through undulations in the cross section of 3rd order lamellae. For higher degrees of interdigitating, when the amplitude of the undulations is greater than the width of 3rd order lamellae, the interface appears as a dense interwoven region composed of agglomeration of 4th orders (Figure 2-26 A and B). The relative strength of the 1st order interface to the inter-3rd order bonding strength can be observed in fractured sections of the crossed lamellar shell. Fractures along the 1st order interface within the *H. brasiliana* shell occur frequently and result in regions that have rough surface with a topography that is a remnant of the two orthogonal fiber directions (Figure 2-26 D). Similar fractures in the shell of *Strombus gigas* frequently have fractures within 1st order lamellae, causing debonding among the 3rd order lamellae, indicating that the 1st order interfacial strength is greater for the crossed lamellar of *Strombus gigas*.

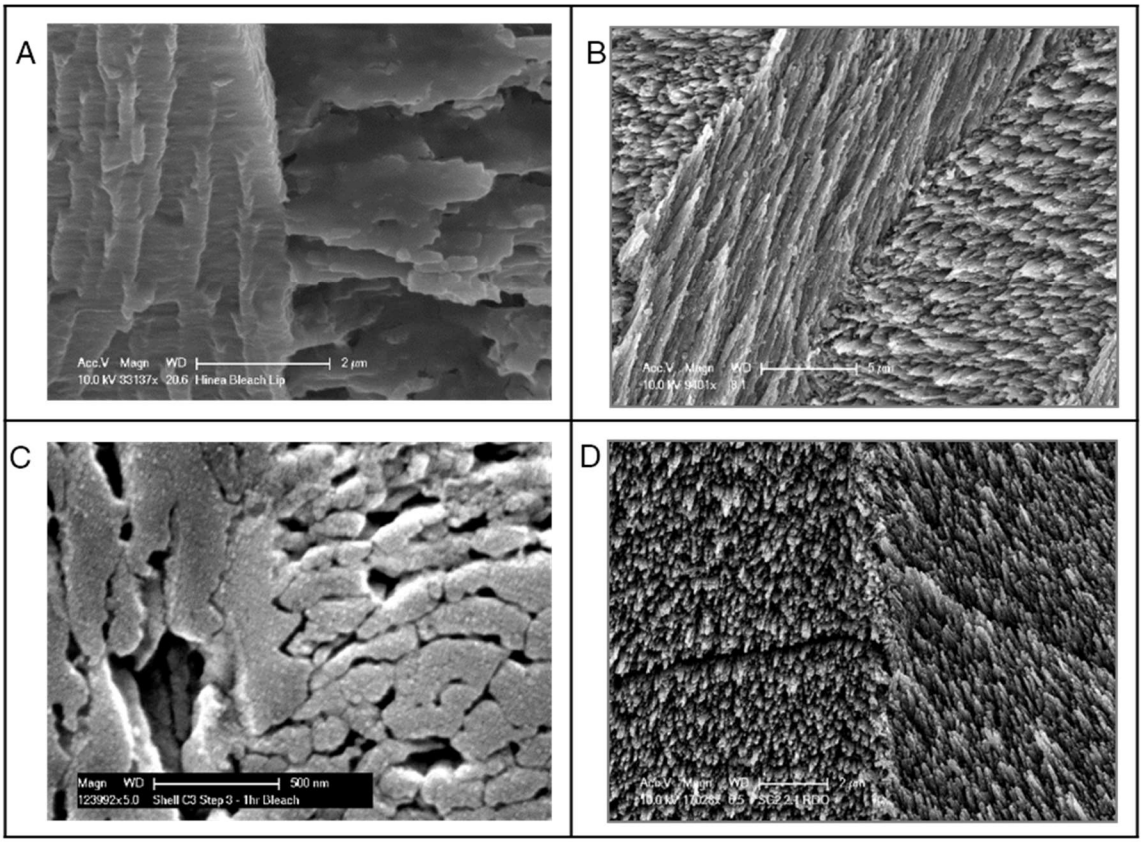

Figure 2-25. Multiple types of 1st order interfaces present in the shell of *Hinea brasiliana*. Abrupt and smooth interface in (A, Sodium Hypochlorite Treated) and (B, RDO Treated). Interdigitating 3rd and 4th order features at 1st order interface in (C, Sodium Hypochlorite Treated) and (D, RDO Treated).

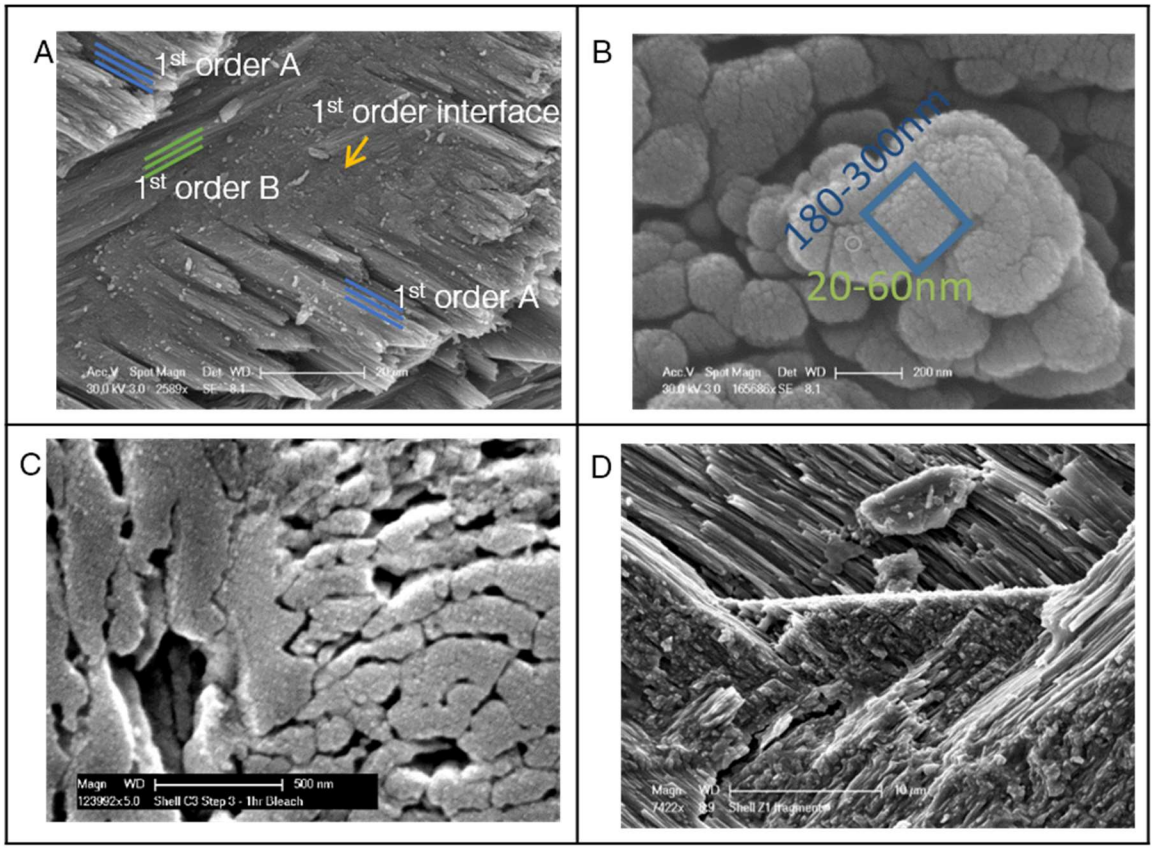

Figure 2-26. Interface between 1st order in new growth region from the shell lip of *Hinea brasiliana* (A). Short chains of spherical particles (4th order) 180-300nm, which are composed of sub particles 20-60nm (5th order)(B). Graded ordering from interface of 1st order(C). At the interface there is an interdigitated structure, composed of short agglomeration of 4th order that typically occurs along 3rd order directions (D).

2.2.8. **Elastic Modulus and Hardness**

The elastic modulus and hardness of the *H. brasiliana* shell were measured using nanoindentation on a polished cross-section from the first whorl and perpendicular to the G direction (Figure 2-27). Nanoindentation is a technique that measures the force to displace a sharp stiff probe into a material. The elastic modulus and indentation hardness can be determined from the force and displacement data as the probe is unloaded from the material. The hardness is measured from the max load observed and the contact area of the probe. The

elastic modulus of the material is determined by the contact stiffness during unloading.

The mechanical properties measured with nanoindentation varied across the three crossed lamellar layers of the shell. The elastic modulus decreases from the 120GPa in the inner crossed lamellar region to 70 GPa in the outer crossed lamellar layer. The hardness varied across all three of the crossed lamellar layers, and correspond with our observations of the orientation of the microstructure from optical and electron microscopy. The inner crossed lamellar layer has the highest average hardness of 5.5GPa, while the middle crossed lamellar layer has the lowest average hardness, 2.5GPa. The mechanical properties reported for indentation of other crossed lamellar shells typically range from 60-120 GPa and 2-6 GPa for elastic modulus and hardness respectively. Indentation of *Strombus gigas* shell found that the hardness varied with orientation of the crossed lamellar layer (*18*). In the commarginal alignment found in the inner and middle layer, the alignment of the c-axis of the aragonite shell mineral is responsible for the differing hardness value arising from the biaxial nature of aragonite causing anisotropic mechanical properties.

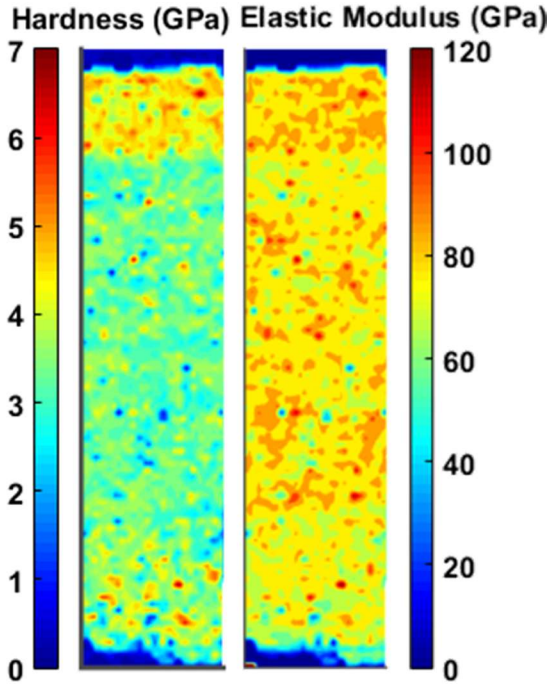

Figure 2-27. Nanoindentation maps of the Hardness (A) and Elastic Modulus (B) from a cross section of the first whorl of a *H. brasiliana* shell.

2.3. Crystallography of *H. brasiliana* by Synchrotron X-Ray Diffraction

2.3.1. Introduction to Two dimensional X-Ray Diffraction (2D-XRD)

An X-ray beam from a synchrotron beamline was used to investigate the phase, size, and orientation of the crystalline mineral of the crossed lamellar structures found within the *H. brasiliana* shell. The crystallographic properties of the *Hinea* shell were mapped using a 19KeV x-ray beam with a 100µm spot size. The incident x-rays interact with and are scattered by the sample mounted on a computer controlled motorized stage. The intensity of the scattered light is detected on a two dimensional planer CCD detector (Figure 2-28).

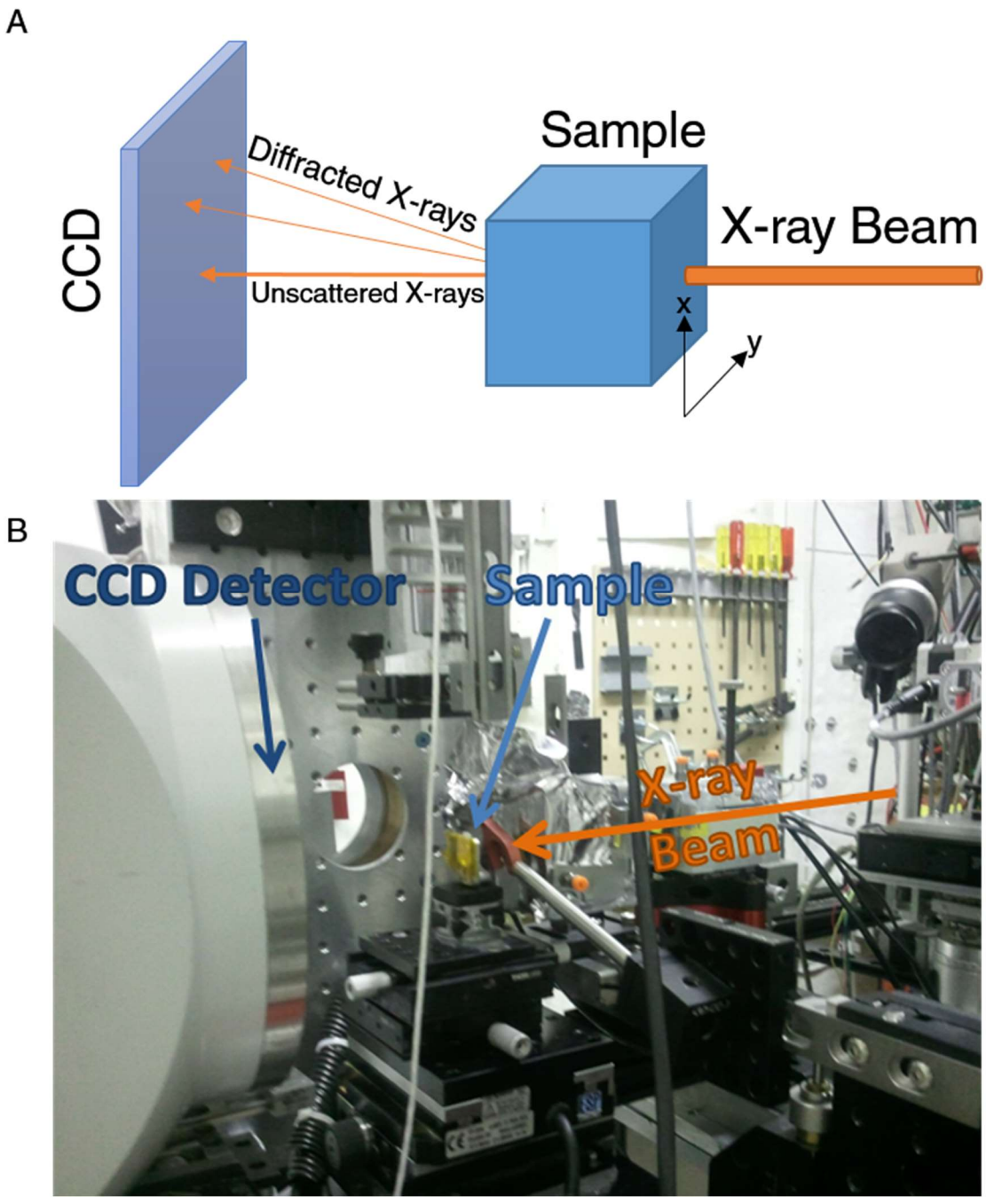

Figure 2-28. Schematic of beamline setup used for 2D-XRD (A). X-13B Beamline at NSLS at Brookhaven National Laboratory. Sample is mounted on motorized XY stage to allow for the translation of the sample perpendicular to the beam direction (B).

When X-rays interact with crystalline material, they are scattered by diffraction due to the periodic spacing of elements in crystalline materials. The

diffracted x-rays are deflected from the path of the incident x-ray. The angle of deflection is dependent on the wavelength of the x-ray source, λ, and the specific interplanar spacing along a certain direction of the crystal lattice of the structure, d_{hkl}. This relation was reported in 1914 by Bragg and is known as Bragg's law (Equation 2-1) (*19*).

$$2d_{hkl}\sin(2\theta) = n\,\lambda$$

Equation 2-1 Bragg's law, relating the scattering angle with the wavelength of the incident light and the characteristic length of the periodic spacing in the structure.

The orientation of the crystallites dictates the orientation and intensity of diffracted light for the different lattice planes of the crystal. The appearance of diffracted beams can be determined through an Ewald construction (*20*) (Figure 2-29) The Ewald sphere is centered about the crystallite and has a radius of $1/\lambda$ and exists in reciprocal space. To determine which lattice planes of the crystallite satisfy Bragg's law (Equation 2-1), the reciprocal lattice for the crystallite is drawn with its origin at the intersection the incident x-ray beam and the Ewald Sphere. Reciprocal lattice points that intersect with the Ewald sphere satisfy the conditions of Bragg's law. X-rays that are diffracted pass through the reciprocal lattice point. The occurrence of x-ray diffraction within a sample depends on the lattice d-spacing, the distribution of crystallite orientations, and the wavelength of the x-ray source. For samples with uniform random distribution of orientations, each reciprocal lattice point forms a sphere with radius d^*_{hkl}. The intersection of the reciprocal lattice point sphere and the Ewald sphere forms a ring, which is projected on to the detector. A non-uniform distribution of crystallites results in arcs

along the Ewald sphere, which can be used to determine the angular distribution within the sample. Figure 2-30A shows an example of the arcs produced by a textured crystalline sample and recorded by a 2D area detector.

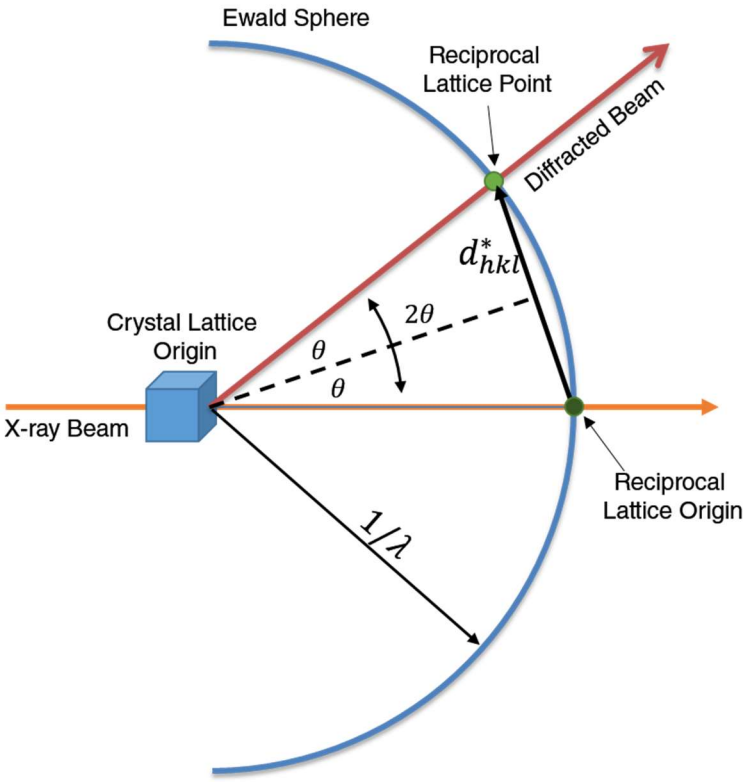

Figure 2-29. The Ewald construction. The Bragg diffraction condition is satisfied for reciprocal lattice points that intersect the Ewald Sphere. The Ewald sphere is centered at the crystallite and has radius $1/\lambda$. The reciprocal lattice point has its origin at the intersection the Ewald sphere and the transmitted x-ray beam. The reciprocal lattice point distance is d^*_{hkl}.

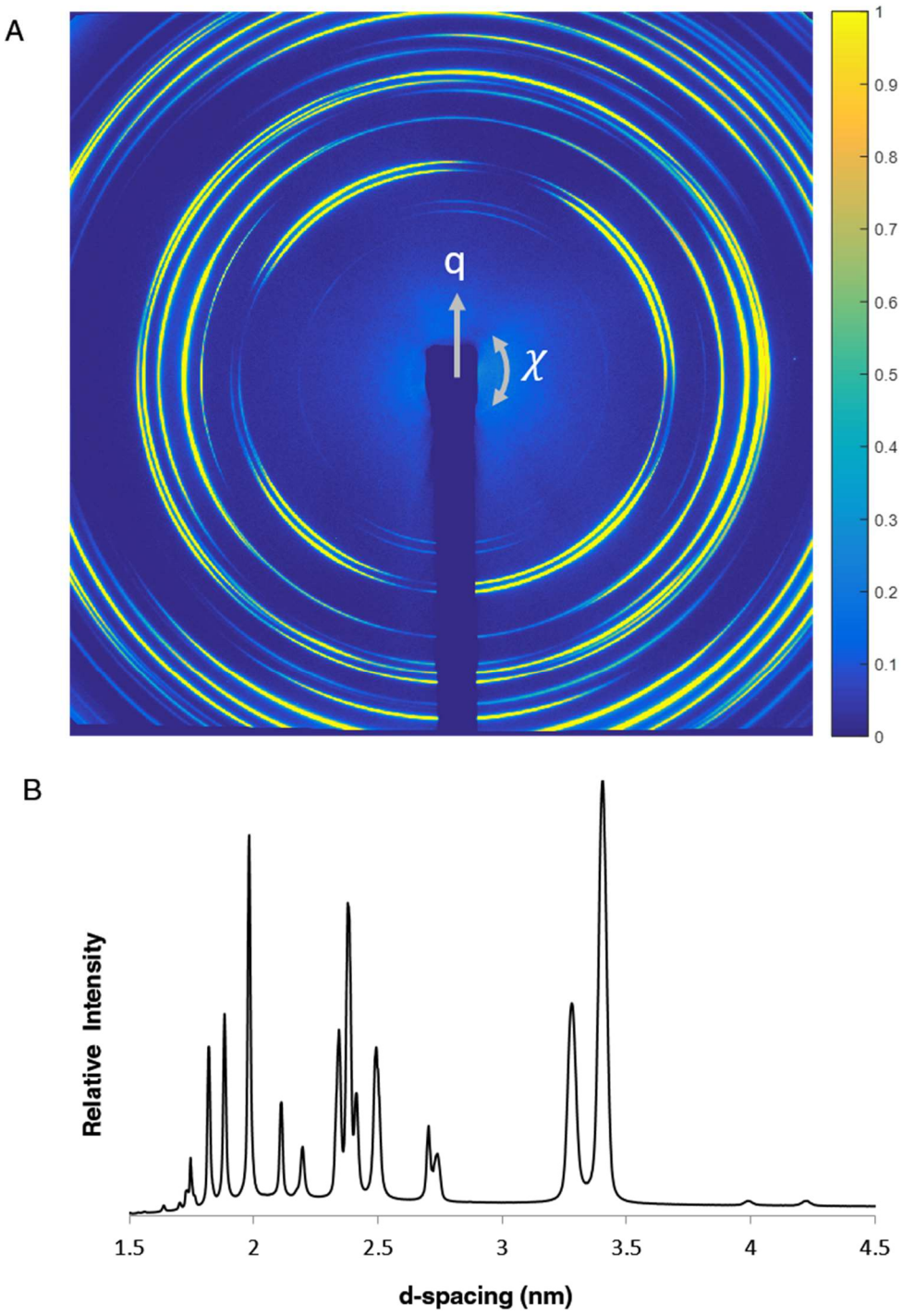

Figure 2-30. Representative 2D-XRD pattern (Frame #88) from *H. brasiliana* with scattering vector (q) and orientation angle (χ) (A). 1D XRD pattern, obtained by summation of the intensity around χ (B).

2.3.1. X-Ray Transmission Map

An x-ray transmission map was produced from an apertural cross section of an adult *Hinea brasiliana* shell (Figure 2-31 A). The transmission map was then used to determine the locations for collecting x-ray diffraction data. A 12x24 map of diffraction patterns were gathered from a cross-section of the first whorl of the shell using a 100µm beam and step size (Figure 2-31 B).

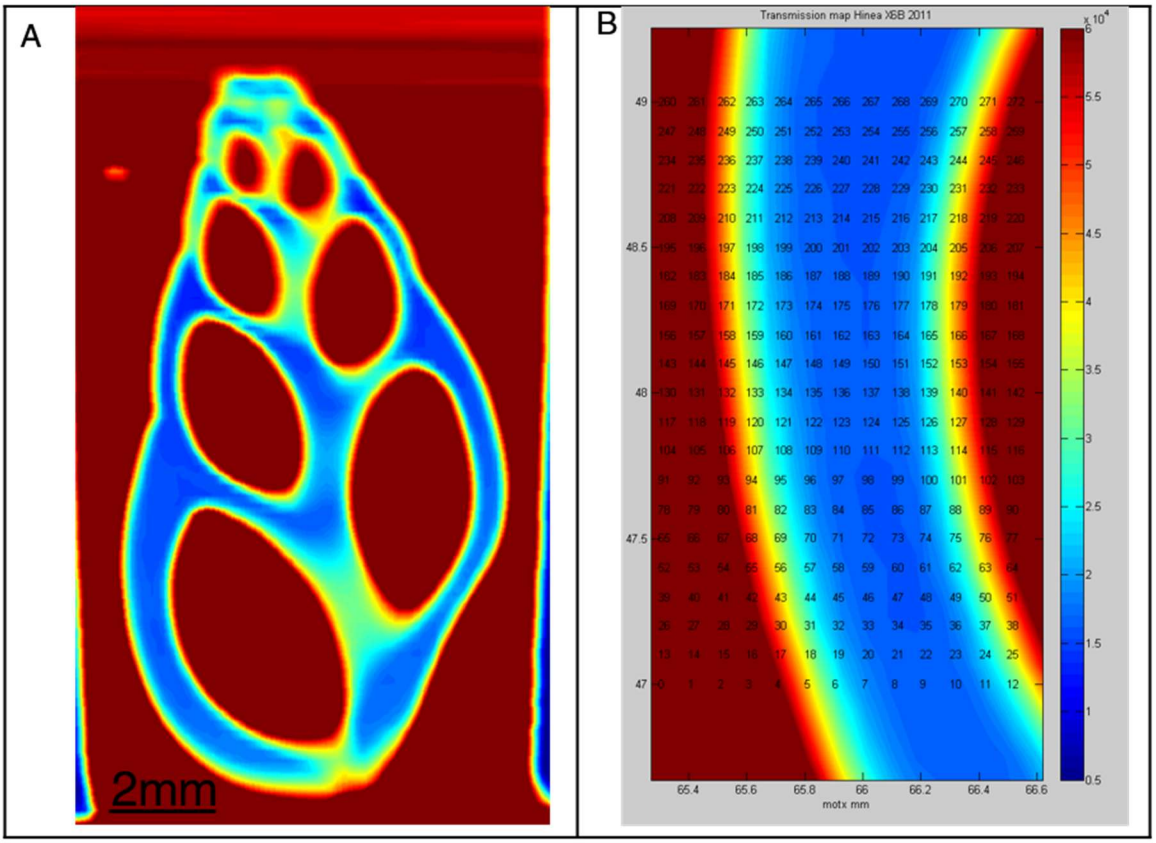

Figure 2-31. X-ray transmission map collected from cross section of *H. brasiliana* shell (A). Location of the individual frames collected from the 1st whorl of the shell (B).

2.3.2. Mineral Phase

A series of 273 diffraction patterns from the *H. brasiliana* shell were analyzed for the mineral phase present. The mineral phase of the shell was

determined to be solely composed of aragonite. Calcite was not detected within any of the shell layers (Figure 2-32). The sole presence of aragonite is typical for caenogastropods, while calcite is commonly found in Vetigastropoda (*7, 21*).

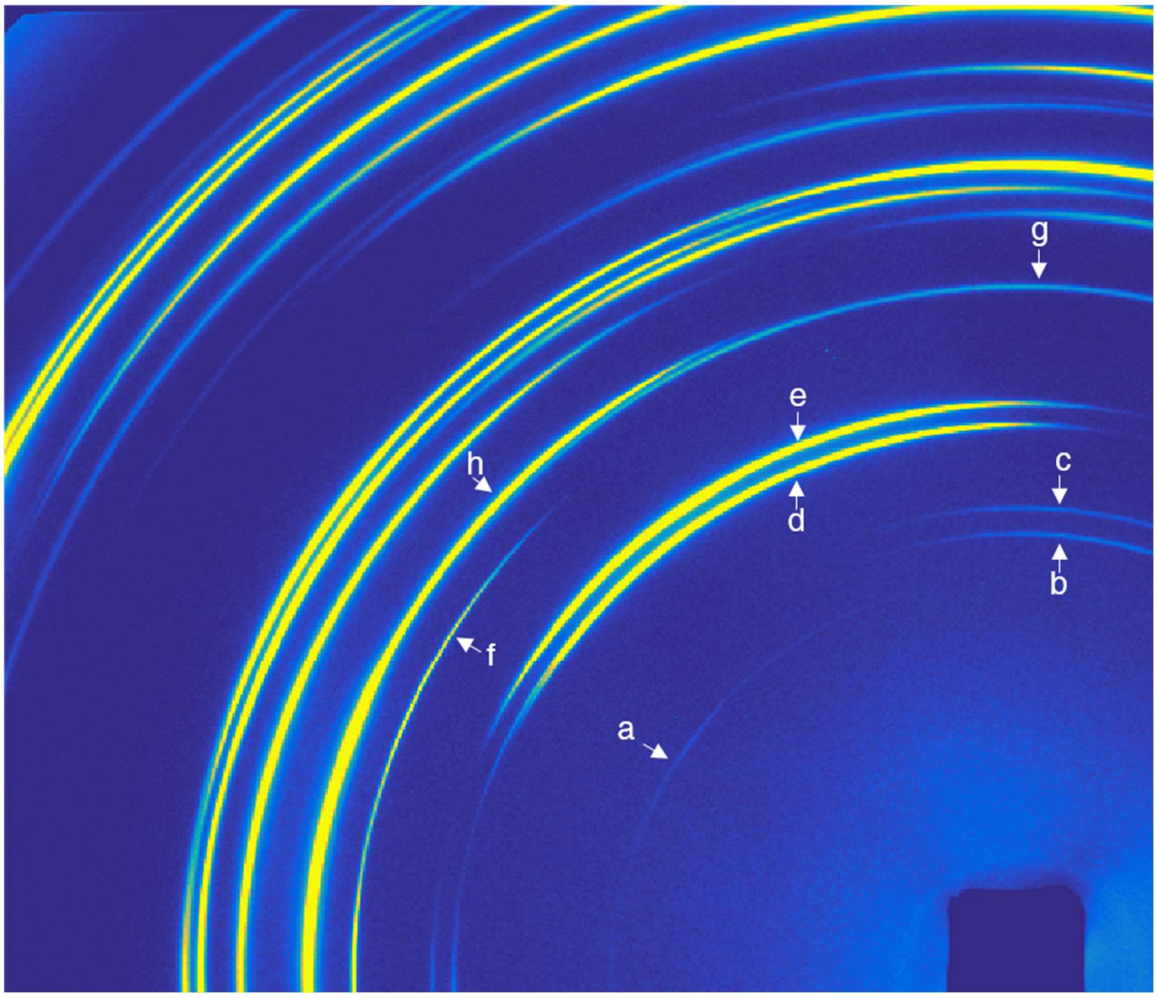

Figure 2-32. Partially indexed enlarged region of a representative 2D-XRD pattern (Frame #88). The 2D-XRD enables the resolution of reflections that have similar lattice spacing but have different orientations in well textured samples. All of the observed reflections were identified as aragonite, the first eight reflections are 011(a), 110(b), 020(c), 111(d), 021(e), 002(f), 121(g), 012(h).

2.3.3. **Crystal Size**

The size of crystallites was measured from diffraction patterns by the full width at half maximum of the reflection using the Scherer equation (*22*). The

crystallite size measured from the (111) reflection ranged from 3.5-5.5nm, with smaller crystallites found in outer regions. In addition, the size of crystallites in the middle layer was observed to vary with along the marginal direction of the shell. The measured crystallite size from x-ray diffraction is smaller than the 5th order particles that were observed by scanning electron microscopy, suggesting that there are further hierarchal features within the crossed lamellar structure.

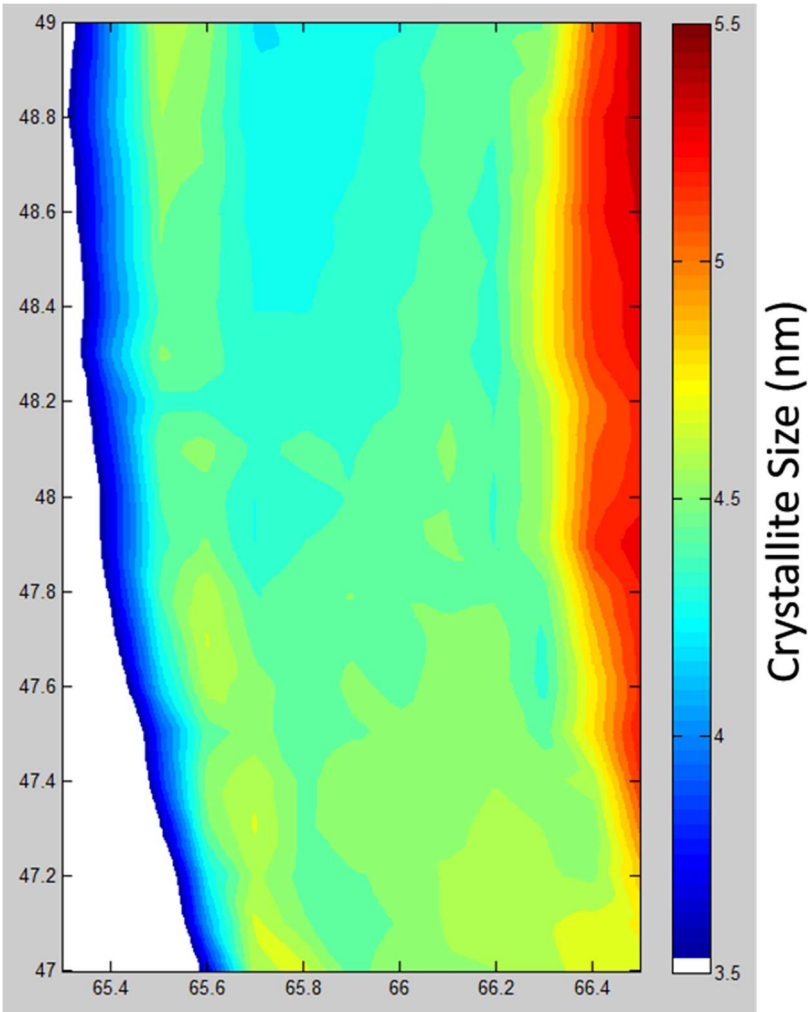

Figure 2-33. Crystallite size from the (111) lattice of aragonite from a map of 273 diffraction patterns collected from the 1st whorl of the *Hinea brasiliana* shell.

2.3.4. **Crystallite Orientation**

The three crossed lamellar layers within the shell of the *Hinea brasiliana* have distinct diffraction patterns from the unique crystallography of the crossed lamellar structure and the rotation of the crossed lamellar structure between adjacent shell layers.

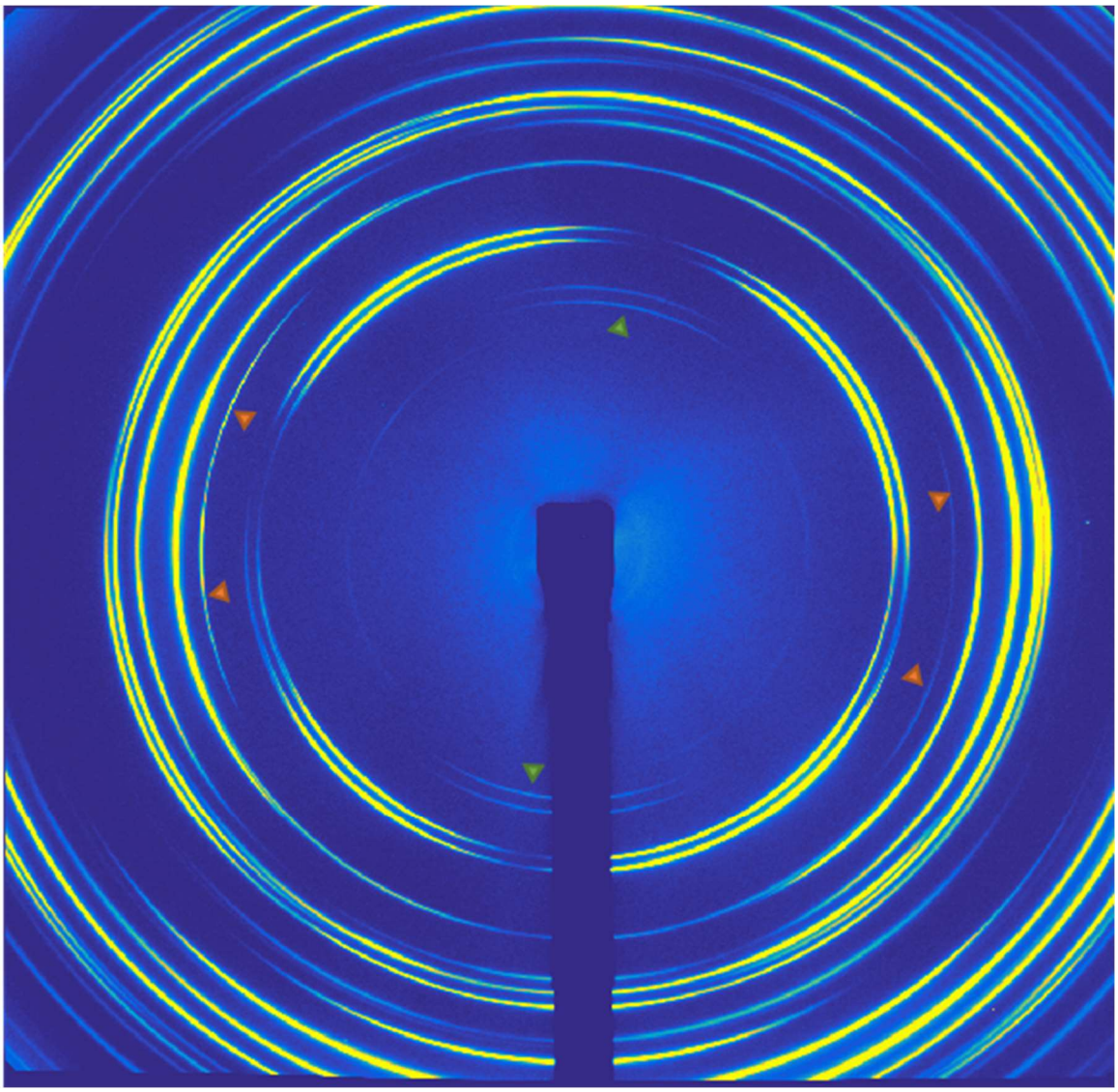

Figure 2-34. 2D-XRD frame (#88) from the inner crossed lamellar layer of *H. brasiliana*. Two pairs of (002) reflections are present (Orange triangles). and one pair of (110) reflections (Green triangles).

The diffraction patterns show distinct arching from well-defined crystalline texture of the crossed lamellar structure, even through relatively thick sections of the shell, an estimated 500 million 3rd order lamellae in the area of each diffraction pattern. In the inner crossed lamellar layer the two pairs (002) reflections are observed. In addition, the (002) and (110) form arcs over a narrow range of angles, suggesting that there are two groups of crystallites with a narrow angular distribution and with a small angle between the two groups (Figure 2-34).

The (002) reflections are not present in the diffraction patterns from the middle crossed lamellar layer (Figure 2-35). (002) reflections are present, but have a decreased intensity in the outer crossed lamellar layer (Figure 2-36). The (002) reflection is rotated out of the plane of the detector during the rotation between crossed lamellar shell layers. The intensity of the (002) reflection was measured for each of the diffraction patterns and was found to be greatest in the inner

crossed lamellar layer, followed by the outer layer, and below the detection threshold in the middle crossed lamellar region (Figure 2-37). The varying degree

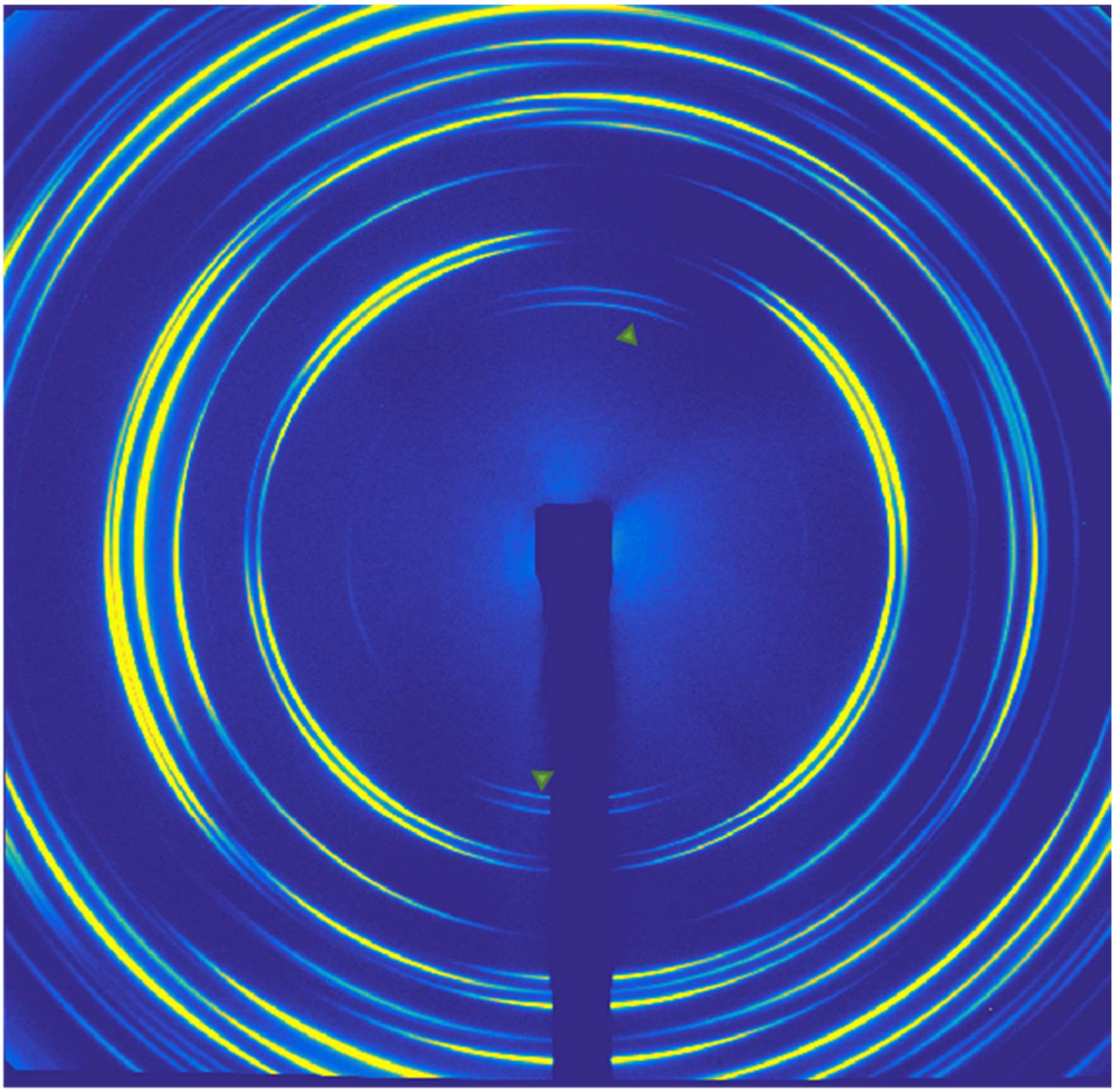

Figure 2-35. 2D-XRD frame (#85) from the middle crossed lamellar layer of *H. brasiliana*. 110 reflections indicated (green triangles), 002 reflection is not present in this layer.

of in-plane (002) alignment observed via XRD corresponds with the trends in hardness measured for each of the shell layers by nanoindentation (Figure 2-27).

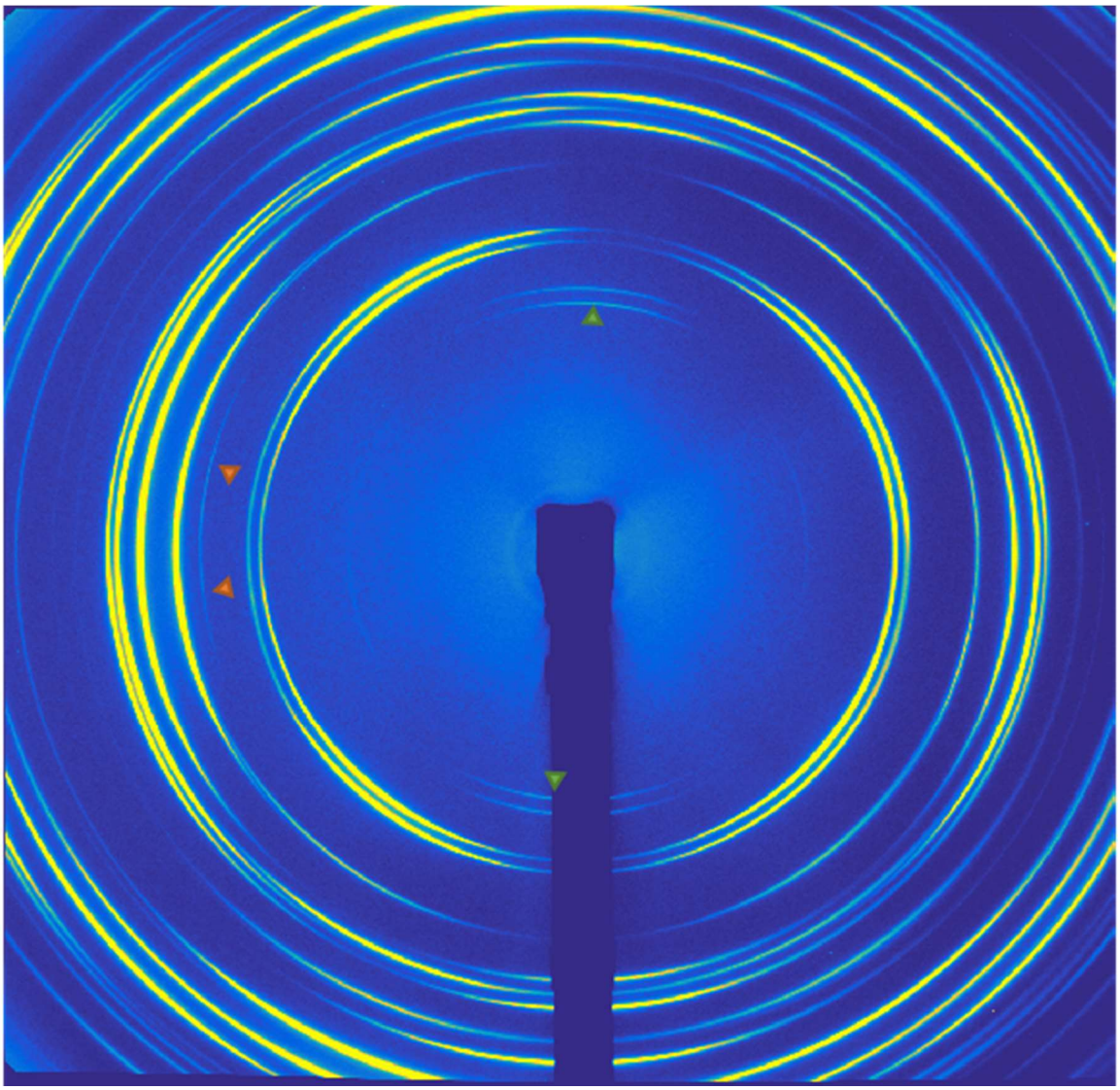

Figure 2-36. 2D-XRD frame (#82) from the outer crossed lamellar layer of *H. brasiliana*. Two pairs of (002) reflections are present (Orange triangles) and one pair of (110) reflections (Green triangles).

The distribution of the (002) reflection varies along the χ direction. When present the (002) reflections are found in groups of two that are symmetrical about

the radial direction of the shell. From the inner layer the angle between the (002) reflections was measured to be 26°. The angle for the outer layer is approximately the same (Figure 2-38). The angle measured between the two observed c-axis is smaller than the angle between 3rd order lamellae in the crossed lamellar structure, which have nearly orthogonal directions.

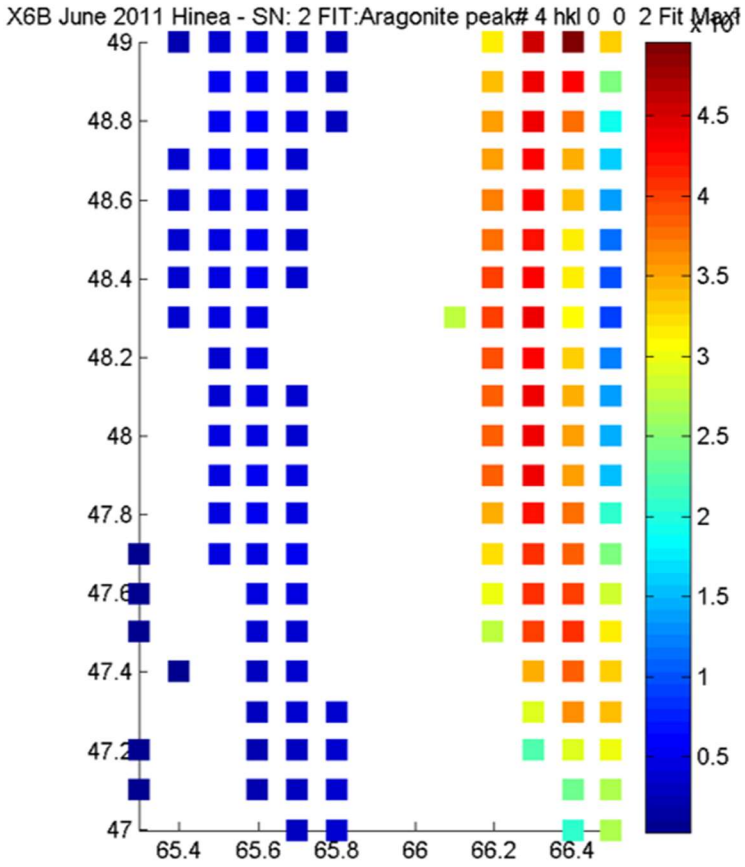

Figure 2-37. Maximum intensity of the (002) reflection from diffraction map of *H. brasliana*. Intensity values in the middle region were below the background threshold value.

The (002) reflections in the inner and outer crossed lamellar layer show a high degree of asymmetry in their intensity, with in many cases the opposite reflections, 180° away, are not observed. This indicates that the reciprocal lattice

vector is not orthogonal to the x-ray beam, and there is a degree of tilt. The tilting of the reciprocal lattice vector causes one reciprocal lattice point to move towards the Ewald sphere, while the opposite point moves further away? from the Ewald sphere.

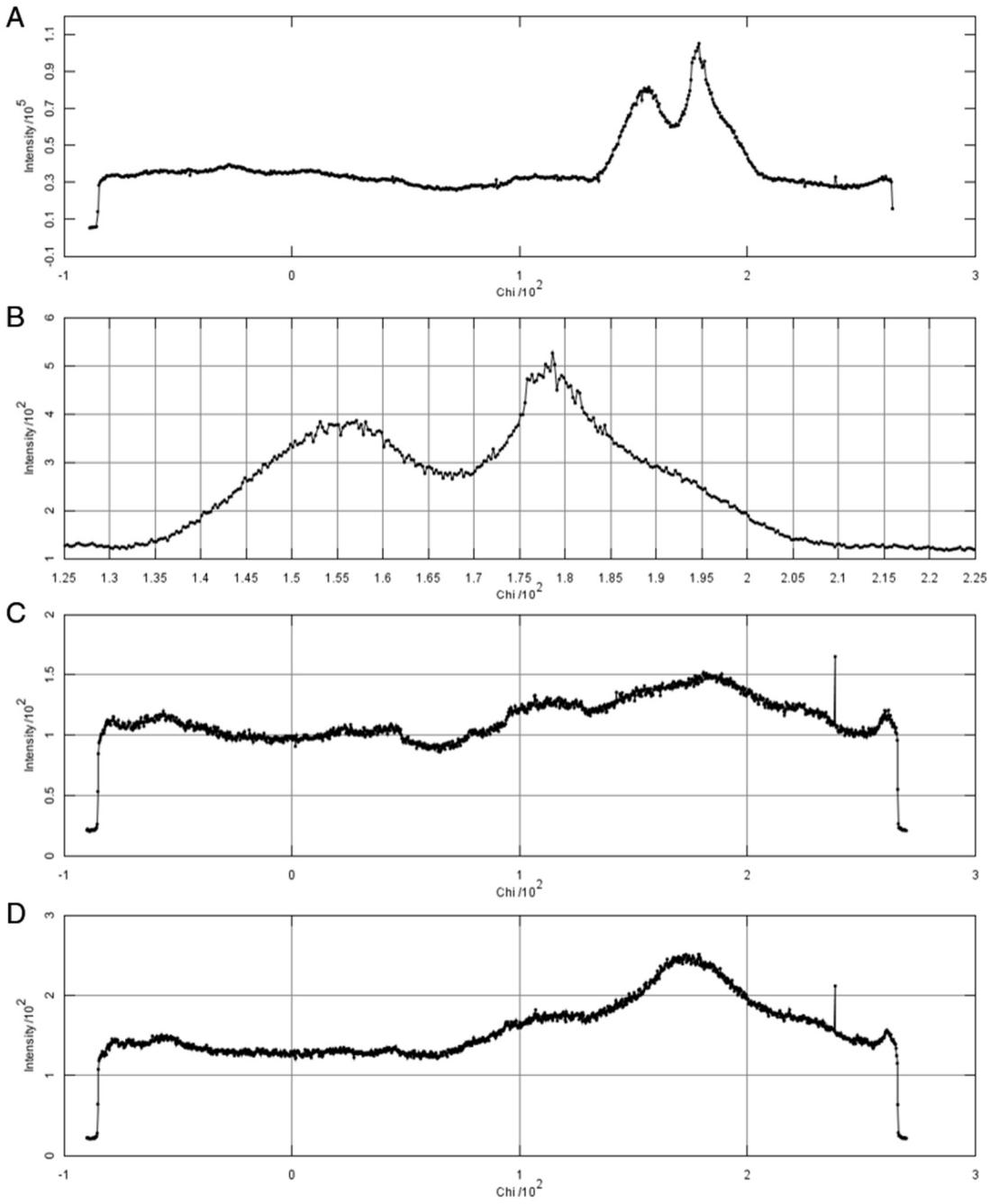

Figure 2-38. Intensity vs. χ plots for the three shell layers, inner (A), middle (C), and outer (D). A pair of intense (002) reflections from the inner crossed lamellar layer, 26° spacing between the centers of each group (B).

2.3.1. Crystalline Textures of Mollusk Shells

The relationships between observed microstructure and crystallography have been investigated for a number of different biogenetic mineral systems. Biologically mineralized structures often have unique, well ordered microstructures that differ significantly from those that occur in abiotic mineral systems. A thorough investigation into the morphological and crystallographic relationships within the many diverse mollusk shell structures has been carried out by Chateigner *et al*. (*7*). It was found that in all of the mollusk shell microstructure types, there was some degree of variability in the orientation of c-axis and a-axis. The crossed lamellar structure showed the highest degree of variability in observed textures and orientations. The large variability in the crossed lamellar structure is due in part from the multiple origins of the microstructure within the different classes of mollusk (Figure 2-39).

In the crystallographic arrangement of crossed lamellar from caenogastropods, the c-axis is commonly reported to be inclined from the long axis of the 3rd order lamellae. Adjacent 1st orders, with perpendicular dip directions, are aligned with parallel (110) planes which are coplanar with the interface between 1st order lamellae (Figure 2-40). In the shell of the *Conus marmoreus* the c-axis of 3rd order lamellae in adjacent 1st orders, were found to be separated by 30°, in contrast to the nearly 90° between 3rd order lamellae. Within the 3rd order lamellae there are numerous (110) twin planes that are parallel to 1st order interface and are continuous along the length of the 3rd order lamellae, and span across the

boundary of 4th order features (Figure 2-41 B). Twinning along the (110) occurs at the highest rate in the crossed lamellar microstructure of gastropods, and is significantly higher than gastropod nacre and crossed lamellar from other classes (*23*) (Figure 2-41 A).

Taxon	Layer microstructure	c-axis	a-axis	Direction from G	V_T (%)	$\{001\}_{max}$ (m.r.d.)	F^2 (m.r.d.^{2})
Bivalves							
Acila castrensis	ISN	⊥	*	<100>, 90	-	63	88
Anodonta cygnea	ISN	⊥	*	<100>,125	38	49	49
	OFSP	⊥	O	-	-	18	7.1
Atrina maurea	ISN	⊥	*	<100>, 160	67	>100	241
Bathymodiolus thermophilus	ISN	⊥	*	<100>, 90	57	84	65
Fragum fragum	ICL	∀, 15	×	<110>	100	49	46
Glycymeris gigantea	ICL	∀, 15	×	<110>	100	35	55
Lampsilis alatus	ISN	⊥	*	<100>, 90	38	>100	175
Mytilus californianus	ISN	⊥	*	<100>, 90	65	25	77
Mytilus edulis	ISN	⊥	*	<100>, 90	52	>100	51
Neotrigonia sp.	ISN	⊥	*	<100>, 90	18	>100	210
Pinctada margaritifera	ISN	⊥	*	<100>, 90	12	>100	>9999
Pinctada maxima	ISN	⊥	*	<100>, 90	21	>100	746
Pinna nobilis	ISN	⊥	*	<100>, 95	38	>100	>9999
Pteria penguin	ISN	⊥	*	<100>, 120	23	>100	429
Spondylus princeps	RCL	⊥	O	-	-	>100	164
	ICL	⩒, 10	×	<110>, 105	100	37	47
Sunetta solanderii	ICL	⊥	O	-	-	>100	177
	OFSP	∠, 20	O	-	-	40	44
Tapes japonica	IRCL	⊥	O	-	-	>100	130
Cephalopods							
Nautilus macromphalus	ICN	⊥	*	<100>, 100	50	>100	333
	OH	⊥	*	<100>, 75	50	65	16
Nautilus pompilius	ICN	⊥	*	<100>, 75	92	51	51
Gastropods							
Cellana testudinaria	IICCL	⊥	×	<100>, 120	-	-	-
Conus leopardus	ICL	⊥	×	<100>, 30	94	52	201
	ORCL	⊥	O	-	-	5	29
Cyclophorus woodianus	IRCL	⊥	|	<100>, 20	0	>100	297
	ORCL	⊥	O	-	-	-	-
Cypraea mus	ISP	⊥	*	<100>, 45	-	-	-
	RCL	⊥	×	<100>, 60	-	-	-
	OCL	⊥	×	<100>, 105	92	63	118
Cypraea testudinaria	ICL	⩒, 15	|	<100>, 10	-	>100	432
	RCL	∀, 25	×	<110>, 75	92	28	32
	CL	⊥	*	<100>, 90	-	28	41
	OH	∀, 15	*	<100>, 90	26	55	78
Entemnotrochus adansonianus	ISP	⊥	O	-	-	-	-
	CN	⊥	O	-	-	-	-
	OICP	⊥	O	-	-	-	-

Euglandina sp.	IRCL	⊥	|	<100>, 80	0	>100	307
	OCL	⊥	|	<100>, 120	0	23	40
Fissurella oriens	IICCL	⩔, 20	*	<110>	83	33	76
Haliotis cracherodi	ICN	∠, 15	O	-	-	>100	90
Haliotis rufescens	ICN	⊥	O	-	-	-	-
Helix aspersa (A)	OCL	⊥	|	<100>, 90	0	38	80
(B)	OCL	⊥	|	<100>, 90	0	42	92
Helix pomatia	OCL	⊥	|	<100>, 90	0	55	105
Helminthoglypta nickliniana anachoreta	OCL	⊥	*	<100>, 90	18	45	103
Muricanthus nigritus	ICL	⊥	×	<100>, 140	94	86	119
	OCL	⊥	×	<100>, 125	98	32	46
Nerita polita	ICL	∠, 25	*	<100>	88	29	27
Nerita scabricosta	IICCL	⊥	O	-	-	34	26
Oliva miniacea	OCL	⊥	×	<100>, 30	100	45	103
	OH	⊥	*	<100>, 115	17	>100	526
Perotrochus quoyanus	ICN	⊥	O	-	-	-	-
	OICP	⊥	O	-	-	-	-
Phasianella australis	CL	⊥	O	-	-	18	8.7
	OICP	⊥	O	-	-	-	-
Scutellaster tabularis	IRCL	⩔, 25	×	<110>, 100	100	42	76
Scutus antipodes	CL	⩔, 15	×	<110>, 5	27	23	34
	ICCL	⊥	*	<100>, 30	88	23	18
Tectus niloticus	ICN	⊥	O	-	-	>100	88
	OSpP	∠, 15	O	-	-	-	-
Tectus pyramis	OSpP	∠, 15	O	-	-	62	26
Turbo petholatus	OICP	⊥	O	-	-	26	17
Viana regina	IICCL	⊥	O	-	-	64	68
	OCL	⊥	O	-	-	18	10
Monoplacophoras							
Neopilina galatheae	ISN	⊥	O	-	-	-	-
	OSP	⊥	O	-	-	-	-
Rokopella zographi	ISN	⊥	O	-	-	-	-

Figure 2-39. Table summarizing the crystallographic textures observed in the mineralized structures of numerous different orders of Mollusca. There is significant variation in the crystallography between species with similar microstructures. Chateigner *et al.* (*7*)

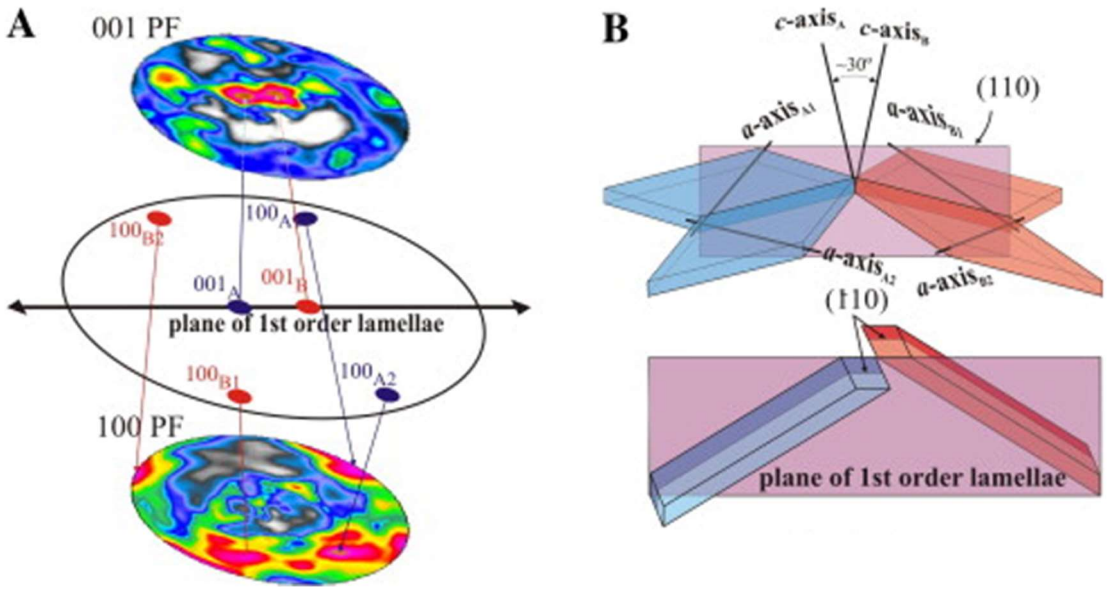

Figure 2-40. Texture of aragonite mineral observed in the shell of *Conus marmoreus* (A). The relationship between the observed crystallographic textures microstructure of the 3rd order lamellae (B). From Rodriguez-Navarro, Checa, Willinger, Bolmaro and Bonarski (*24*)

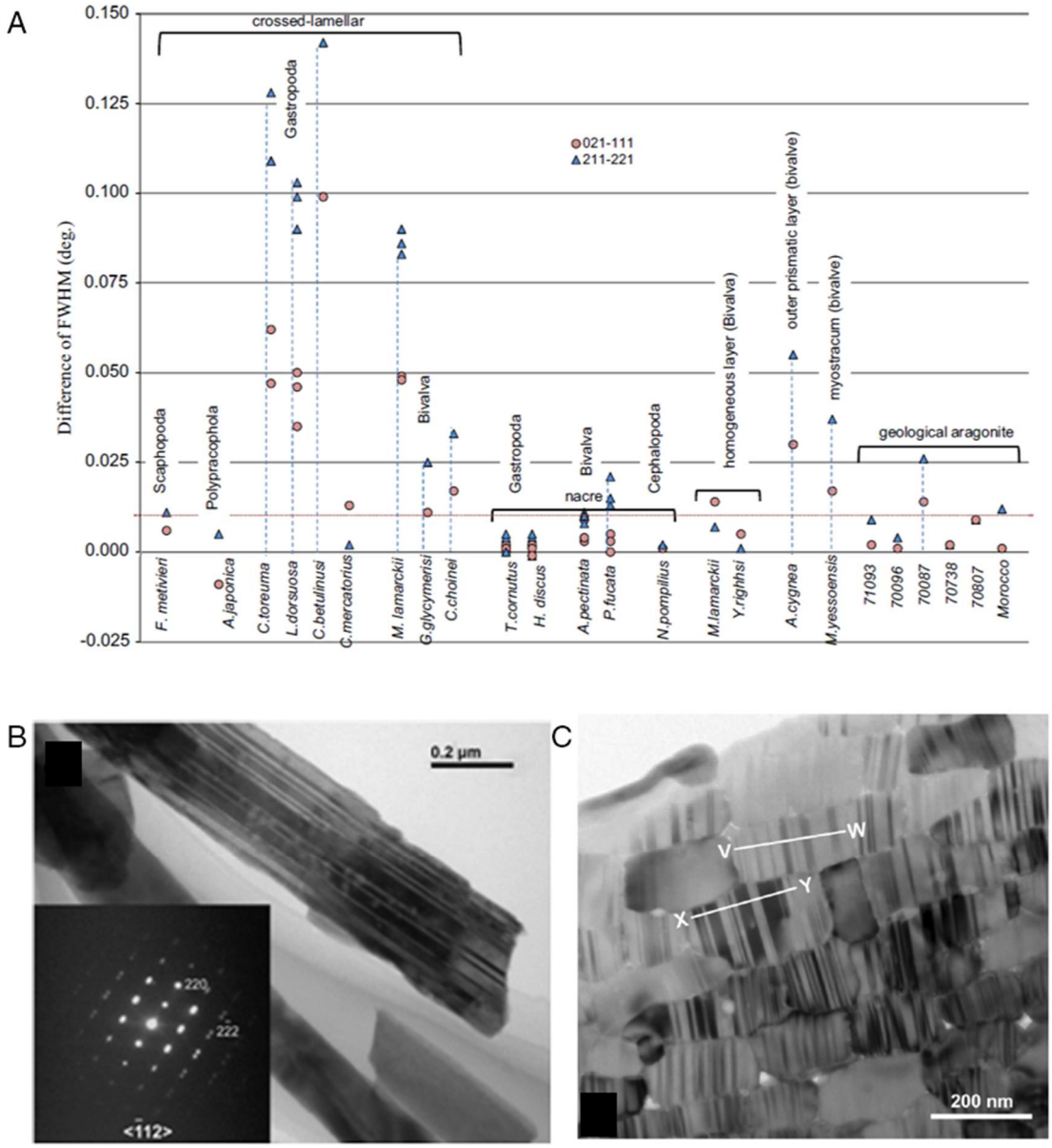

Figure 2-41. Twinning in crossed lamellar. Differences in FWHM indicative of the degree of twinning along the (110) direction for different aragonitic mineral systems (A)(*23*). Transmission electron micrograph showing twin planes running along the length of the 3rd order lamellae from gastropod crossed lamellar. Inset selected area diffraction showing high degree of alignment and doubled reflections from across the twin boundary (B) (*23*). End on view of 3rd order lamellae, showing that the (110) twin planes are parallel within a 3rd order lamellae (C) (*25*).

2.3.1. **Fine Splitting of Reflections**

Fine splitting of specific reflections can be observed with synchrotron x-ray diffraction. The splitting is observed to happen most frequently with reflections that fall along the 111 direction (Figure 2-42). The fine splitting observed is a result of the unique crystallographic arrangement, with the high degree of (110) polysynthetic twin, found in the crossed lamellar structure of gastropods. The fine splitting was only observed in the tail ends of the reflection arcs, and is often unobservable due to the width of reflection and low spatial resolution of conventional laboratory x-ray diffractometers.

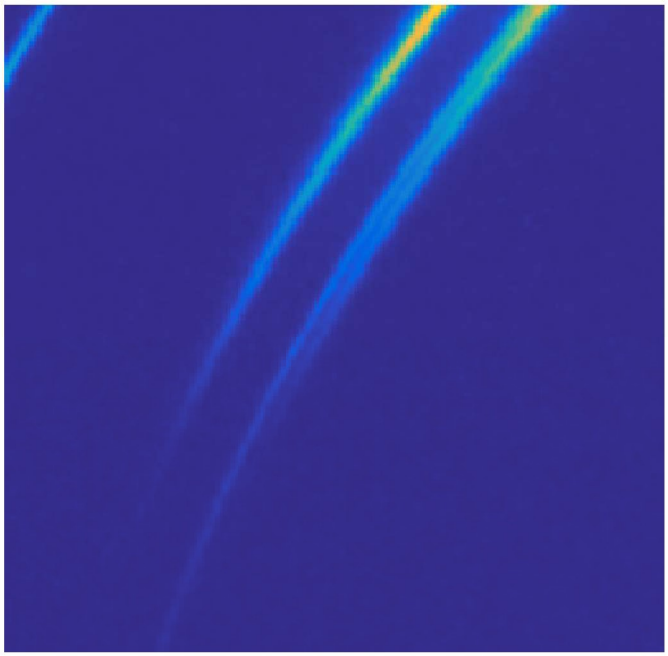

Figure 2-42. Fine splitting of the (111) reflection from the inner crossed lamellar layer of *H. brasiliana*.

2.4. Diffusion of light in *H. brasiliana* and other Crossed Lamellar shells

2.4.1. Transmittance of incident light through *Hinea*

H. brasiliana has two patches of bioluminescent cells along the dorsal region of the mantle, which is confined to the inside of the shell (Figure 2-7 B). The cells in the patches produce a blue-green luminescence. The measured direct transmittance spectrum through the shell has a minimum at 520nm (Figure 2-8), which corresponds to the wavelength of the bioluminescent light produced by the animal, and could correspond to a preferential diffusion of light by the shell. To investigate the diffusion of bioluminescent light through the shell, we simulated the light through a section of the 1st whorl of the shell, using three different (Blue, Blue-Green, and White) LED light source coupled with a 50µm fiber optic cable (Figure 2-5243).

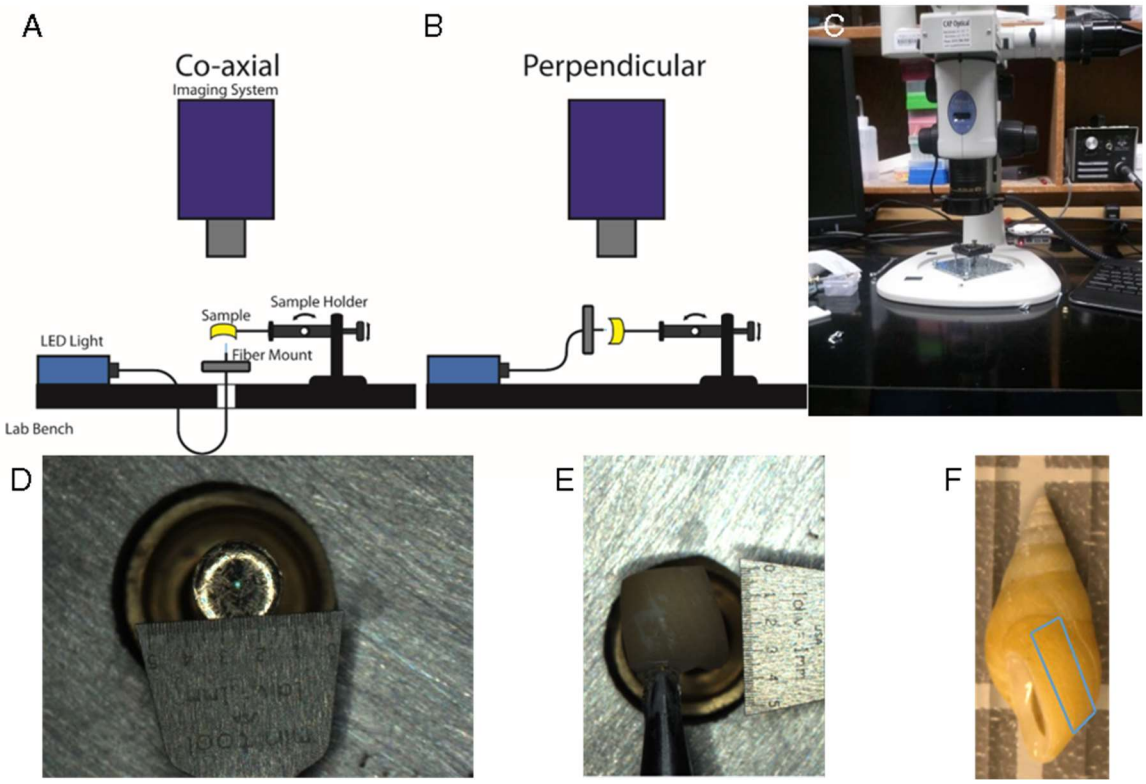

Figure 2-43. Schematic of the configuration of the light source, sample, and microscope for two illuminating conditions, co-axial(A) and perpendicular (B). Sample stage and microscope used in optical testing of *H. brasiliana* shells. Light source and fiber optics run from underneath the bench and are not visible in this view (C). The 50µm fiber optic cable mounted to the sample stage (D). Section of *H. brasiliana* resting on the fiber optic cable (E). Region where the section was obtained from the shell of *H. brasiliana* (F).

The diffusion of transmitted light was observed in the perpendicular orientation with the light source aligned normal to the shells inner surface. During our testing we did not observe a significant dependence on the wavelength of the light source and the diffusion of light through the shell (Figure 2-44). When the inner surface is demineralized with acid, there is a significant increase in intensity of directly transmitted light (Figure 2-44 RDO). After removal of 150µm of material, through the entirety of the inner layer and into the middle, the direct intensity decrease and the diffusion remains unchanged (Figure 2-44 Ground). After washing the ground

surface with Sodium Hypochlorite, to remove residual organic material, the directly transmitted intensity increased significantly (Figure 2-44 Bleach). In all case the intensity was consistent at a distance of 0.53mm from the center of the light source (Figure 2-45). This limit could potentially be due the orientation of the 1st order lamellae and the curvature of the shell, imposing a geometric limit to the area covered by the crossed lamellar fibers from the middle to the outer layer. The removal of the organic structure resulted in a significant increase in the intensity of the directly transmitted light through the shell, approximately four times greater than the untreated shell. The shell is able to diffuse all three light sources to a similar degree regardless of the wavelength.

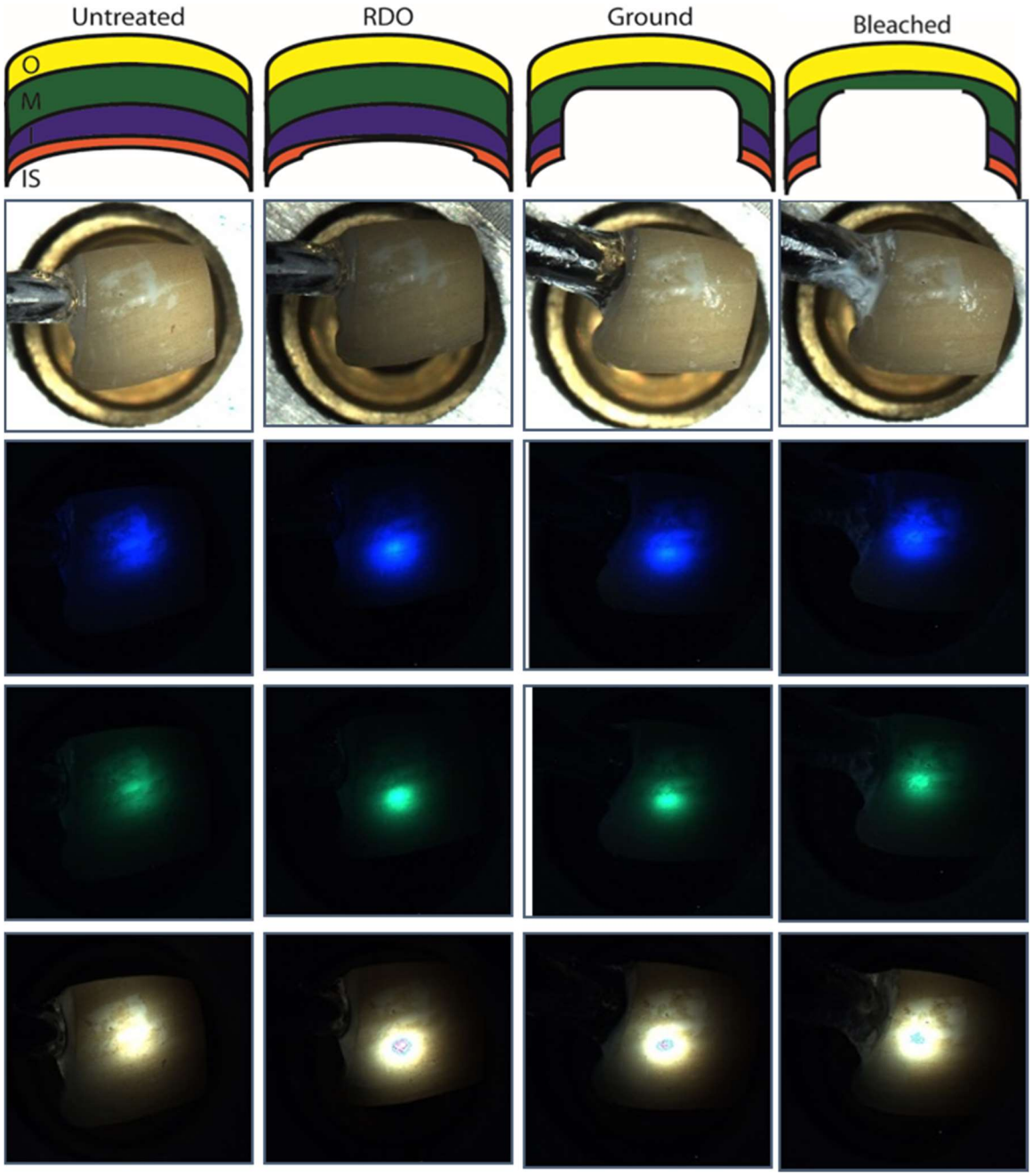

Figure 2-44. Diffusion of blue, green, and tungsten white light through a section of *H. brasiliana* shell. The interior surface was sequentially removed (progressing from Untreated, RDO, Ground, and then Bleached), and the resulting diffusion was observed.

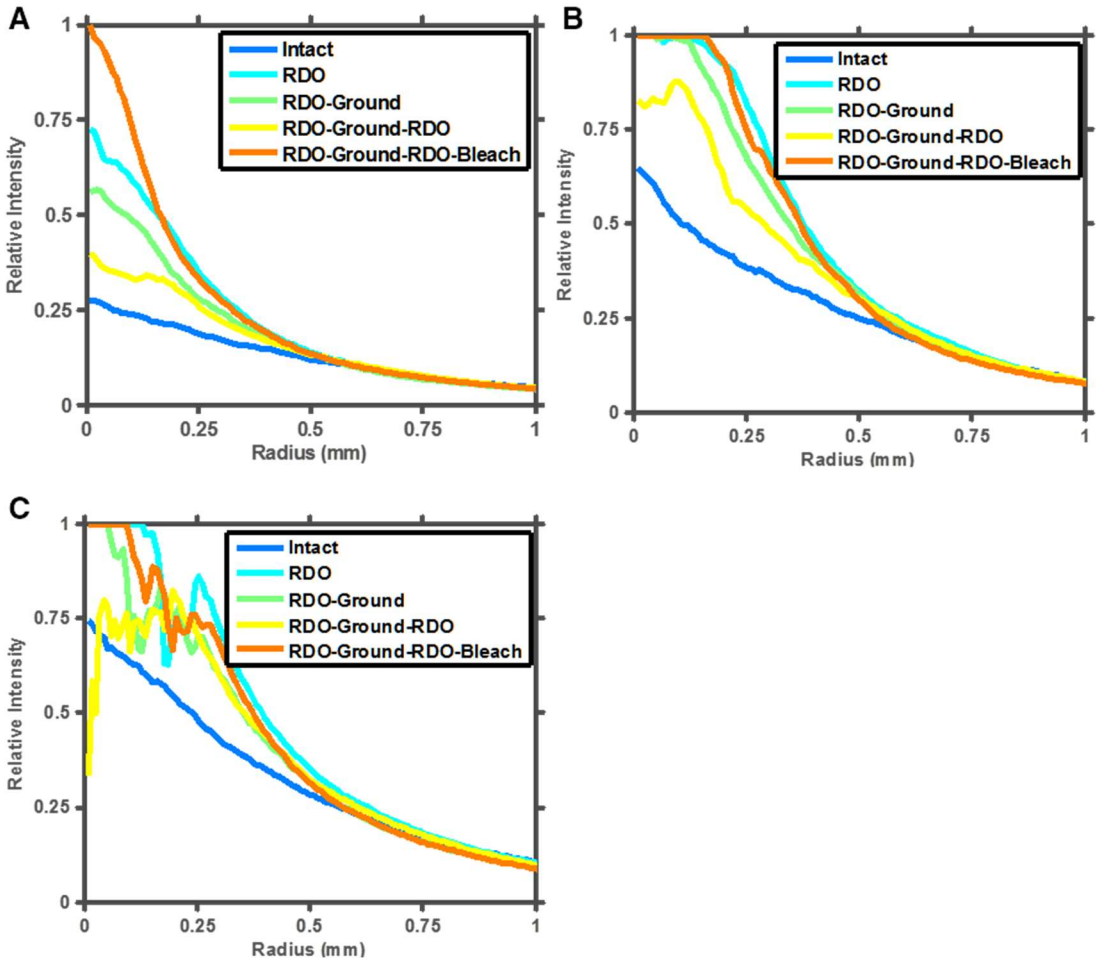

Figure 2-45 Intensity distribution for diffused light for the different shell treatments and different light sources. Green (A), Blue (B), and Tungsten White (C)

2.4.1. Diffusion of Light in Other Crossed Lamellar Shells

In contrast to the crossed lamellar structure, bioluminescence is a relatively recent adaptation in gastropods. For example there are only a few species of gastropods that have the ability to bioluminescence. When we examined species closely related to *H. brasiliana,* such as the non-luminescent *Planaxis sulcatus* that has a shell with a similar microstructure, we observed that the shells are not able

to diffuse or transmit light. However these shells are heavily pigmented with dark coloration that acts to absorb light being propagated through the shell.

In the shells of other non-luminescing lightly pigmented species, which are more distantly related to *Hinea brasiliana* than *P. sulcatus*, such as the shell of the queen conch (*Strombus gigas*) or the casket nassa (*Nassarius arcularius*), which both *possess* a similar crossed lamellar shell microstructure and are capable to transmit and diffuse light through remarkably thick (>2cm) sections of shell (Figure 2-46). The crossed lamellar structure found in the shells of the gastropods, *S. gigas, N. arcularius, and H. brasiliana*, vary significantly in the thickness and definition of the 2nd order lamellae. For example, in *H. brasiliana* and *N. arcularius* the 2nd order lamellae are significantly thinner than those commonly observed in *S. gigas*.

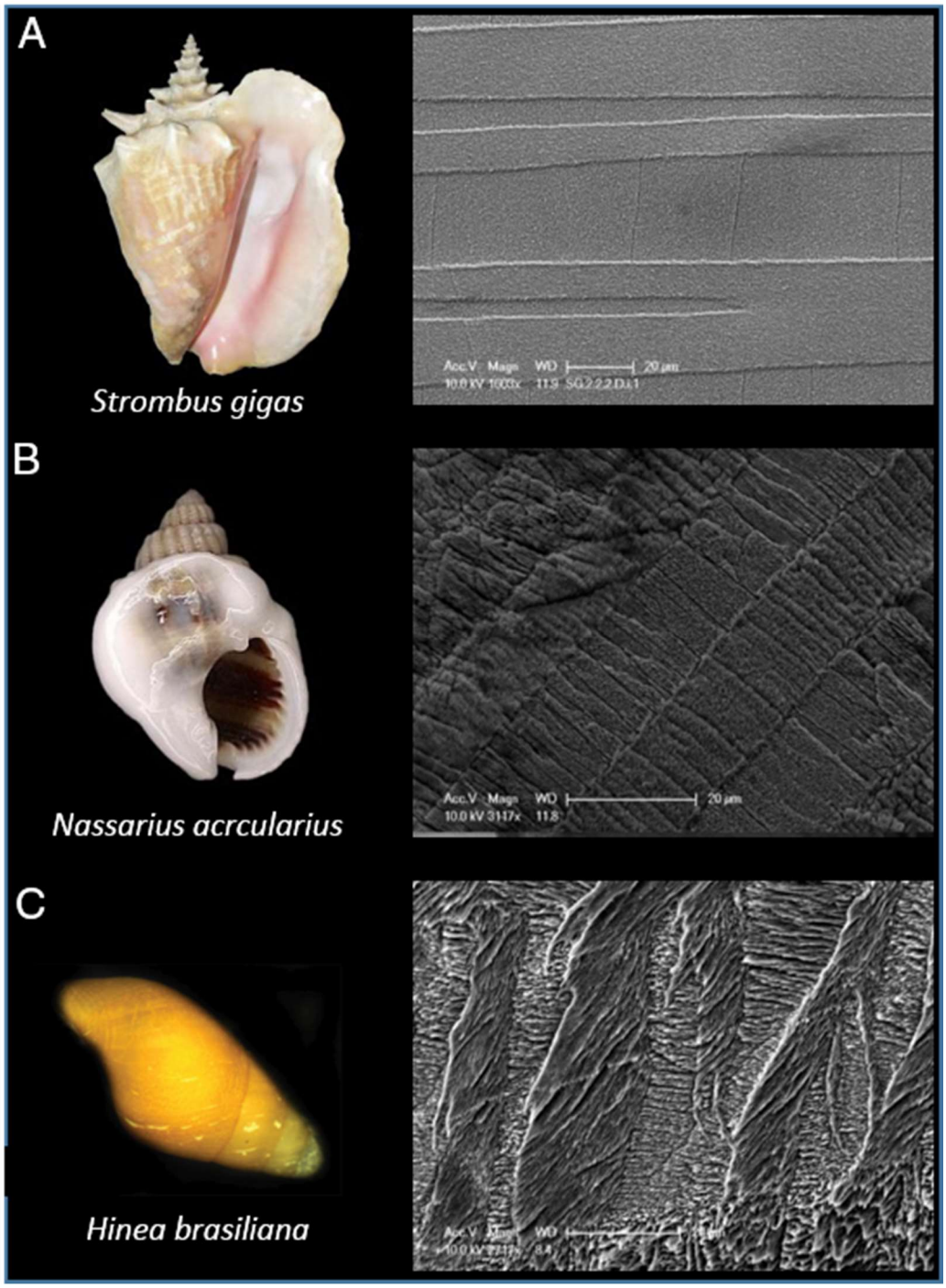

Figure 2-46. Size and regularity of 2nd order crossed lamellar features of select common gastropods. The queen conch (*Strombus gigas*) has large,10-30 μ m, well defined 2nd order lamellae (A). The 2nd order lamellae of the casket nassa (*Nassarius arcularius*) are also well defined but significantly thinner, approximately 1-5 µm (B). The 2nd order lamellae observed in *Hinea brasiliana* are very fine and not well defined (C).

Light that is transmitted through the 1st whorl of the *N. arcularius* shell does not diffuse significantly and retains the size and shape of the incident light (Figure 2-47 A). However, light that is transmitted through the thickened lip of the same shell is diffused along the margin of the shell. In this lip region, the middle crossed lamellar layer is significantly thicker than it is in the 1st whorl. The thickness and orientation of the crossed lamellar layers within the shell are influencing the diffusion of light, indicating that the mechanism of optical diffusion in crossed lamellar microstructure is geometric in nature. This means that optical diffusion of light in *Hinea* cannot be attributed to *Hinea* specific organic structures.

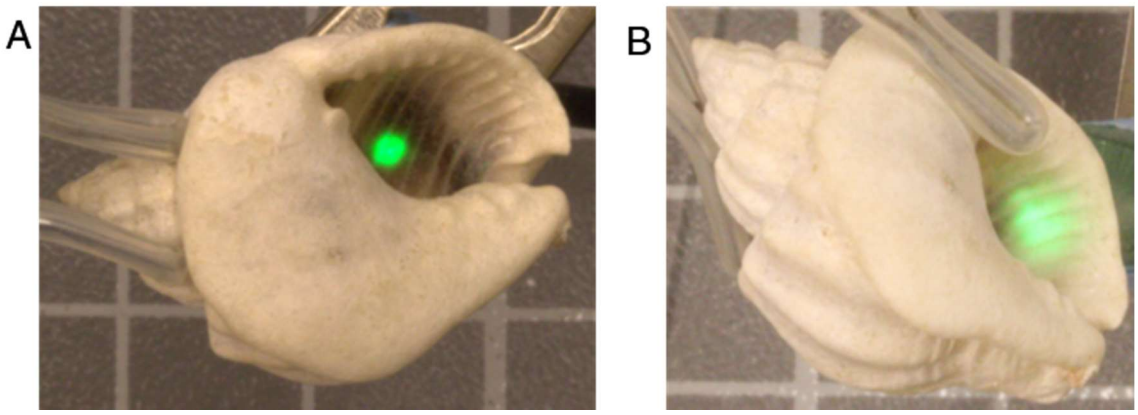

Figure 2-47. Diffusion of light through the shell of the casket nassa (*Nassarius arcularius*). Light is readily transmitted through the thickness of the shell in the 1st whorl, showing minimal diffusion (A). In the lip region light is diffused in the marginal direction, and covers a significantly larger spatial area.

The crossed lamellar microstructure is found in a number of other mollusks classes, including Bivalvia and Polyplacophora (*7*). The crossed lamellar structure is believed to have originated independently in the different classes. There is significant variation of the morphology and crystallography of the reported crossed lamellar structures, both within and between classes of mollusks. The crossed

lamellar structure found in bivalve shells, varies in its orientation and is found with the 1st order lamellae parallel to the growth direction (Figure 2-48). The crossed lamellar of bivalve shells is capable of diffusing light (Figure 2-49 A). Along the growing edge of the shell, there are numerous dark broad growth bands (Figure 2-48 C) and the diffusion of light within these dark growth bands is significantly higher than the surrounding white regions (Figure 2-49 B).

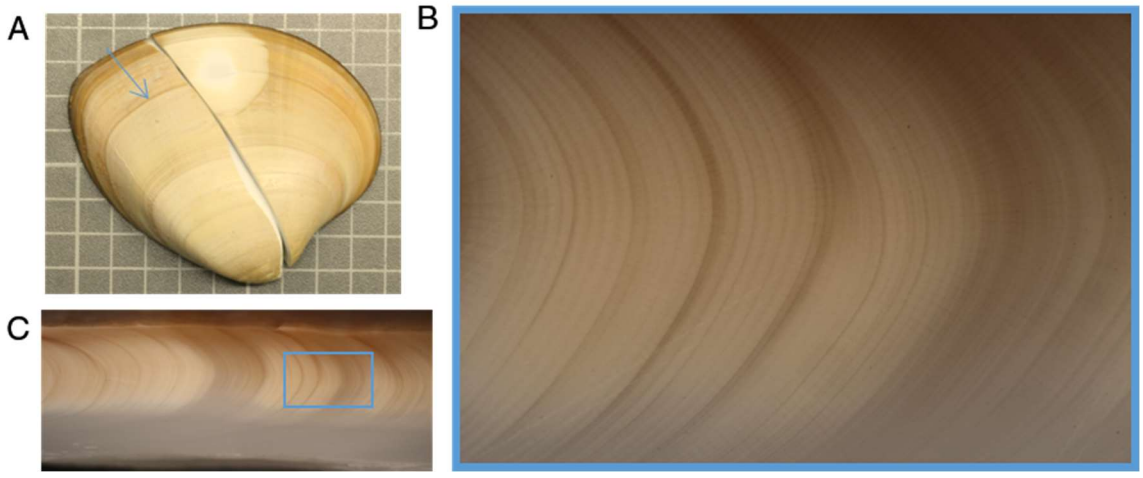

Figure 2-48. Overview of a bivalve shell (A). Distinctive light and dark 1st order lamellae are observed orthogonal to the growth lines in the lip of the shell (B). Broad growth regions have darker appearance (C).

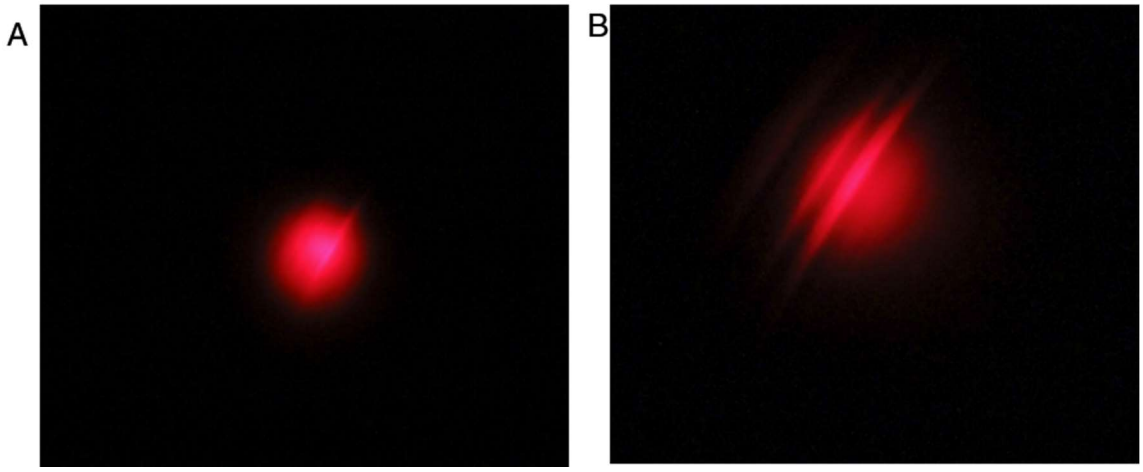

Figure 2-49 Diffusion of light through a bivalve shell (A). Diffusion was significantly enhanced in the region of the dark broad growth lines.

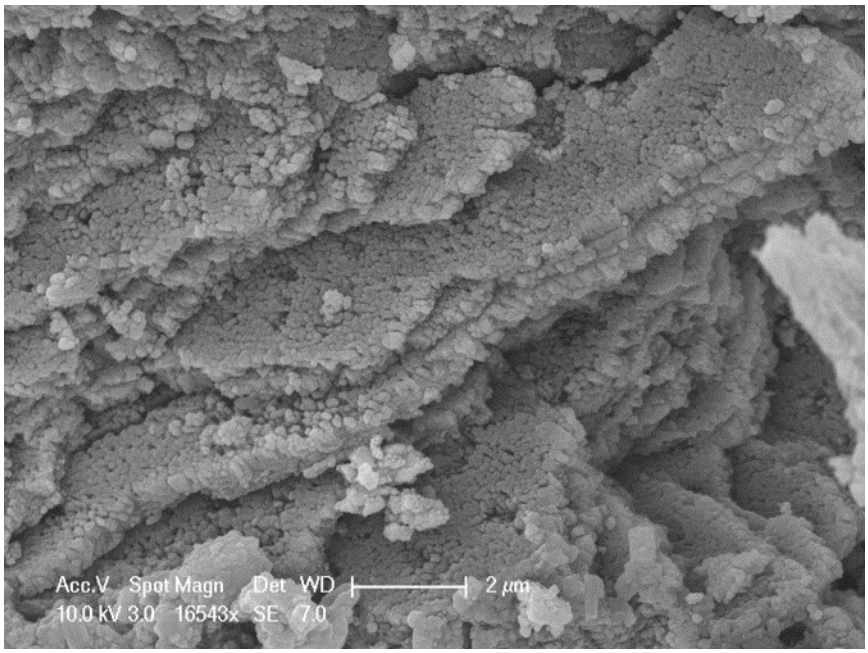

Figure 2-50. Scanning electron micrograph of the crossed lamellar structure from select bivalves. The 2nd order lamellae are composed of shorts rods aligned orthogonal to the long axis of the 2nd order.

The ability of the crossed lamellar structure to diffuse light is common to many of the varieties found in nature. The origin of bioluminescence within *H. brasiliana* and other planixids is most likely to be influenced by the numerous advantages of

the crossed lamellar microstructure, later utilizing the intrinsic properties to diffuse bioluminescent light through its shell.

2.4.2. **Diffusion of light in a single Crossed Lamellar Layer**

To better understand the diffusion of light through a crossed lamellar microstructure, we tested the inner layer of *Strombus gigas* with the 2nd order lamellae aligned ±45° from the surface normal. The transmitted light through the shell is asymmetrically diffused and is elongated along the directions of the 1st order lamellae (Figure 2-51 A-D). Upon closer examination of the diffuse transmitted spot, the 1st order lamellae surrounding the intense central are illuminated and alternate in their dark and light appearance depending on their position relative to the light source (Figure 2-52). Within a single crossed lamellar

layer the transmittance of light is higher in directions normal to the 0th order direction, parallel with the 1st order sheets.

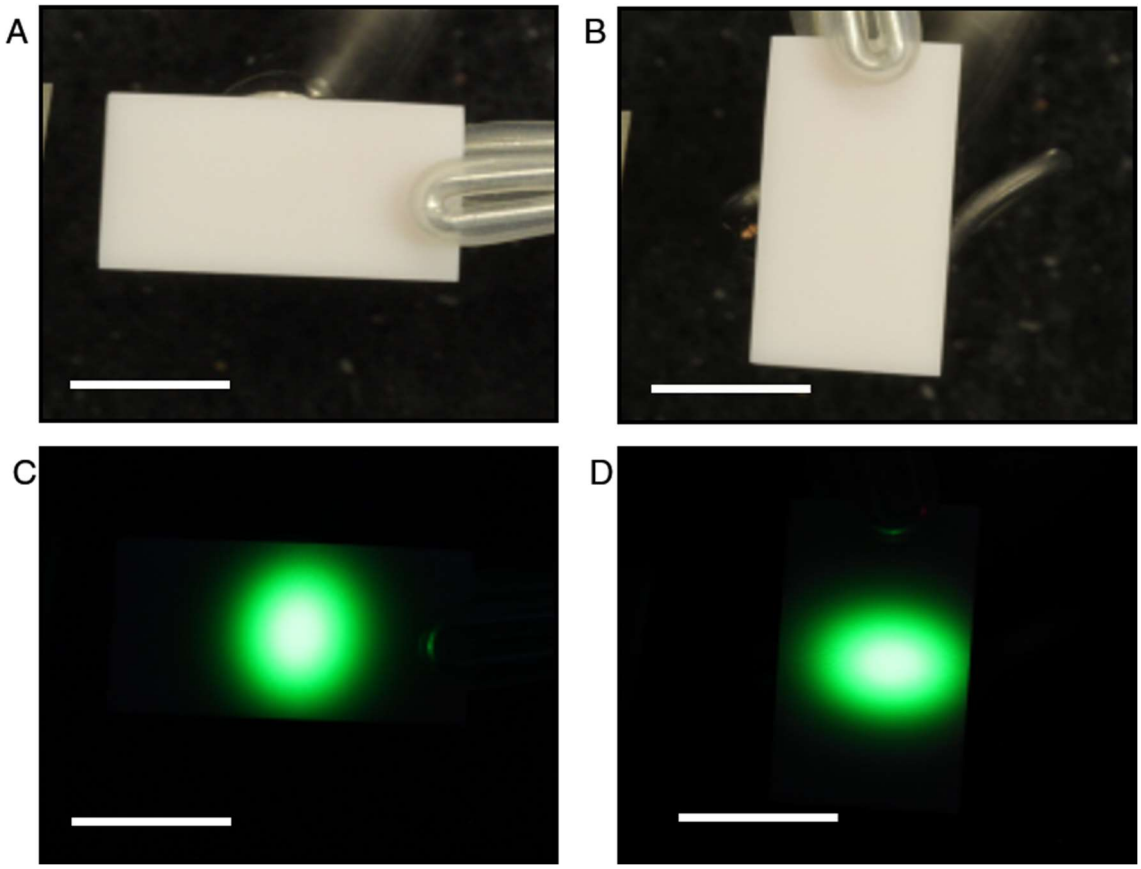

Figure 2-51. Rectangular slab of a single inner crossed lamellar layer from *Strombus gigas*, in a 0°(A) and 90°(B) orientation. Diffusion of light through the single crossed lamellar layer for 0°(C) and 90°(D) orientation.

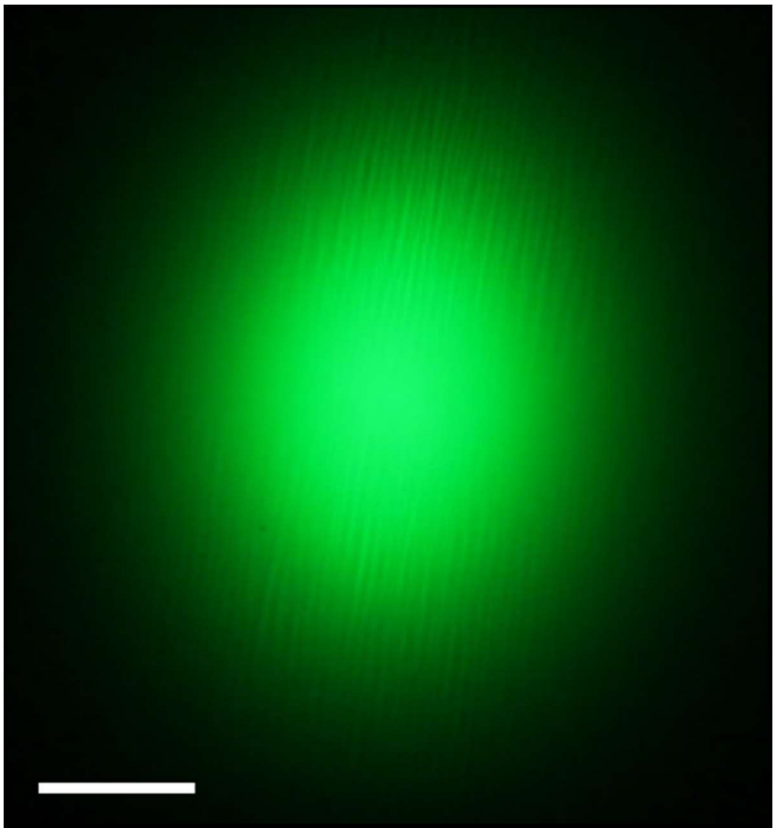

Figure 2-52. Asymmetric diffusion of light through the *Strombus gigas* shell. The diffusion is elongated along the planes of the 1st order lamellae. Around the intense centrally transmitted spot, characteristic light and dark 1st order lamellae can be observed.

2.4.3. **Diffusion of Light along 1st order Lamellae**

Within the shell light is preferentially transmitted along the length of 2nd order lamellae and appears to be absorbed in directions perpendicular to the length. In the ±45° orientation the asymmetry is due to light escaping from the ends of the 2nd order lamellae, while the lateral spread of light is limited. In the direction along the length of the 2nd order lamellae there are significantly fewer mineral/organic interfaces than compared to the other principle directions along the 2nd order plank. Within one 1st order lamella there is approximately one mineral-organic interface per 5 μm of 3rd order length. There are approximately 50 interfaces per 5 μm along

the direction of the thickness of the 3rd order, and 33 interfaces along the width. The role of the 1st order lamellae can be observed from the asymmetric diffusion of light through a single 0th order layer of the crossed lamellar microstructure. When examined closely the 1st order lamellae are illuminated based on their orientation and spatial relation to the light source, which results in an alternating light and dark 1st order lamellae.

2.4.4. Diffusion of Light Among 3rd order Lamellae

The 3rd order lamellae are composed of many well-ordered 4th order particles that are crystallographically and optically coherent within the 3rd and 2nd order lamellae. In addition the (110) plane is approximately parallel with the plane of its 1st order lamellae. The c-axis is tilted approximately 26° from the long axis of the 3rd order lamellae, resulting in high mineral coherency along the length of the 3rd order planks within a 1st order lamellae. The angle of the c-axis varies by 26° between alternating 1st order lamellae, while they share a mutual aligned (110) twin plane which is approximately parallel with the 1st order interfaces. The aragonitic structure within the 3rd order lamellae of crossed lamellar gastropod has significant higher frequency twining along the (110) plane when compared to other mollusk and geologic aragonite (*23, 25*). Scattering of light traveling along a 3rd order is reduced due to the high degree crystallographic alignment of the mineral grains (4th order) and the mineral/organic inter-4th order material (Figure 2-53). Due to the biaxial nature of the aragonite mineral the transmittance and reflection of light at the aragonite and organic interface is dependent on the orientation of the mineral.

The difference in index of refraction between aragonite, refractive indices of α=1.530 β=1.681 γ=1.686 (*26*), and alpha-chitin, refractive index of 1.550 – 1.557 (*27*), is minimal in the c-direction and greatest in the a- and b-directions of the mineral. The difference in the index of refraction between the organic and the mineral results in the attenuation of light traveling across 1st order lamellae ([110] direction).

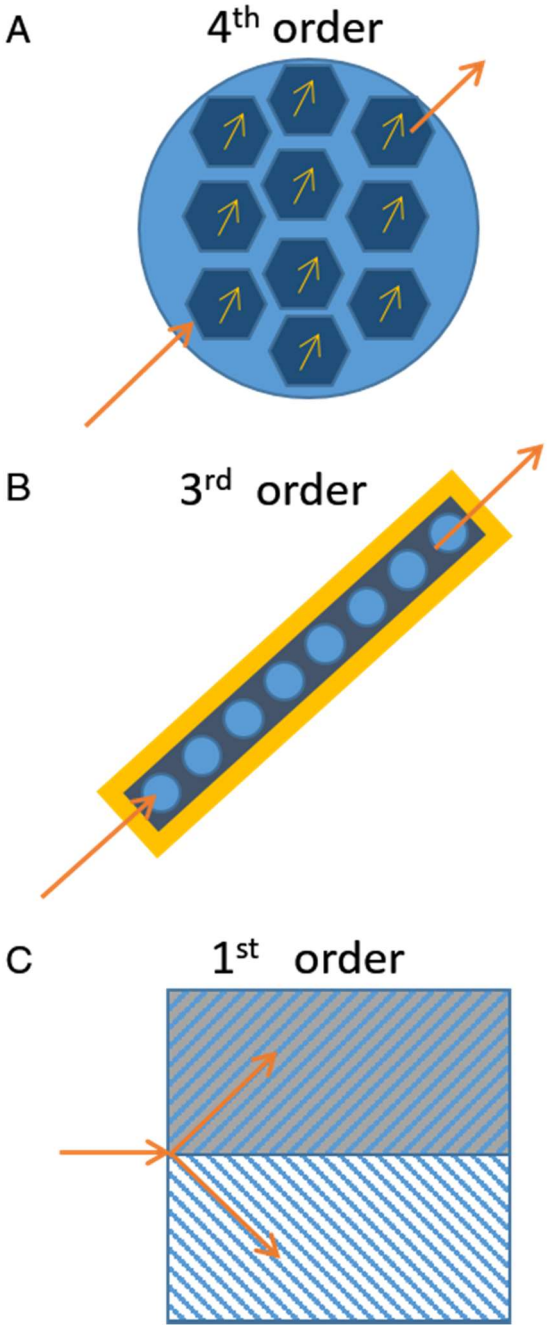

Figure 2-53. Optical interfaces within higher order lamellae. 4th order lamellae are composed crystallites that form a pseudo single crystal (A). 3rd order lamellae consist of many well-aligned 4th order lamellar, and are encased in an envelope of organic material (B). 1st order lamellae are composed of long continuous sheets of well aligned fibers (C).

2.4.5. **Heat Treatment of SG**

To further understand the role of the organic and crystalline phases within the crossed lamellar structure, samples from the inner crossed lamellar layer of *S. gigas* were annealed in air for a series of isothermal heat treatments with temperatures ranging from 150°C to 400°C. Drastic changes in both the optical and structural properties of the shell were observed. Isothermal annealing was used to account for the kinetics of degradation in dense intact crossed lamellar (Figure 2-54). At 150°C, 1.2% of the mass was lost corresponding with a loss of organic materialbetween 4th order features and intra-4th order organic material?? (*28*). However, the optical diffusivity and crystallographic properties are preserved (Figure 2-57 B). After treatment at 200°C there is a minor increase in the total mass loss (Total 1.4% Figure 2-55) and the mineral phase remains as aragonite, in addition 4th order lamellae are beginning to coarsen resulting in voids forming within the 3rd order lamellae (Figure 2-58 C), the transmitted light through the section is heavily attenuated but is still detectable. Previous rapid annealing photothermal studies have shown that the majority of the mass loss between 150°C and 200°C can be attributed to decomposition of the organic resulting in an increase in thermal conductivity by decreasing the resistance at interfaces, this is followed by transformation from aragonite to calcite phase between 300-500°C, and a final transformation to calcium oxide above 700°C (*29*). At 300°C, 3rd order lamellae have significantly increased in sized and have a faceted appearance (Figure 2-58 D), the total mass loss increases slightly to 1.7% (Figure 2-55) is lost,

at this point the mineral phase is a mixture of both aragonite and calcite (Figure 2-56). At this stage in the heat treatment light transmitted through the crossed lamellar sample is completely attenuated, the section has a dark grey appearance with alternating light/dark grey 1st order lamellae. At 400°C the mineral phase has completely transformed to calcite and there is only a slight increase in mass loss (1.8%), the microstructure is almost completely transformed to dense globular spheroids (Figure 2-58 D). The evolution of the crossed lamellar microstructure during heat treatment is influenced by composition of the biological composite with the interaction of aragonite, amorphous calcium carbonate, polypeptides, and polysaccharides acting to modify the annealing characteristics compared to abiotic calcium carbonates.

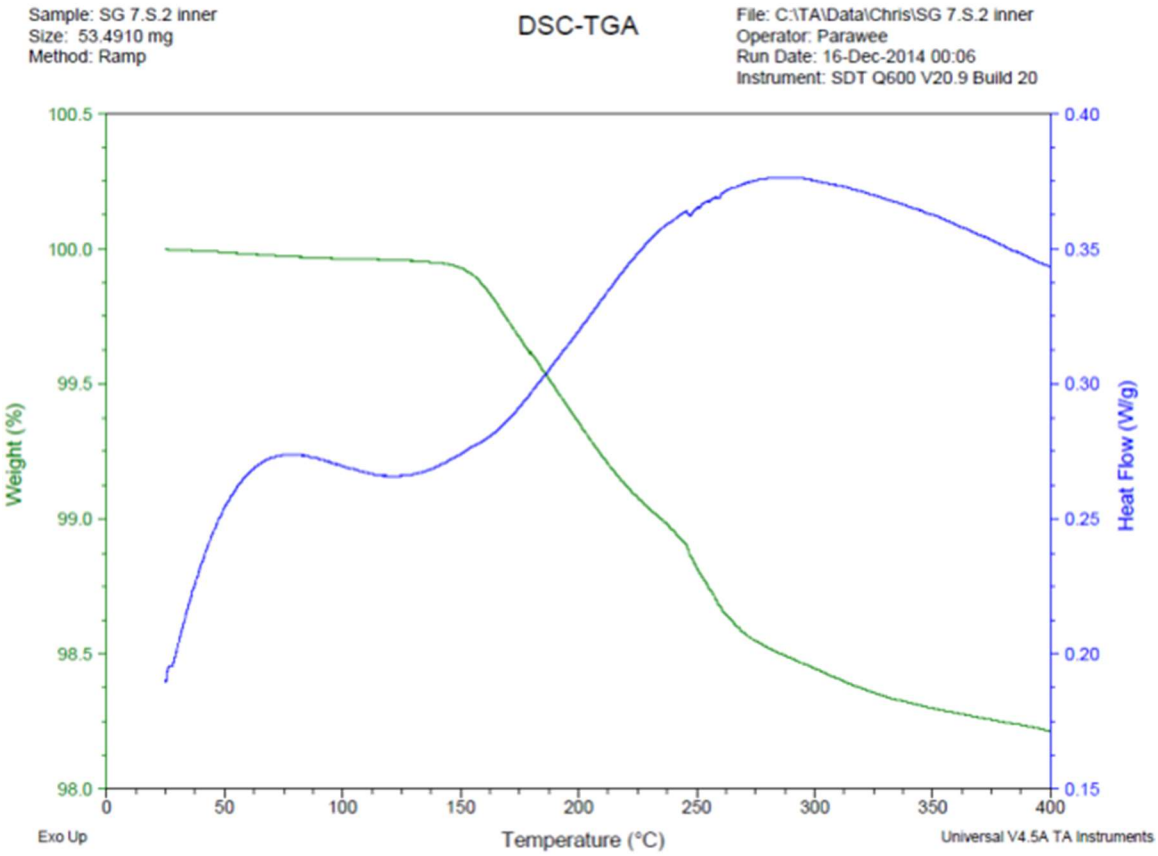

Figure 2-54. Mass loss from crossed lamellar powders from the shell of *Strombus gigas* during ramped heat treatment in air.

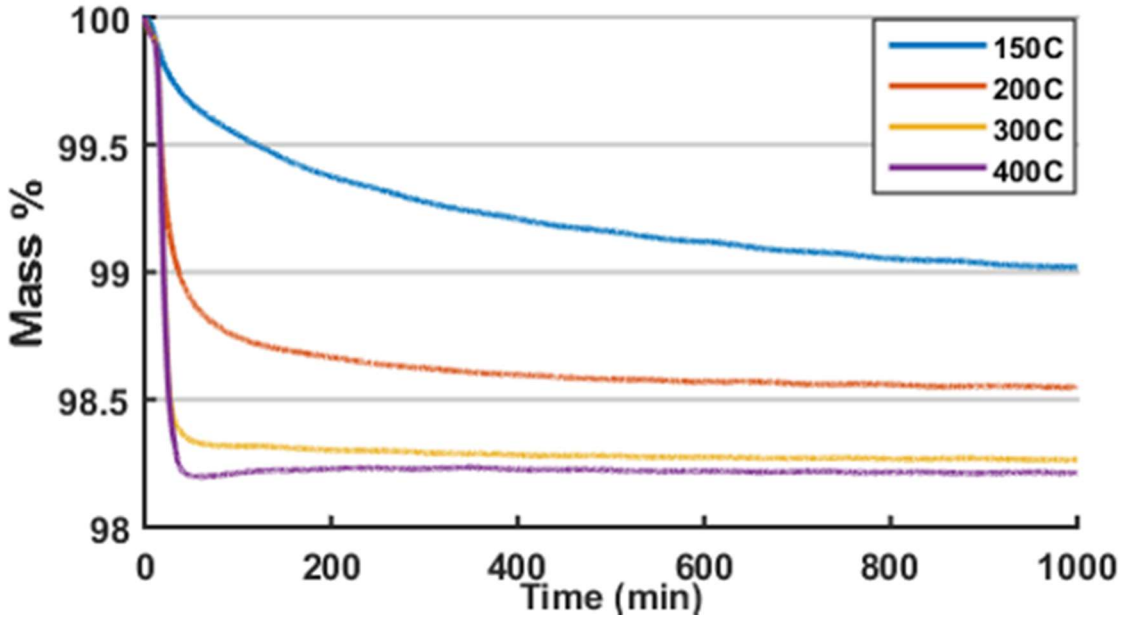

Figure 2-55. Mass loss during isothermal heat treatment in air of the inner crossed lamellar layer from *Strombus gigas*.

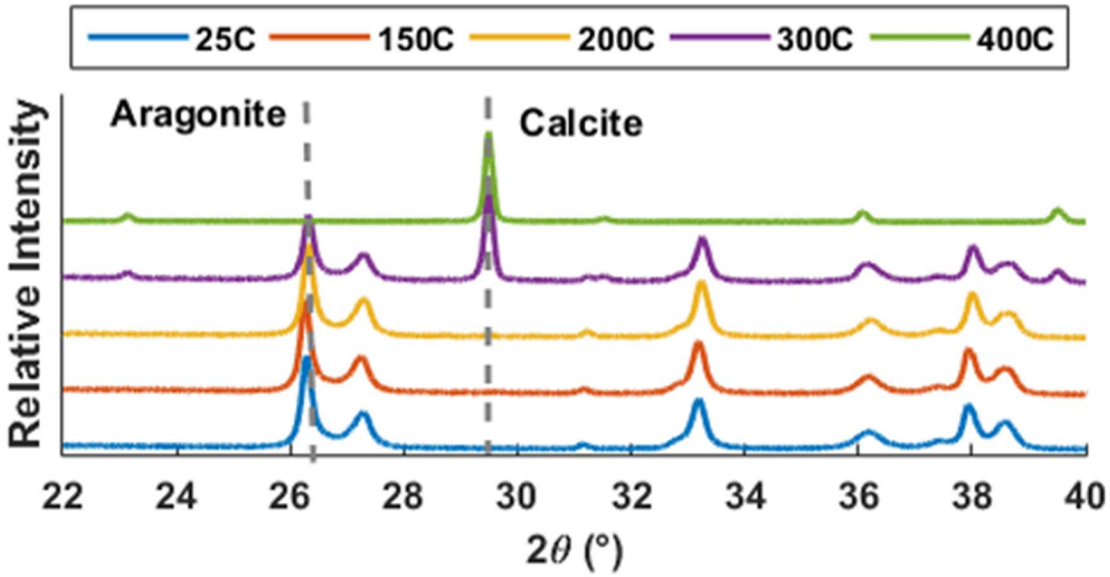

Figure 2-56. X-ray diffraction patterns from the inner crossed lamellar layer of *Strombus gigas* after isothermal heat treatments in air.

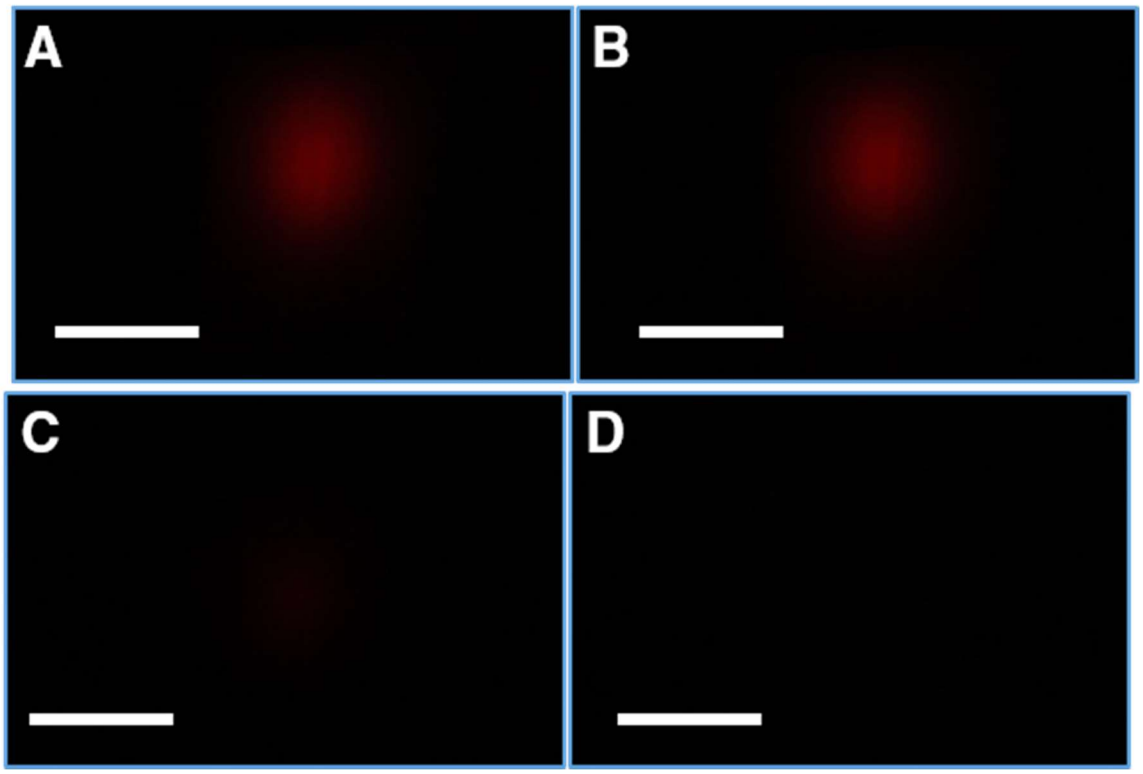

Figure 2-57. Diffusion of light through a rectangular slab of inner crossed lamellar from *Strombus gigas*. Untreated (A), 150°C (B), 200°C (C), 300°C (D).

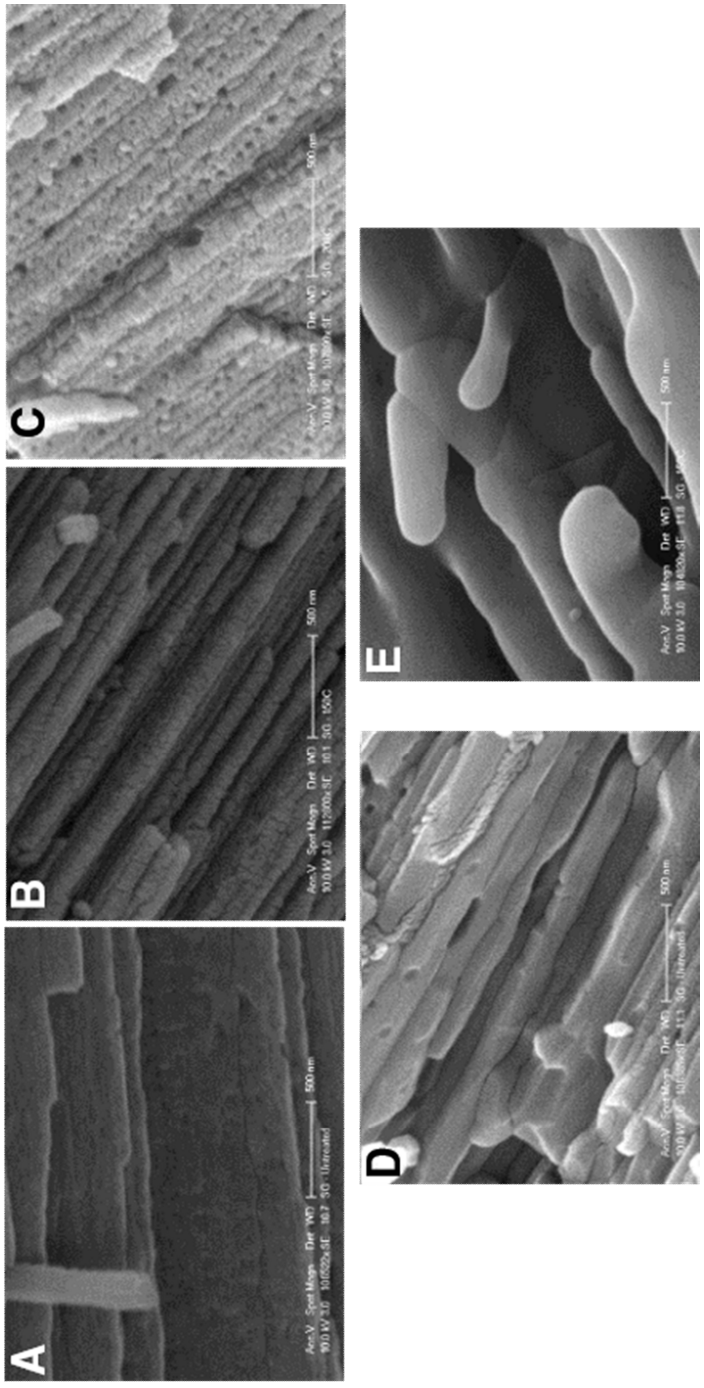

Figure 2-58. Scanning electron micrographs of the inner crossed lamellar layer from *Strombus gigas* after various stages of heat treatments. Untreated (A), 150°C (B), 200°C (C), 300°C (D), and 400°C (E).

2.4.6. **Model of Light Transmittance**

Individual crossed lamellar layers act to diffuse light along the direction of the 1st order sheets, resulting in the asymmetric diffusion of light observed in Figure 2-52. When multiple crossed lamellar layers are combined with perpendicular 0th order directions, light is diffused in two steps along the two perpendicular 1st order directions. The combination of two orthogonal asymmetric diffusers results in a uniform diffusion of light over a larger area (Figure 2-59). Between the different layers within the shell there does not appear to be abrupt or distinct transitions, and both the 1st and 3rd order features appear to continue across the boundary between layers, reducing the scattering by minimizing the number of interfaces along the optical path (Figure 2-23).

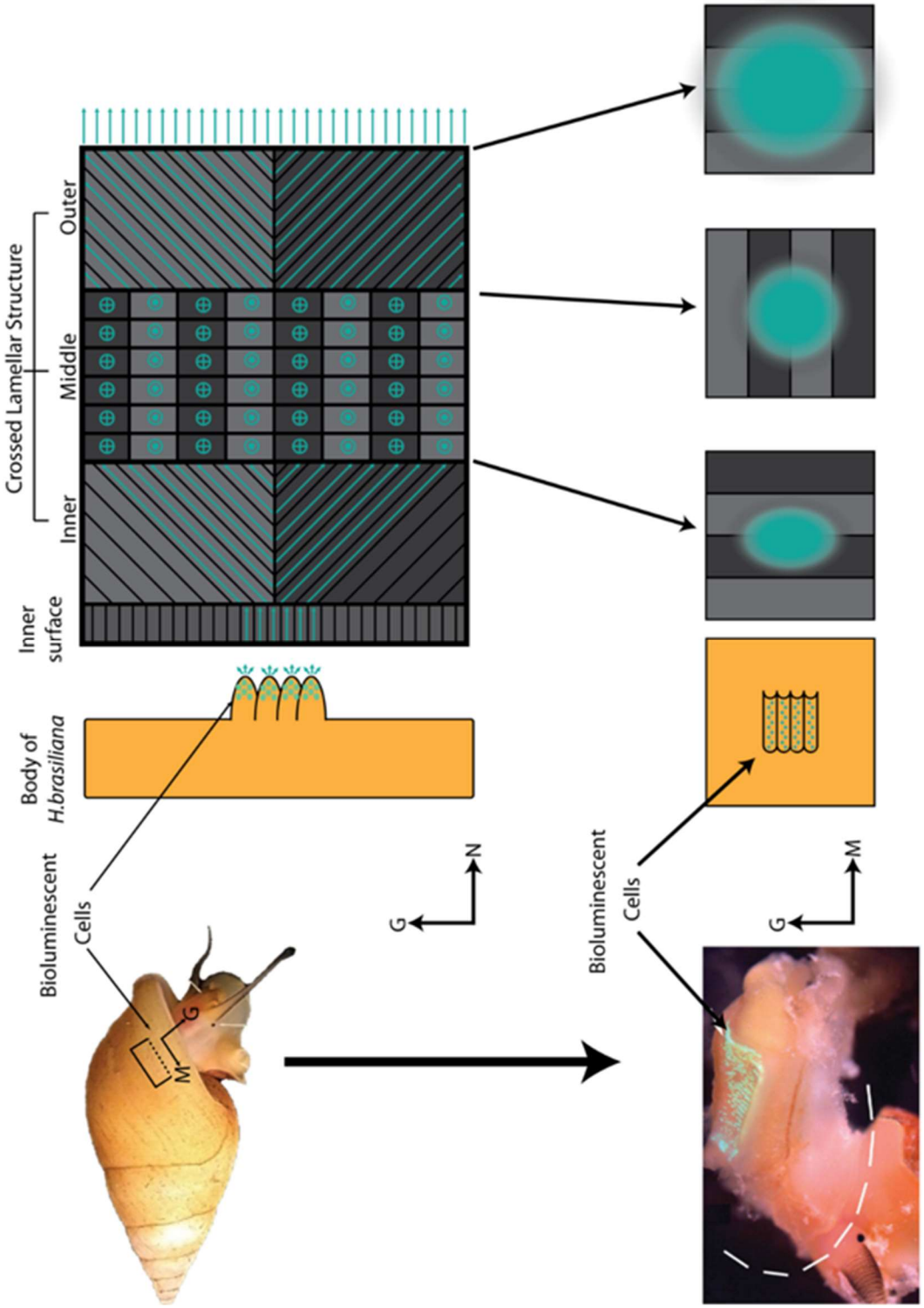

Figure 2-59. Model of the diffusion of bioluminescent light in the crossed lamellar shell of *Hinea brasiliana*.

2.5. Conclusions

Bioluminescent displays can be utilized for a variety of both defensive and offensive functions such as: active camouflage, prey attraction, intraspecific communication, predator distraction, and illumination. One additional defensive application, which may be used by *H. brasiliana*, is that of a “burglar alarm.” The idea of such a “burglar alarm” is that when there is threat from a predator, the potential prey uses its bioluminescent display to attract the attention of larger predators in an attempt to scare away the attacking predator.

The crossed lamellar shell microstructure has become the most common gastropod microstructure due to the evolutionary advantages it provides gastropods in a diverse range of ecological niches. In addition to the hard and tough nature of the crossed lamellar microstructure, many geometric defensive traits such as spines, broad lips, and narrow apertures have evolved in many species. *Hinea brasiliana* evolved bioluminescence that was further enhanced by the inherent diffusive nature of the crossed lamellar structure. Hierarchical arranged biologic structures may possess properties desirable for applications far outside of the scope of the original evolutionary adaptation.

2.6. Materials and Methods

2.6.1. Scanning Electron Microscopy (SEM)

Scanning election microscopy was performed using a Phillips XL-30 microscope operating at 10 keV. Samples were mounted to an aluminum stub with adhesive carbon tape and then sputter coated with Pt/Pd (Cressington 108 Watford,

England) to reduce charging. To enhance surface features fractured specimens were treated with 5% NaClO for 30seconds to partially remove the residual organic film.

2.6.2. 1-D X-Ray Diffraction (XRD)

Theta-Theta x-ray diffraction spectra were recorded using a PANalytical Empyrean (PANalytical Westborough, MA), using x-rays generated from Cu $K\alpha_1$. Solid samples were rotated at a frequency of 4 s^{-1}. Intensity data was recorded from 10-70° 2θ.

2.6.3. Thermal Gravimetric Analysis (TGA)

Crossed lamellar powders and sections were analyzed using a TA Instruments SDT Q600 TGA/DSC (TA Instruments New Castle, DE). Samples were heated from room temperature to the annealing temperature at a rate of 5° C per minute. Heat flow and mass loss were recorded during a 1000 minute isothermal hold. Air at 10 ml/min was flowed over the sample.

2.6.4. Synchrotron 2-D X-Ray Diffraction (2D-XRD)

Synchrotron x-ray diffraction experiments were conducted on beam line X-6B at the National Synchrotron Light Source at Brookhaven National Laboratories. The beam energy was 19.0 KeV with a spot size of 100μm. Two dimensional diffraction patterns were recorded by a CCD area detector. Samples were mounted to a motorized stage that allowed for translation of the sample along two axes.

Cross-sections of *Hinea brasiliana* shell were prepared by grinding with silicon carbide paper until approximately 600μm thick, and then polished with progressively finer diamond suspensions until 1μm.

Diffraction patterns were analyzed using Data Squeeze software package to calculate the intensity as a function of q. Peak intensities were determined by use of the fit function in MATLAB to find Gaussian curves for key peaks within the intensity versus q plots.

2.6.5. **Nanoindentation**

Nanoindentation was performed using a TI-950 nanoindenter (Hysistron MN, USA) equipped with a Berkovich diamond indenter probe. Displacement controlled indents were performed to a depth a 500nm in a map 20 by 5 with 20μm spacing between indents, using a 5s load, 5s hold, 5s unload quasi static indentation profile. Depth and load data was recorded for each event. The elastic modulus and indentation hardness are calculated using the procedure outlined by Oliver and Pharr (*30*).

Samples for nanoindentation were embedded in an epoxy resin, and then sectioned with a water cooled diamond saw. Sections were then polished with progressively finer diamond suspensions ranging from 15μm to 50nm.

2.6.6. **Optical Characterization**

The optical characterization of *Hinea brasiliana* shell was performed using Nikon SMZ 1500 stereomicroscope equipped with a CCD camera for recording images. Light is produced by LED drivers (Ocean Optics, Dunedin, FL USA)

coupled with a 50µm fiber optic cable.The optical characterization of the *Strombus gigas* was performed using a Canon 60-d DSLR camera (Canon Inc., USA) while the samples were illuminated by a 1mm PMMA fiber optic cable coupled with LED drivers.

Treatment of *Hinea* shell for optical testing. The 1st whorl was removed from a large specimen and the unmodified shell section was used for the intact sample. Then the inner surface was briefly wiped with RDO-rapid decalcifier (Sigma Chemical Co., St. Louis, MO) (RDO treatment). 150 µm of the inner surface was ground away using a cylindrical diamond grinding tool (RDO-Ground). The ground surface was subsequently treated with RDO (RDO-Ground-RDO), and then finally treated with Sodium hypochlorite (RDO-Ground-RDO-Bleach).

The crossed lamellar layers of *Strombus gigas* shell were sectioned using a rotary tool equipped with a diamond cut-off blade. Sections were then ground into slabs of crossed lamellar using Silicon carbide paper. The faces of the crossed lamellar slab were then polished with progressively finer diamond suspensions ranging from 15µm to 50nm.

References

1. S. H. D. Haddock, M. A. Moline, J. F. Case, Bioluminescence in the Sea. *Annu Rev Mar Sci* **2**, 443-493 (2010).

2. M. J. Vendrasco, S. M. Porter, A. V. Kouchinsky, L. Guoxiang, C. Fernand, Shell microstructures in early mollusks. *Festivus* **42**, 43-53 (2010).

3. B. Pokroy, E. Zolotoyabko, Microstructure of natural plywood-like ceramics: a study by high-resolution electron microscopy and energy-variable X-ray diffraction. *J Mater Chem* **13**, 682-688 (2003).

4. G. J. Vermeij, The Mesozoic marine revolution: evidence from snails, predators and grazers. *Paleobiology*, 245-258 (1977).

5. A. R. Palmer, Relative Cost of Producing Skeletal Organic Matrix Versus Calcification - Evidence from Marine Gastropods. *Mar Biol* **75**, 287-292 (1983).

6. J. Sälgeback, Functional morphology of gastropods and bivalves. (2006).

7. D. Chateigner, C. Hedegaard, H. R. Wenk, Mollusc shell microstructures and crystallographic textures. *J Struct Geol* **22**, 1723-1735 (2000).

8. E. A. Widder, Bioluminescence in the Ocean: Origins of Biological, Chemical, and Ecological Diversity. *Science* **328**, 704-708 (2010).

9. J. M. Claes, M. N. Dean, D. E. Nilsson, N. S. Hart, J. Mallefet, A deepwater fish with 'lightsabers'--dorsal spine-associated luminescence in a counterilluminating lanternshark. *Sci Rep* **3**, 1308 (2013).

10. M. Isobe, D. Uyakul, T. Goto, J. J. Counsilman, Dyakia bioluminescence—1. Bioluminescence and fluorescence spectra of the land snail, D. striata. *J Biolum Chemilum* **2**, 73-79 (1988).

11. V. B. Meyer-Rochow, S. Moore, Biology of Latia neritoides Gray 1850 (Gastropoda, Pulmonata, Basommatophora): the Only Light-producing Freshwater Snail in the World. *Internationale Revue der gesamten Hydrobiologie und Hydrographie* **73**, 21-42 (1988).

12. E. N. Harvey, *Bioluminescence*. (Academic Press, 1952).

13. Y. Haneda, Studies on luminescence in marine snails. (1958).

14. R. S. Houbrick, *Anatomy, Reproductive Biology, and Phylogeny of the Planaxidae (Cerithiacea-Prosobranchia)*. (Smithsonian Institution Press, 1987).

15. D. D. Deheyn, N. G. Wilson, Bioluminescent signals spatially amplified by wavelength-specific diffusion through the shell of a marine snail. *P Roy Soc B-Biol Sci* **278**, 2112-2121 (2011).

16. Y. Dauphin, A. Denis, Structure and composition of the aragonitic crossed lamellar layers in six species of Bivalvia and Gastropoda. *Comp Biochem Phys A* **126**, 367-377 (2000).

17. X. W. Su, D. M. Zhang, A. H. Heuer, Tissue regeneration in the shell of the giant queen conch, Strombus gigas. *Chem Mater* **16**, 581-593 (2004).

18. L. Romana *et al.*, Use of nanoindentation technique for a better understanding of the fracture toughness of Strombus gigas conch shell. *Materials Characterization* **76**, 55-68 (2013).

19. W. L. Bragg, The analysis of crystals by the X-ray spectrometer. *Proceedings of the Royal Society of London. Series A, Containing Papers of a Mathematical and Physical Character*, 468-489 (1914).

20. P. Ewald, Introduction to the dynamical theory of X-ray diffraction. *Acta Crystallographica Section A: Crystal Physics, Diffraction, Theoretical and General Crystallography* **25**, 103-108 (1969).

21. J. G. Carter, *Skeletal biomineralization: patterns, processes and evolutionary trends*. (Wiley Online Library, 1990), vol. 1.

22. A. Patterson, The Scherrer formula for X-ray particle size determination. *Physical review* **56**, 978 (1939).

23. T. Kogure *et al.*, Twin density of aragonite in molluscan shells characterized using X-ray diffraction and transmission electron microscopy. *Journal of Crystal Growth* **397**, 39-46 (2014).

24. A. B. Rodriguez-Navarro, A. Checa, M. G. Willinger, R. Bolmaro, J. Bonarski, Crystallographic relationships in the crossed lamellar microstructure of the shell of the gastropod Conus marmoreus. *Acta biomaterialia* **8**, 830-835 (2012).

25. M. Suzuki, H. Kim, H. Mukai, H. Nagasawa, T. Kogure, Quantitative XRD analysis of {110} twin density in biotic aragonites. *Journal of structural biology* **180**, 458-468 (2012).

26. W. Bragg, The refractive indices of calcite and aragonite. *Proceedings of the Royal Society of London. Series A, Containing Papers of a Mathematical and Physical Character*, 370-386 (1924).

27. I. B. J. Sollas, On the Identification of Chitin by Its Physical Constants. *Proceedings of the Royal Society of London. Series B, Containing Papers of a Biological Character* **79**, 474-481 (1907).

28. B. Pokroy, J. P. Quintana, E. N. Caspi, A. Berner, E. Zolotoyabko, Anisotropic lattice distortions in biogenic aragonite. *Nat Mater* **3**, 900-902 (2004).

29. A. Hernandez-Ayala, P. Quintana, J. Alvarado-Gil, D. Aldana, Photothermal characterization of thermally treated shells of Strombus Gigas. *J Phys Iv* **125**, 691-695 (2005).

30. W. C. Oliver, G. M. Pharr, An Improved Technique for Determining Hardness and Elastic-Modulus Using Load and Displacement Sensing Indentation Experiments. *J Mater Res* **7**, 1564-1583 (1992).

3. Fracture Properties of Crossed Lamellar Gastropod Shells Utilizing Nanoindentation

Abstract

Gastropods have evolved shells that can resist the threat of increasingly stronger predators that smash, peel, and crush their shells. Gastropods shells are most commonly constructed from a crossed lamellar microstructure, which is a hierarchically arranged architecture that is carefully formed from structures that range from the nanometer to the millimeter scale. The careful control of the entire crossed lamellar structure is responsible for the four orders of magnitude increase in fracture toughness versus abiotic aragonite mineral. We observed, examined, and modeled the effect of differing orientations of the microstructural influence the inter-third order lamellar fracture behavior by nanoindentation of well aligned sections from the inner layer of the *Strombus gigas* shell. We observed significant influences of the plank structure orientation and the nanoindenter probe on the measured indentation properties. The ±45° arrangement of planks found within natural examples of crossed lamellar provides a significantly more isotropic resistance to penetration by sharp objects such as jaws and claws. In addition, the ±45° arrangement is able to resist higher loads before failure.

3.1. Introduction

Gastropods have evolved tough and hard shells in order to provide protection from durophagous (shell breaking) predators. Their shells are made from a composite material, primarily composed of the aragonite phase of calcium

carbonate combined with a small fraction of structural (i.e., polysaccharide) and functional (i.e., protein) organic material (~1%). Through the use of this organic fraction, which controls the growth and arrangement of the mineral components, gastropods have evolved numerous shell microstructures that greatly enhance the toughness of the structure when compared to geologic aragonite. Over the course of 400 million years of evolution, two common microstructures have arisen within the shells gastropods. The first being the evolutionary older nacre and the second is the crossed lamellar, which emerged as the dominant gastropod shell microstructure after the Mesozoic marine revolution (*1*). An extant example of the crossed lamellar structure is found in the thick and heavily mineralized shell of the *Strombus gigas* (queen conch), a large (>30 cm) Atlantic gastropod (Figure 3-1).

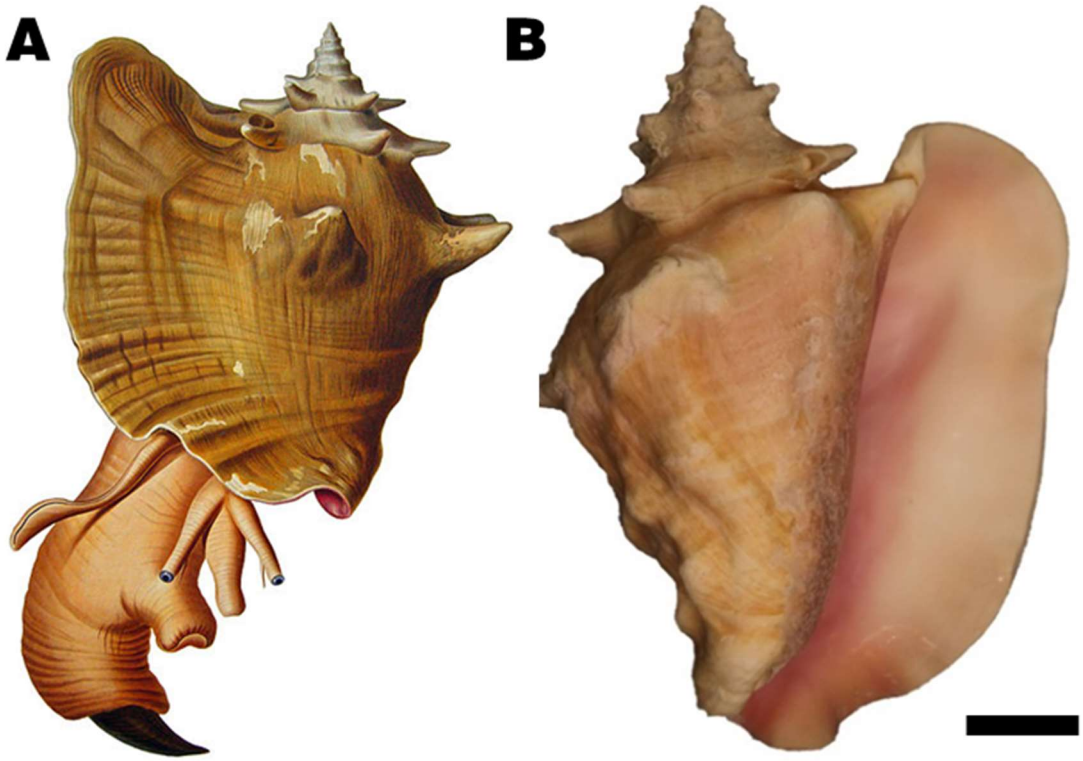

Figure 3-1 Illustration of *Strombus gigas* (queen conch) with shell (Chenu, 1844) (A). Dried and cleaned shell of an adult specimen (B).

3.2. Ultrastructure of *Strombus gigas* Shell

The shell of *Strombus gigas* is composed of three distinct crossed lamellar layers, the inner, middle, and outer, which are each composed of four different hierarchal orders of features with a hierarchy from the nanometer to millimeter scale (Figure 3-2).

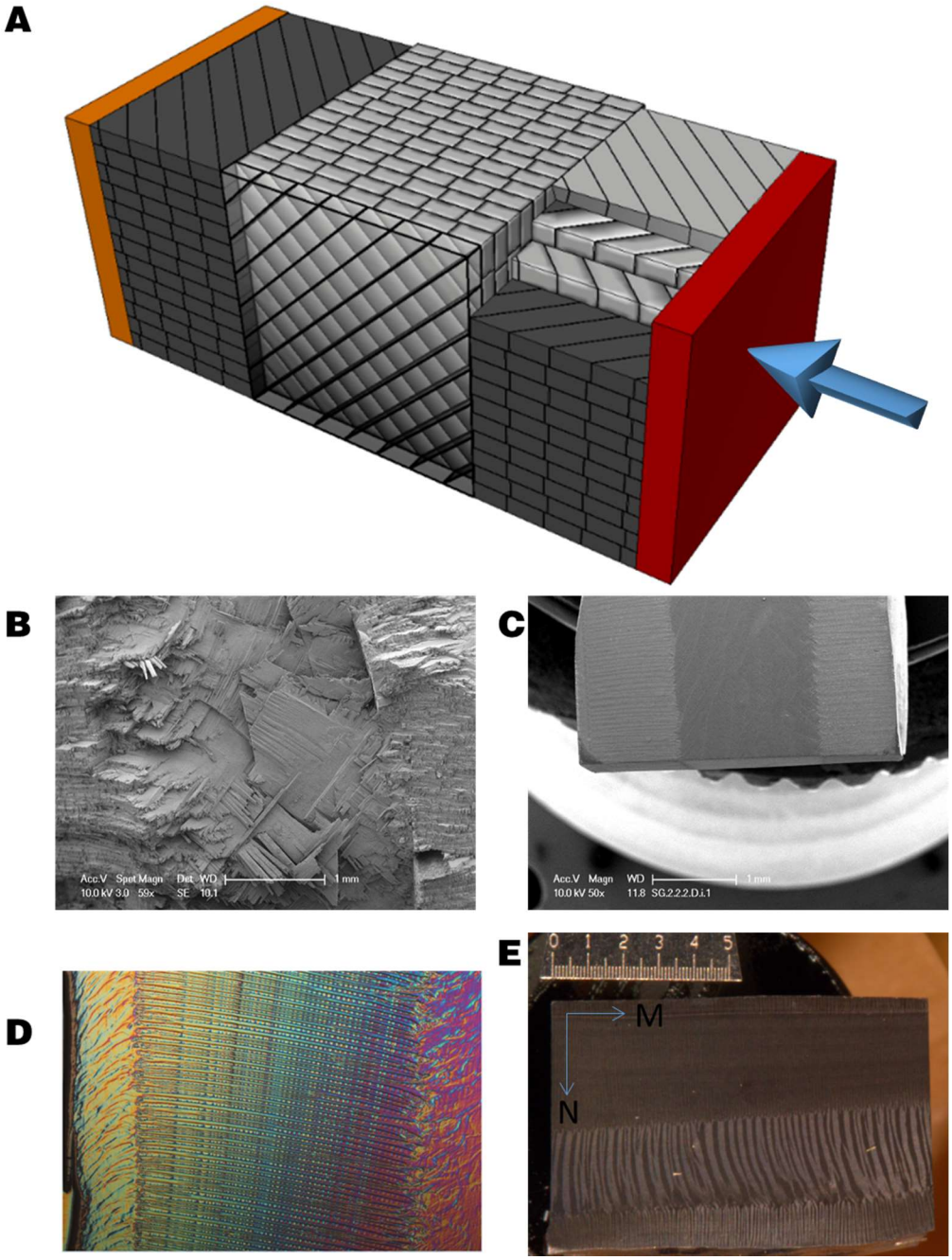

Figure 3-2 Model of multi-layer crossed lamellar gastropod shell, arrow depicting direction that force is applied during predation (A). Electron micrographs of *Strombus gigas* shell from the main whorl, fractured (B) and polished (C). Polarized light micrograph of shell cross-section (D). Optical micrograph of coated sample, note contrast between and within the shell layers (E).

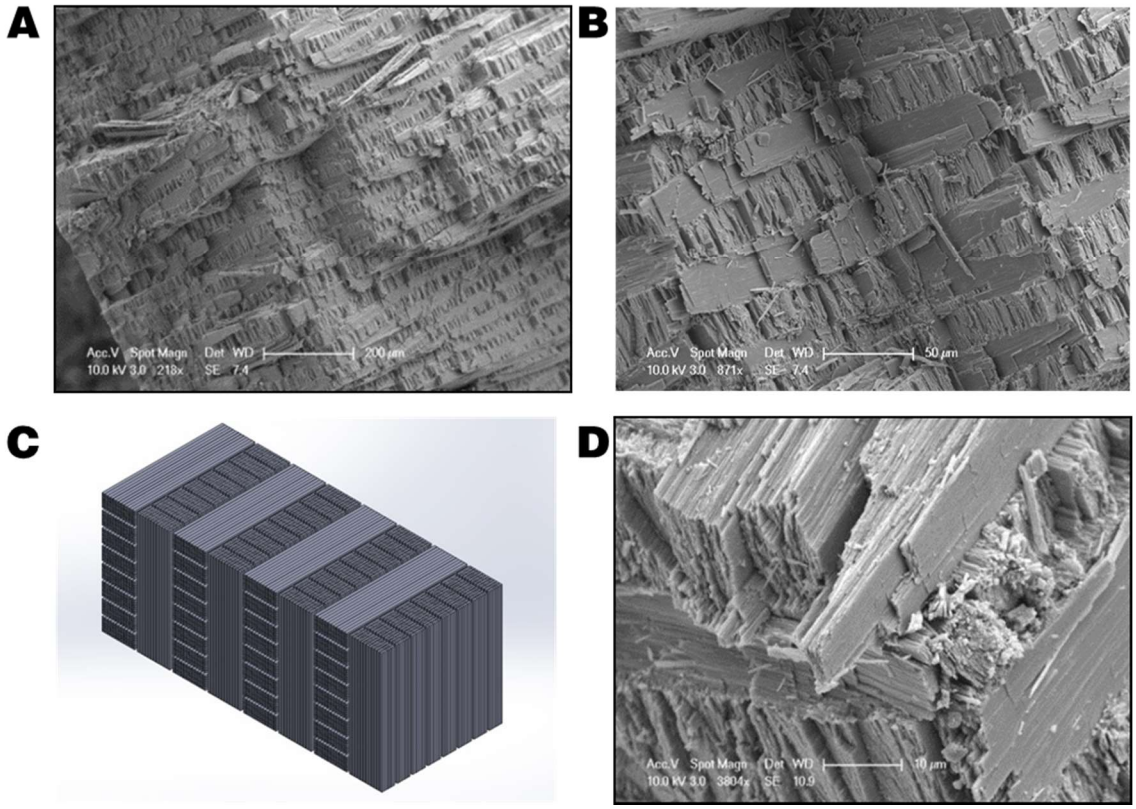

Figure 3-3 1st order lamellae of the crossed lamellar microstructure from *S. gigas*. Macro layer (0th order) consist of numerous parallel 1st order sheets (A). The adjacent 1st order has orthogonal fiber directions, which are responsible for the contrast present between layers (B). 3d model of a series of 1st order lamellae of a primitive crossed lamellar structure (C). Alternating dip direction between adjacent 1st order layers (D).

Within each of the three shell macro-layers, the crossed lamellar structure is composed of multiple parallel 1st order lamellae (Figure 3-3), which are unidirectional sheets formed from multiple 2nd order bundles, are stacked with alternating perpendicular 2nd order directions between adjacent layers. The 1st order lamellae are composed of many parallel 2nd order beams arranged into a sheet (Figure 3-4). The 2nd order lamellae are 10-20 μm wide, 20-50 μm thick, and up to several hundred micrometers in length and composed of tens of thousands of 3rd order lamellae to form a rectangular beam. The 3rd order lamellae are nearly

rectangular planks in shape, approximately 150 nm wide by 100 nm thick and several micrometers in length and are surrounded by a thin organic sheath (Figure 3-5). The 3rd order planks are formed from numerous 4th order particles (Figure 3-6).

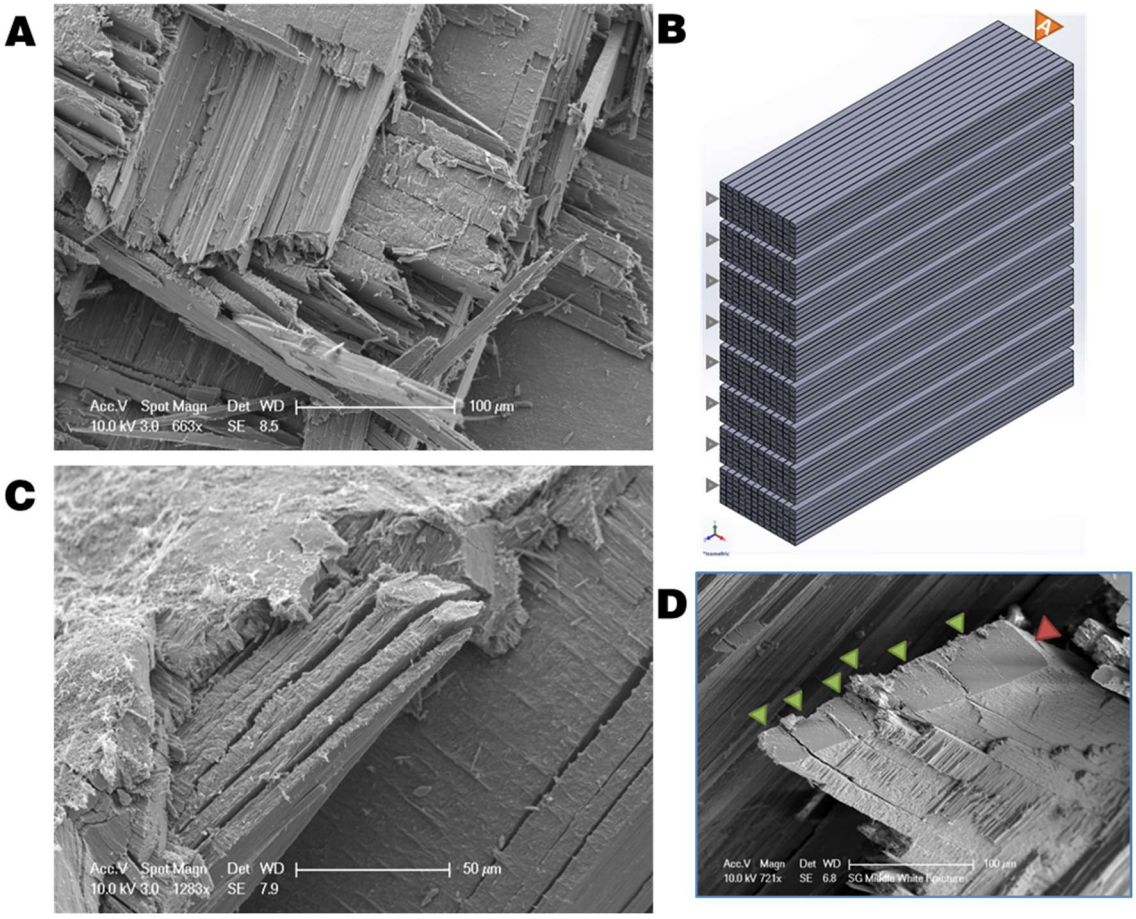

Figure 3-4 2nd order lamellae of the crossed lamellar microstructure from *S.gigas*. The 1st order sheets are composed of rectangular bundles of fibers, 2nd order planks (A and B). The interface between adjacent 2nd order planks is smooth and parallel, allowing for delamination during fracture (C). Within a 1st order lamella (red triangle) there appears to be additional features that span across multiple 2nd order lamellae (green triangles) (D).

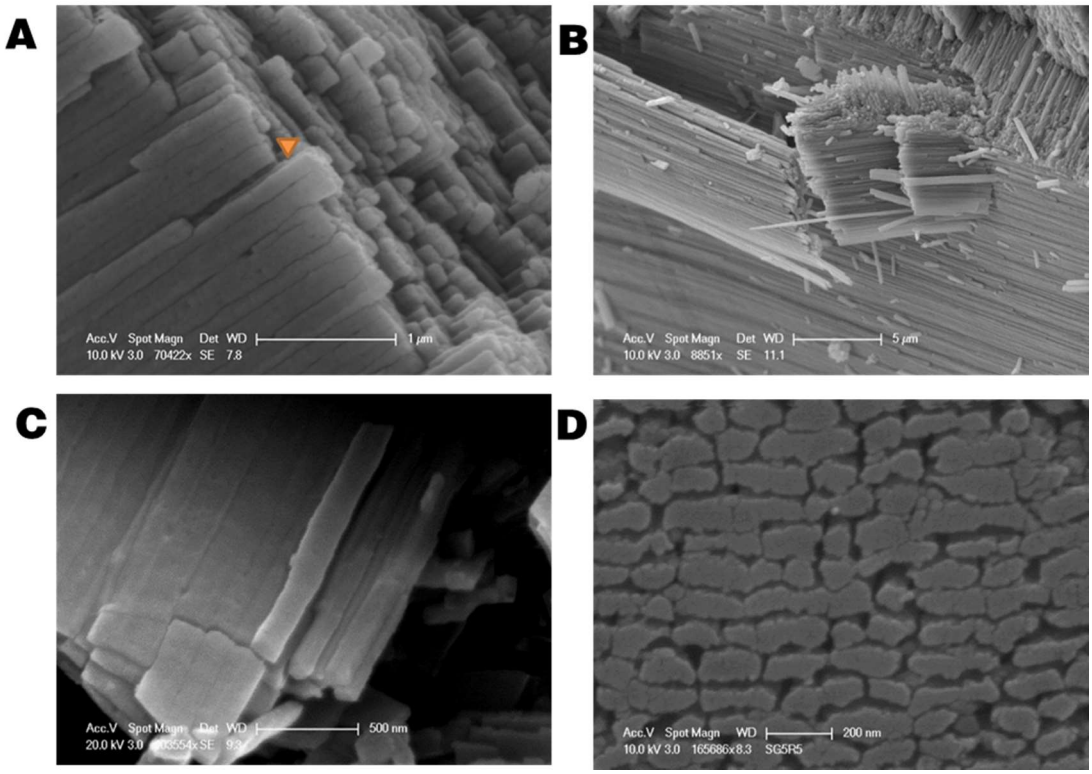

Figure 3-5 3rd order lamellae of the crossed lamellar microstructure from *S.gigas*. The 3rd order fibers are rectangular in cross section (~100 nm x ~150-200 nm) and several μmin length. The fibers are locally co-linear within a single 1st order lamella (A and B). Within a 2nd order lamella there are additional features that span across neighboring 3rd order lamellae (C). The fibers are arranged with semi-regular square packing (D).

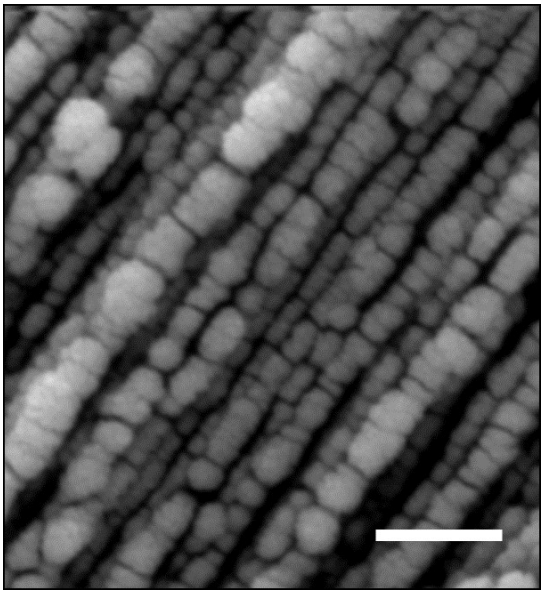

Figure 3-6 4th order particles of the crossed lamellar microstructure from *S.gigas*. Spherical 4th order sub-units construct the 3rd order lamellae. 4th order particles appear to be aligned into fibers. Sample treated with NaClO to increase contrast.

The remarkable toughness of the crossed lamellar structure of the gastropod shell is due to a number of structural features. During loading of the shell, multiple cracks are initiated within the inner layer due to a difference in toughness between the “weak” inner and “tough” middle layers (2). Each macro-layer has a “weak” direction that under an applied load, causes delamination along 1st order lamellar interfaces. However because the direction of 1st order lamellae is nearly perpendicular between adjacent macro-layers, a fracture that propagates along the weak direction in one layer is redirected at the interface of the adjacent layer. Within a 1st order lamella there are two principle directions in which a crack can grow: the weak direction, which causes delamination along 2nd order interfaces, and the strong direction where the 3rd order lamellae are in tension (Figure 3-7). Fractures along the weak direction of 1st order lamellae are bridged

by adjacent 1st order lamellae that have their 2nd order lamellae oriented in a perpendicular direction. The 1st order interfaces are rough, which increase the friction between adjacent layers allowing for load to be transferred (*2-4*) (Figure 3-8).

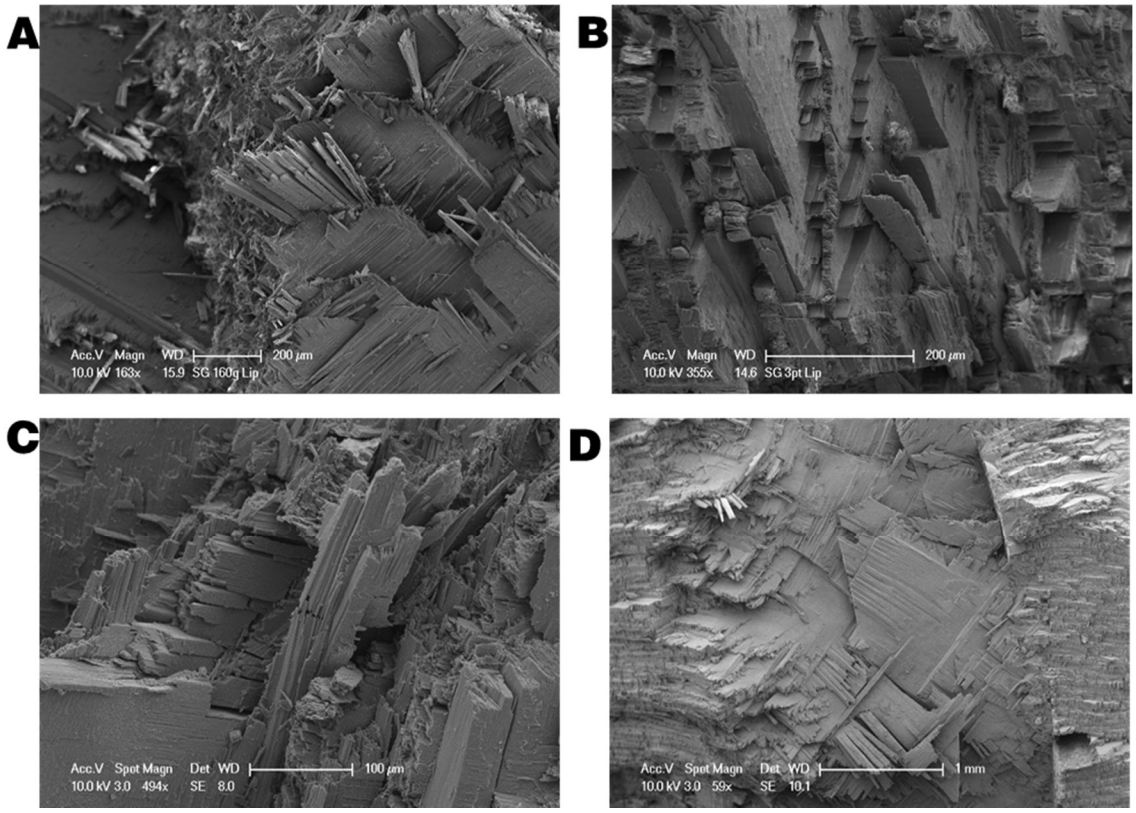

Figure 3-7 Fractured *Strombus gigas* shells. Minimal resistance to delamination along 2nd order interfaces (A). Saw-tooth fractures as cracks are redirected due to alternating fiber directions (B). Fiber bridging by adjacent layers (C). Rotation of CL structure between layers (D).

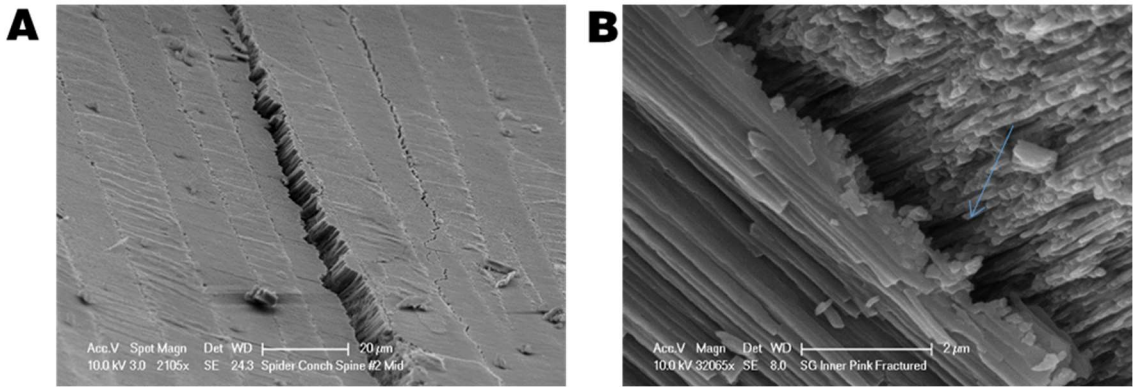

Figure 3-8 Rough interface between adjacent 1st order lamellae. Failure within 1st order lamellae suggesting inter-1st order strength is greater than intra-1st order strength (A). At the interface between 1st order lamellae, the structure becomes interdigitated (B).

3.3. Nanoindentation on the Crossed Lamellar Microstructure of the *Strombus gigas* Shell

Previous nanoindentation studies have shown that the hardness variation found in the different layers of the crossed lamellar structure is related to the crystallographic orientation of the aragonite mineral within each layer. There is an increase in the rate of crack nucleation within the 3rd order lamellae compared to abiotic aragonite, due to the hierarchical internal 3rd order nanostructure (*5*). To further understand the fracture mechanisms of the crossed lamellar system, we investigate the inner crossed lamellar layers of *Strombus gigas* using nanoindentation and finite element analyses. The resistance to penetration of different alignments of 3rd order lamellae (β) (Figure 3-9 A) was measured and the role, if any, of the alignment of the indenter geometry (α) (Figure 3-9 B) has on the observed fracture patterns was determined.

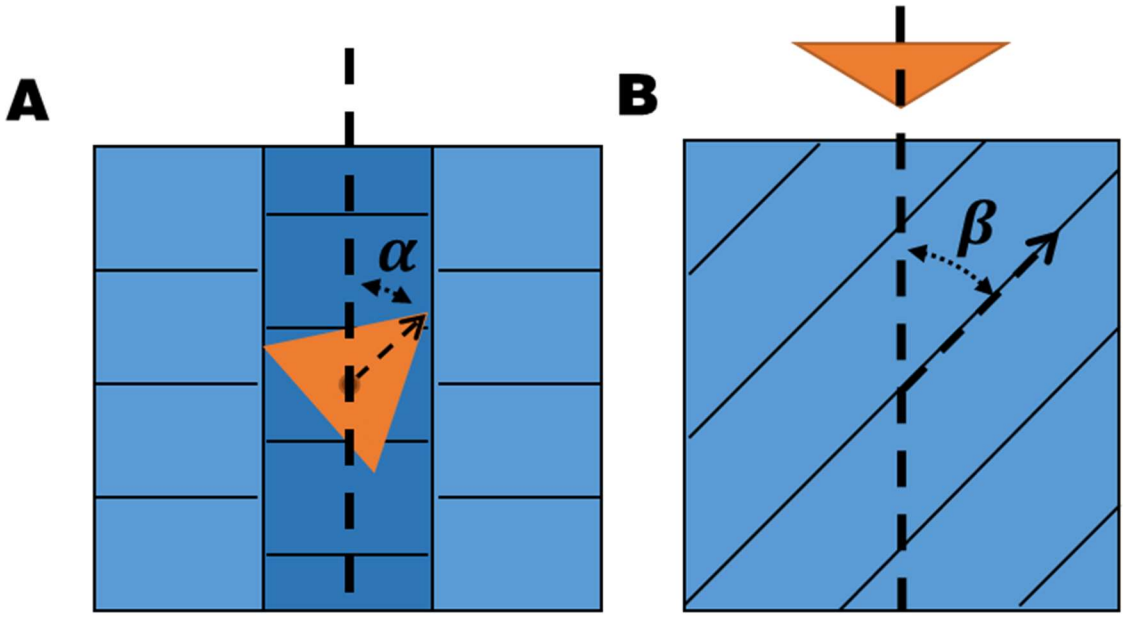

Figure 3-9 Orientation of indenter probe with crossed lamellar microstructure. α is the angle between the corner of the indenter probe and the 1st order interface (A). β describes the degree of tilt of the 2nd order lamellae from the indentation axis (B).

3.4. Materials and Methods

3.4.1. Preparation of *Strombus gigas* Shell

Dried *Strombus gigas* shells were obtained from a commercial vendor. Sections of the shell were taken from the main whorl, where the inner surface (pink) was sectioned using a rotary tool with a diamond embedded cut-off wheel. Sections of the shell were chosen for their thickness and uniformity of the inner layer. Samples were embedded in epoxy resin and polished with diamond suspensions down to 50 nm. After initial polishing, the alignment of the crossed lamellar system within the inner layer was determined using optical microscopy using two factors: 1st order tilt (γ) and 2nd order tilt (β). The degree of tilt can be observed by the angle between 2nd order and 1st order interfaces. In this study the

1st order tilt is approximately 0°, the 2nd order interfaces are perpendicular to 1st order interfaces (Figure 3-10). Once the initial alignment of the crossed lamellar system was determined, the samples were sectioned again to obtain the desired alignment of 3rd order lamellae (Figure 3-11).

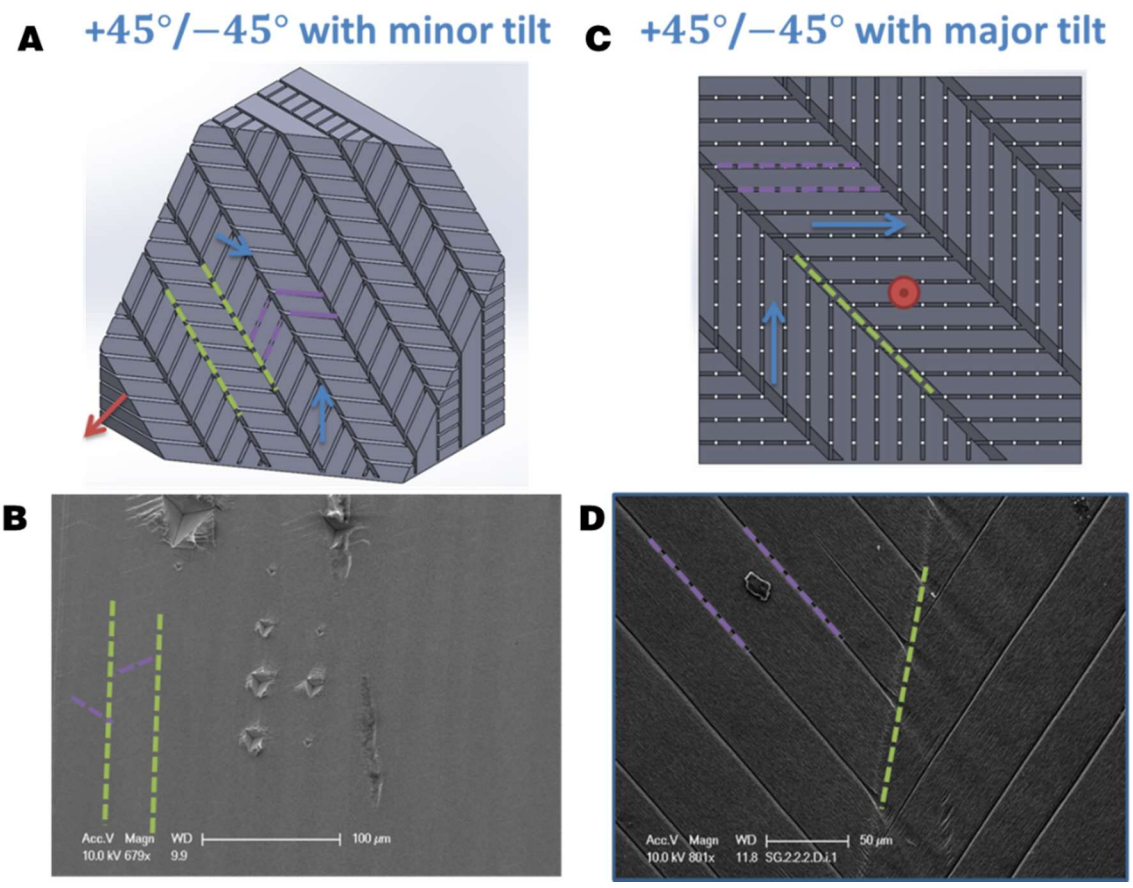

Figure 3-10 The appearance of the crossed lamellar microstructure for varying degrees of tilt. Schematic showing the 1st and 2nd order interfaces for minor tilts (A). SEM micrograph of crossed lamellar structure with minor tilt, 2nd order lamellae are nearly perpendicular to 1st order interface (B). Schematic of major tilt within crossed lamellar system (C). SEM micrograph of crossed lamellar with major tilt. 2nd order interfaces are nearly 45° from the 1st order interface. The long sides of the 2nd order lamellae are present between 1st order interfaces (D).

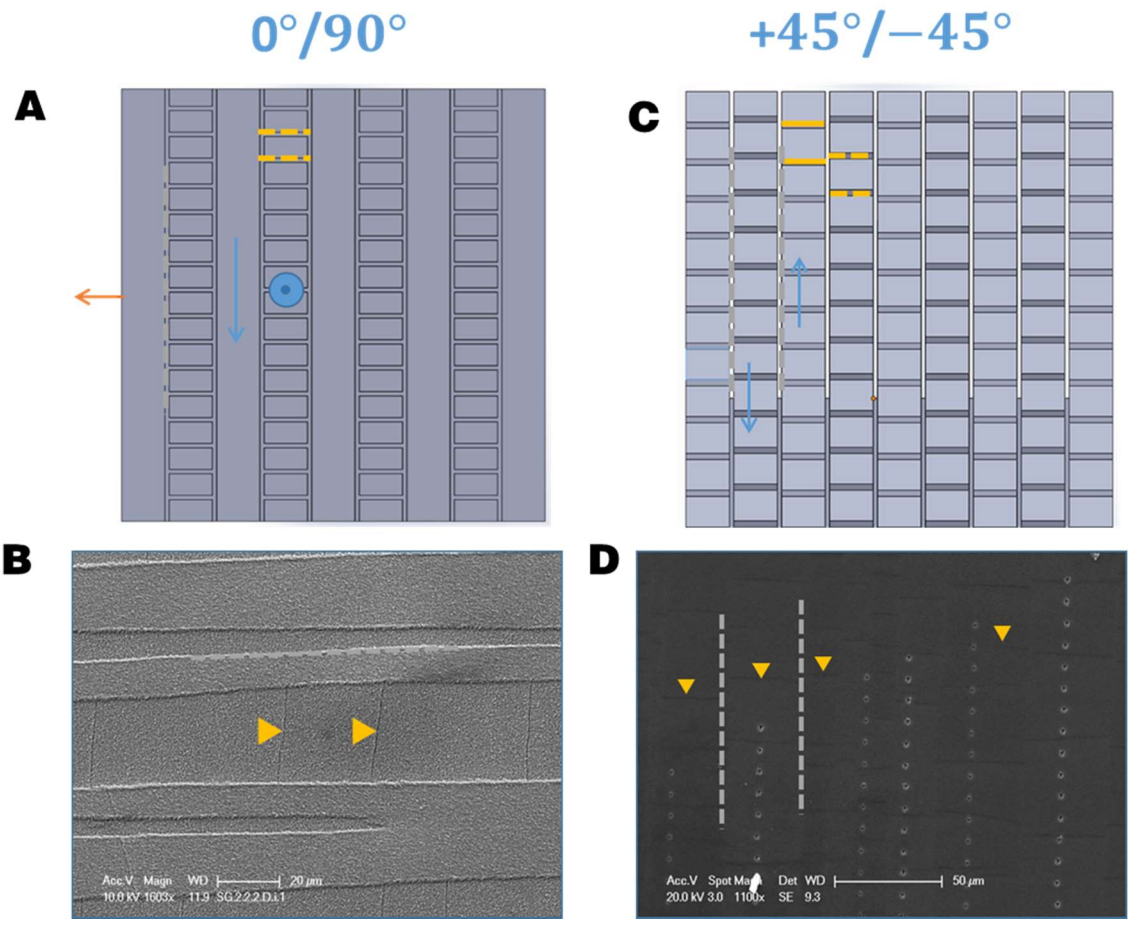

Figure 3-11 Alignment of the β parameter, which is determined by frequency of 2nd order interfaces. Minimum and maximum frequency for β =0 and β =90, schematic (A) and scanning electron micrograph (B). Similar frequency in both layers for β =45 and β =-45, schematic (C) and scanning electron micrograph (D).

3.4.2. **Nanoindentation**

Nanoindentation was performed using a TI-950 nanoindenter (Hysitron USA) equipped with both a low load (maximum 13mN) and a high load (maximum 15N) transducer that were both equipped with diamond cube corner probes. The indents were displacement controlled to a depth of 1µm and 10µm, which we refer to as low depth and high depth, respectively, at a displacement rate of 100 nm/s. Relatively wide and consistent first order lamellae were chosen and the indents

were placed along the center line of the 1st order lamellae. For both the high and low depth indents, four alignments of the 3rd order lamellae were tested: β=0°, β=-45°, β=45°, and β=90°. The angle of the indenter tip (α) is defined as the angle between the vertex of the indenter impression and the 1st order interface, with 0° defined as the case were the impression points away from the inner surface of the shell (Figure 3-9 A). For each value of β for low depth indents, the value of α was varied between 0° and 120° in 7.5° steps. The high depth indents were tested for two cases of α: 0° and 60°. After indentation, the samples were examined using scanning electron microscopy (SEM, Phillips XL-30) operated at 10-20 keV. To enhance conductivity and minimize charging during imaging, the samples were sputter coated with platinum and palladium.

3.4.3. Strain Rate Sensitivity

The sensitivity of the material to the loading rate applied was studied using three loading rates: 100 nm/s, 1,000 nm/s, and 10,000 nm/s.

3.5. Results

3.5.1. Nanoindentation

The maximum load required to displace the indenter probe 1μm into the sample depends greatly on both the orientation of the rods with respect to the surface (β) and the indenter rotation angle (α) (Figure 3-12 and Figure 3-13). The maximum resistance to penetration, 12,000 μN, occurs when β=0° and α=90°; where the 3rd order planks are parallel with the indentation direction (Figure 3-13 B). The least

resistance is observed were β=90° and α=60° (Figure 3-13 A). For β=±45°, the force required is 10,000 μN. When the orientation of the indenter is varied, significant variation is observed in the resistance to penetration for the β=90° and β=0° cases, with maximums occurring when misalignment is greatest (α=30°/90°) and minimums at (α=0°/60°/120). For β=±45°, the values do not vary significantly with rotation angle of the indenter and no clear minimum or maximum can be observed from the results (Figure 3-12 A and B).

An examination of the observed variance of measured mechanical properties between and within 1st order lamellae reveals that there is significant variation locally within a single 1st order lamella (Figure 3-14). It is unclear if the variation measured is limited by sample preparation or if it is inherent to the material being tested.

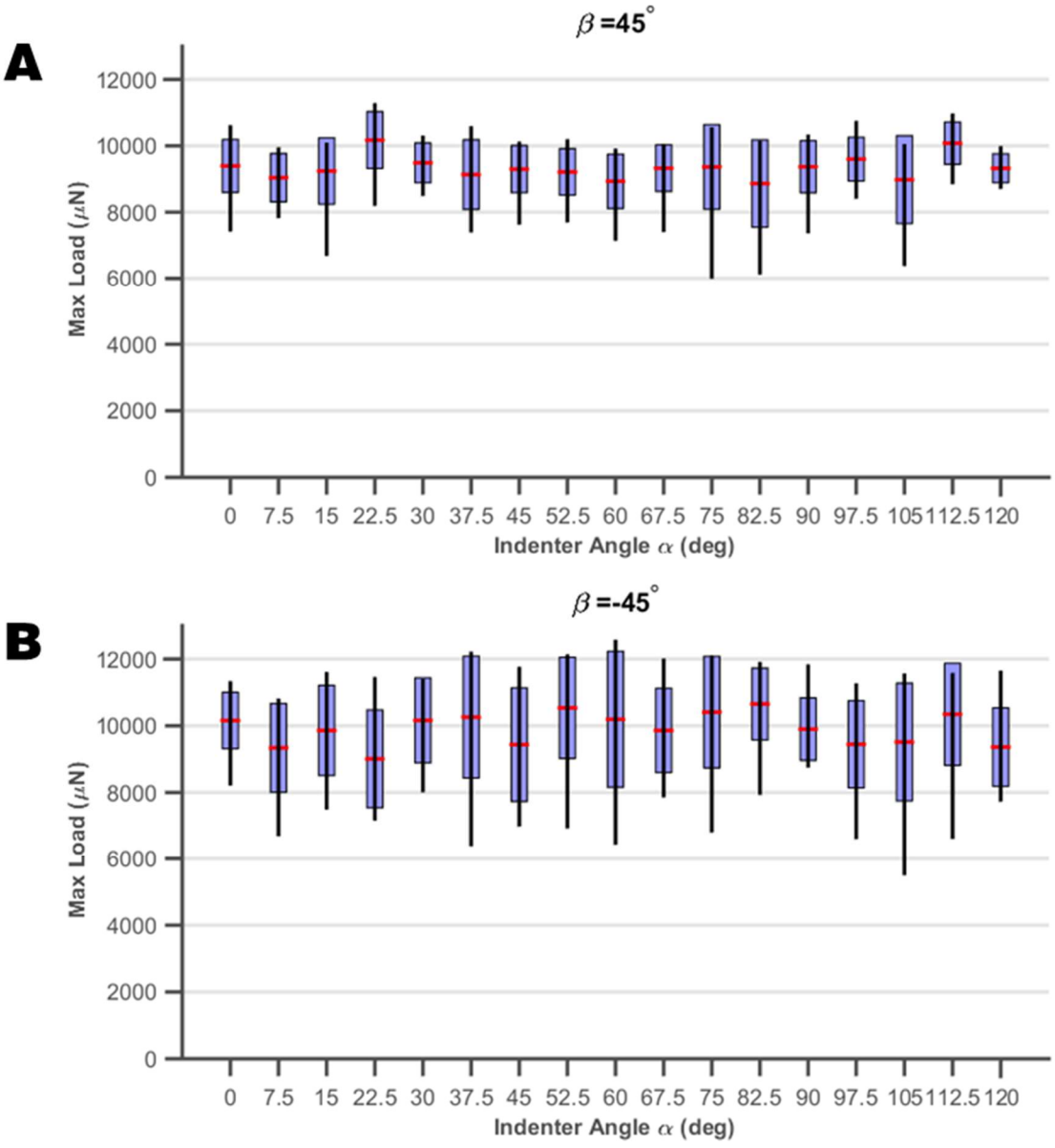

Figure 3-12 Maximum load observed during indentation to 1,000nm depth for different rotation angles of the indenter probe (α) and 3rd order tilt (β) β =45 ° (A) β =-45 ° (B).

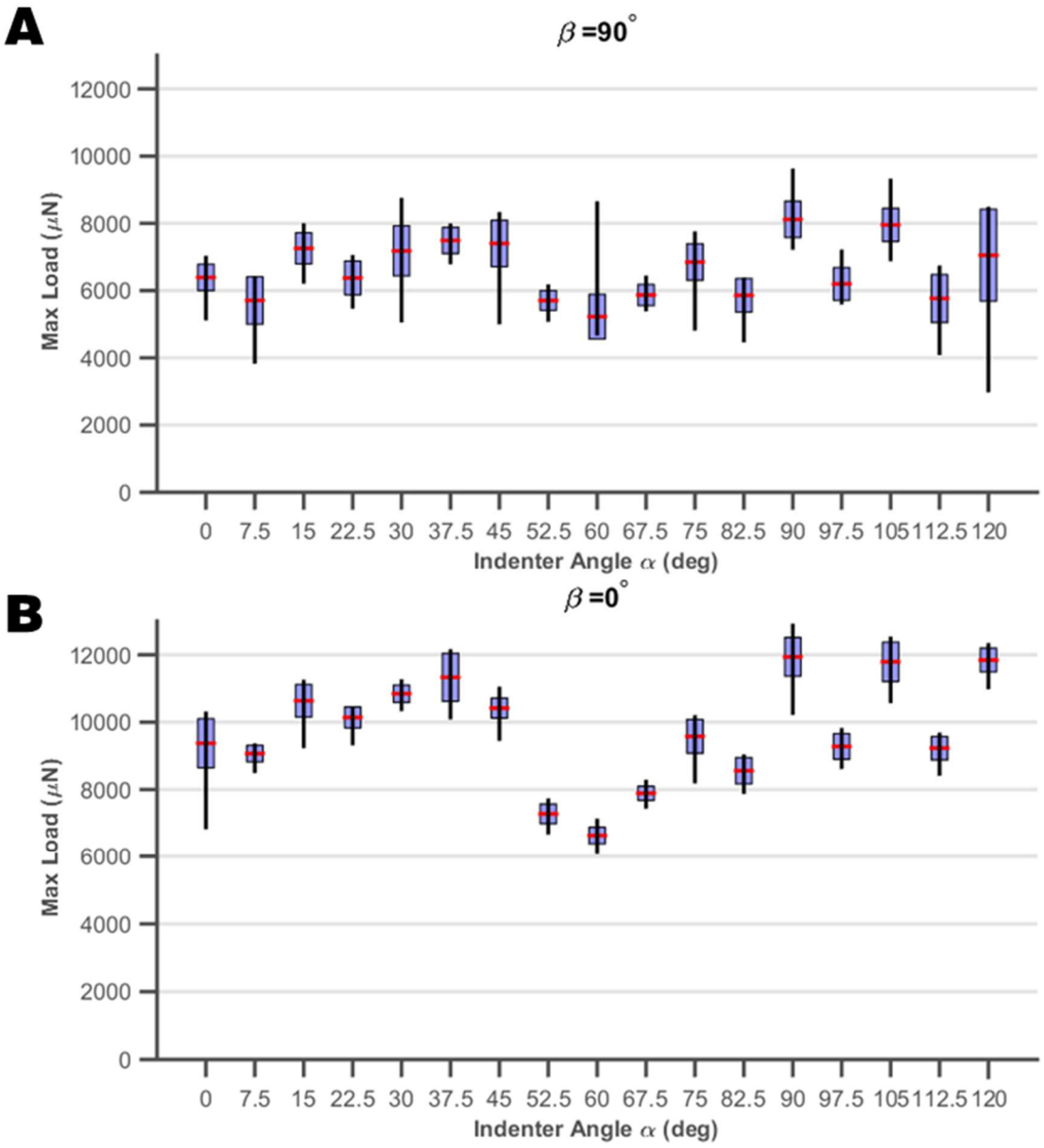

Figure 3-13 Maximum load observed during indentation to 1,000 nm depth for different rotation angles of the indenter probe (α) and 3rd order tilt (β) β =90 ° (A) β =0 ° (B).

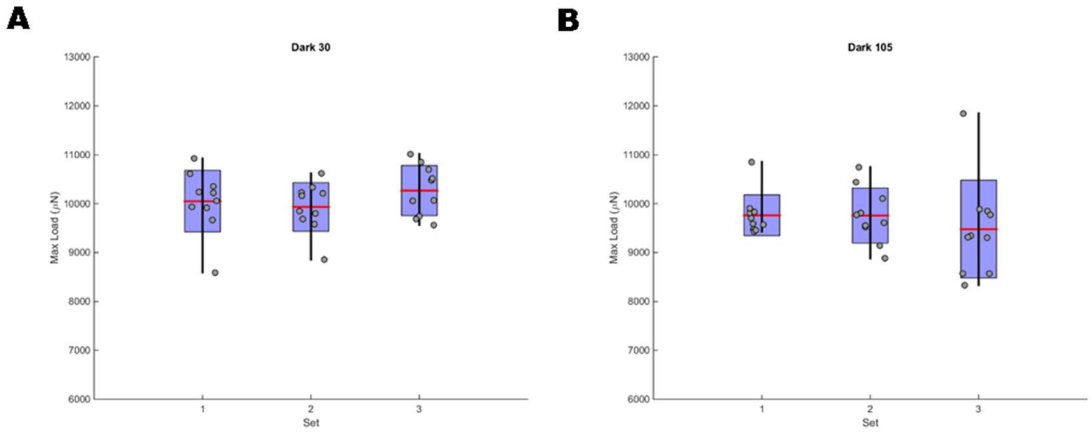

Figure 3-14 Examples of the variation within single values of α for β =-45°. Each group of indents was placed in individual 1st order lamellae.

Indentation at higher depths produced more pronounced fractures, which originate at the indentation site and continue to the surrounding 1st order interfaces where they appear to be arrested. The observed fracture patterns for β=+45° and β=-45° are related by a 180° rotation, upon which the two sets of indents appear similar (Figure 3-15 A, D, G, J). Post indentation microscopy unveils a number of different deformation mechanisms among the 3rd order lamellae, which are highly dependent on both the angle of lamellae and the geometry of the indenter. Asymmetric indentation impression are observed where β=+45° and β=-45° where α=0° and α=60° respectively (Figure 3-15 B and F). Interestingly in the opposite alignment of indenter, where β=+45°/-45° and α=60° /0° respectively, the resulting indent projection is an equilateral triangle as is expected for a cube corner indenter (Figure 3-15 C and E). The elongated face of the triangle points away from the direction of the 3rd order lamellae, the degree of elongation varies as the indenter is rotated between 0° and 60°.

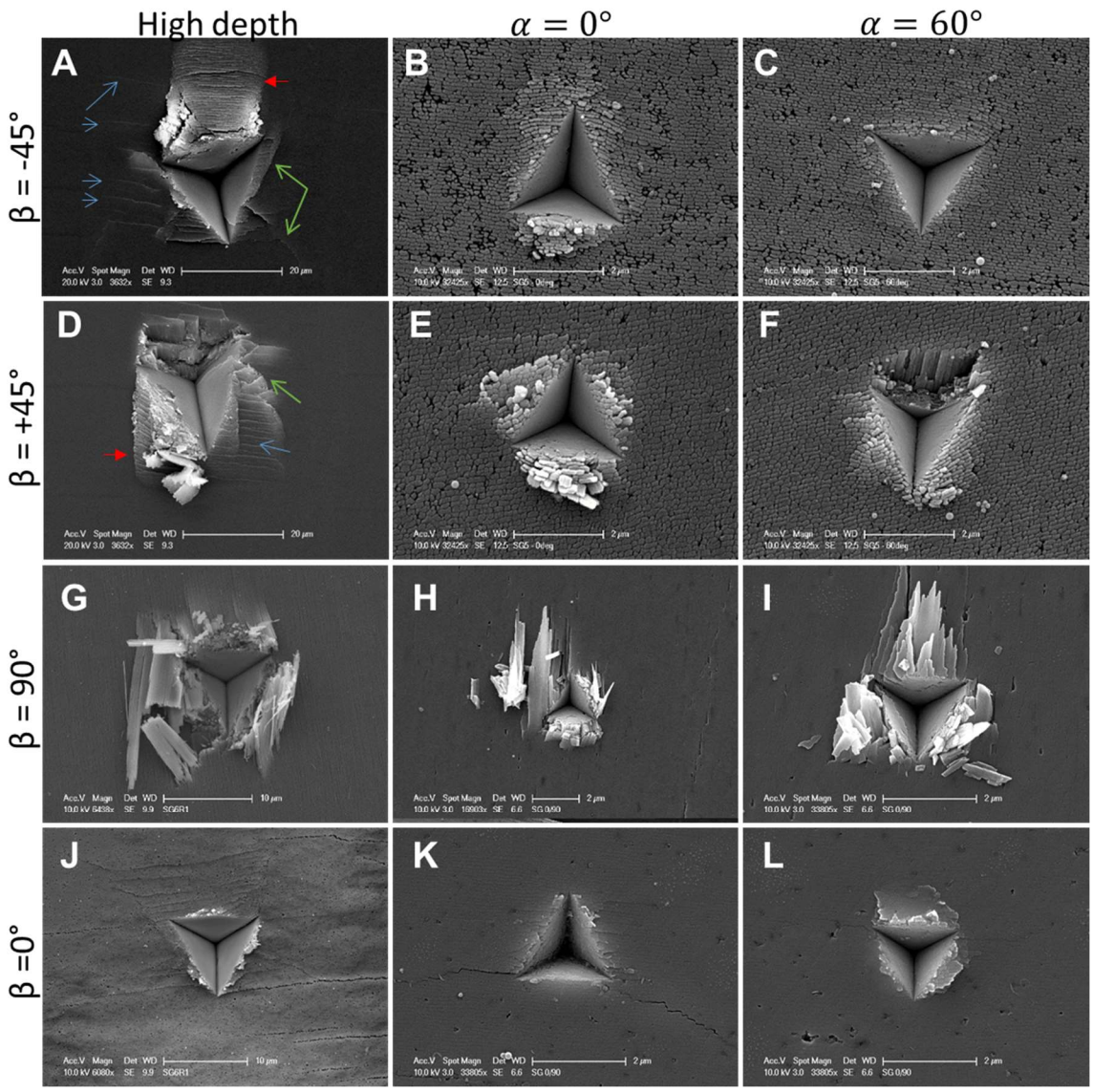

Figure 3-15 Representative indentation impression for four cases of beta, high (A,D,G,J) and low depth (B,C,E,F,H,I,K,L), and α =0° and α =60°. High depth reveal diagonal cracking and pile up, were the location of pileup switching between β =-45° (A) and β =45° (D). Indentation with the vertex anti-aligned with the projection of the 3rd order direction show anisotropic plastic deformation, resulting in a non-uniform residual indentation impression (B) and (F) in comparison to (C) and (E). β =90° α=60° 10,000 nm (G) β =90° α=0° 1,000 nm (H) β =90° α=60° 1,000 nm (I) β =0° α=60° 10,000 nm (J) β =0° α=0° 1,000 nm (K) β =0° α=60° 1,000 nm (L)

The surface of the residual indent impression is smooth and granular in appearance. This granular structure is observed for approximately 100 nm surrounding the indent, after which the structure of the 3rd order lamellae are

preserved (Figure 3-16). The plastic deformation of the 3rd order lamellae are enhanced by the hierarchical structure found within a 3rd order plank. Additional deformations of the 3rd order lamellae are observed in the regions surrounding the indenter impression. Lateral to the indent, away from the plank direction in the β=-45°, the rows of 3rd order lamellae are compressed along their thickness directions, while the boundaries are preserved (Figure 3-17). However when β=0°, the boundaries of the 3rd order lamellae, adjacent to the indent impression, have vanished during the deformation of the 3rd order lamellae along their width (Figure 3-15 K).

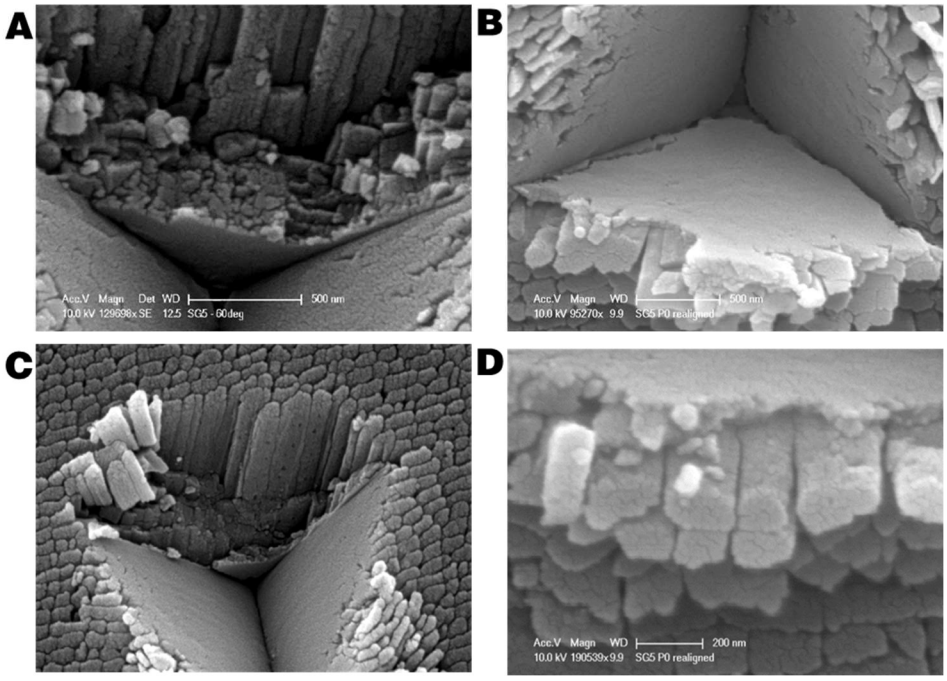

Figure 3-16 Plastic deformation at interfaces between the indenter and sample. Zone of damage radiating from the indenter face, resulting in destruction of 3rd order structures (A). Cracks form around edges of smoothed surfaces (B). Densely packed deformed sections can fracture and be pulled out during removal of indenter probe (C). Ends of rods appear to be blunted after loading (D).

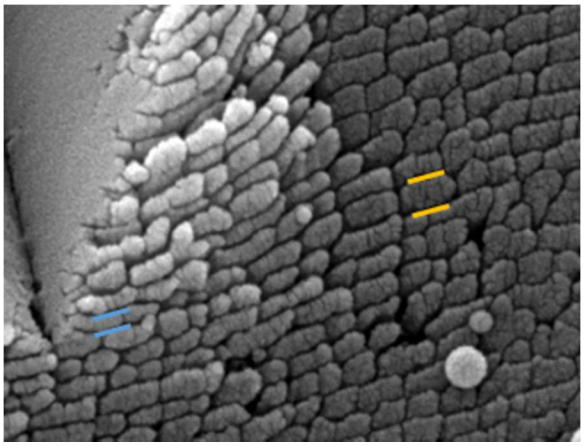

Figure 3-17 Thinning of the 3rd order lamellae in the stress field surrounding an indentation impression. Blue lines show the thickness of a compressed 3rd order lamella near the indent, yellow lines show the thickness of an uncompressed indent.

There are additional inter-3rd order lamellae energy dissipation mechanisms that were observed from the indentation event. Along the indenter face that is approximately perpendicular to the fiber direction, the third order lamellae are displaced and form a pile-up region with numerous cracks traveling between lamellae (Figure 3-18). The pile-up region is formed along the direction of the long axis of the planks, with minimal lateral spread, resulting in staggered vertically displaced planks. When the planks have a greater tilt with respect to the indentation axis, two different types of fractures are commonly observed. Mode I crack opening occurs during delamination between 3rd order lamellae, which results in bundles of 3rd order lamellae that are strained until fracture occurs within the 3rd order lamellae. As adjacent 3rd order lamellae are loaded in shear (mode II), there are interfacial features, which increase the resistance to sliding. Evidence of the sliding motion can be seen in the buckled 3rd order planks along the flat parallel indenter face when $\beta=90°$. The effects of further sliding motion can be observed

when the 3rd order lamellae are nearly parallel with the indenter face, in which case the lamellae are fractured near the tip of the indenter, and the planks are sheared along their length, resulting in a section of 3rd order lamellae to be pulled out with the indenter probe (Figure 3-16 B and D). These pulled out sections can be occasionally observed deposited on the surface of the subsequent indent. Additional fractures are observed traveling primarily laterally between rows of 3rd order lamellae, where they encounter resistance due to the interfacial strength between 3rd order lamellae. Arching fractures are observed originating from the sides of the indenter, taking a torturous path traveling diagonally between rows and columns of 3rd order lamellae, these arching delaminations continue until they reach a lateral delamination or the interface between adjacent 1st order lamellae (Figure 3-19).

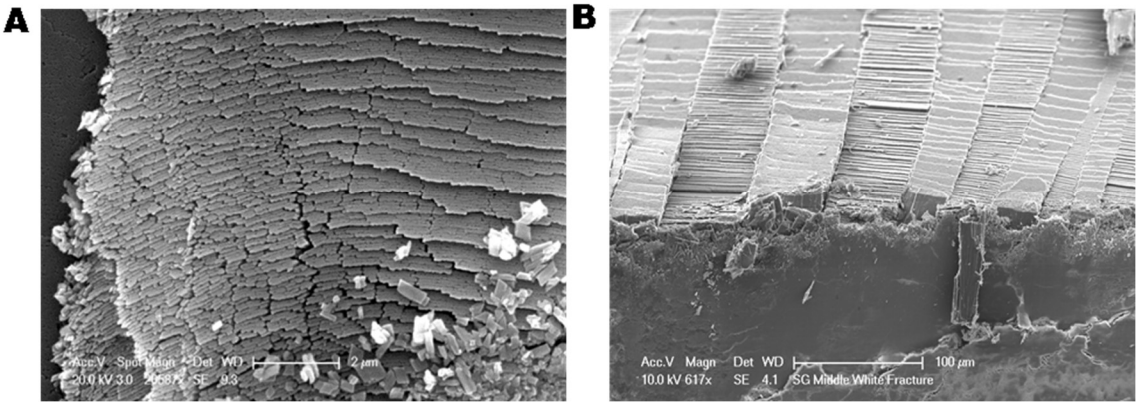

Figure 3-18 Pile-up, displaced 3rd order lamellae. SEM micrographs showing displaced “layers” of 3rd order lamellae resulting from indentation (A). Similar deformation occurs in bulk samples that are impacted with a flat chisel (B). Notice whole regions of 1st order lamellae are displaced into and out of the surface of the sample.

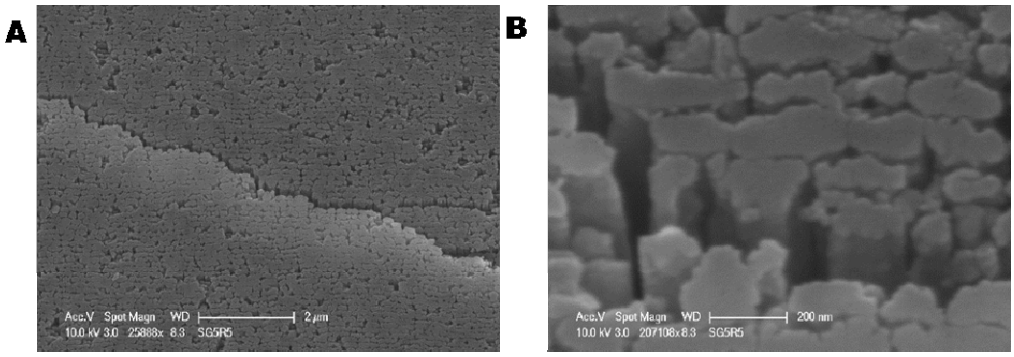

Figure 3-19 Torturous path taken by lateral cracks traveling between 3rd order lamellae within a 1st order lamella (A). Growth of cracks along the interface between 3rd order lamellae is impeded by mineral bridges joining adjacent planks (B).

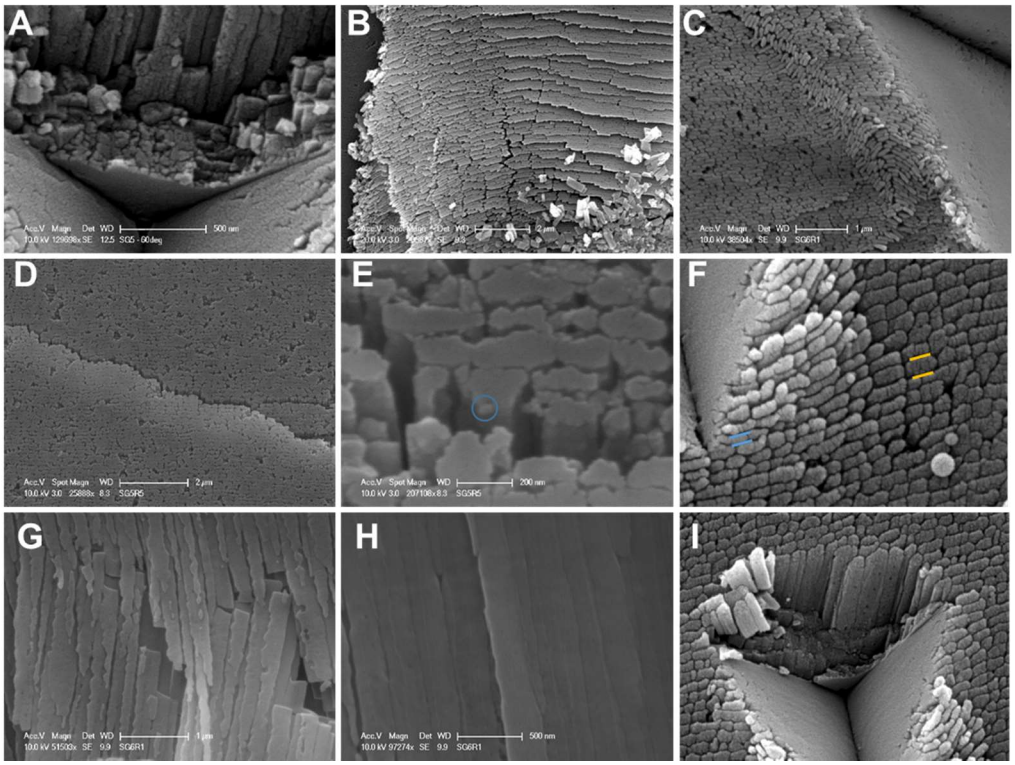

Figure 3-20 Different deformation mechanisms observed after indentation. Significant plastic deformation at the surface of the indenter as higher order features translate (A). Pile-up along the flat edge of the indenter probe, as inclined rods are deformed (B). Regions along the sides of the indenter showing bands of rotated 3rd order lamellae that have deformed to accommodate the change in volume (C). Inter-3rd order lamellar fracture, take a zig-zag path while traveling latterly were they are arrested at the 1st order interface (D). Fracture along rough interface between 3rd order lamellae (E). Compressive deformation of 3rd order lamella surrounding indent, thinned 3rd order (F). Lateral displacement and the resulting smooth fracture across 3rd order lamellae (G). The surface of delaminated of 3rd order lamellae (H). Fiber pullout around indenter face of 3rd order lamellae that have been fractured by shearing (I).

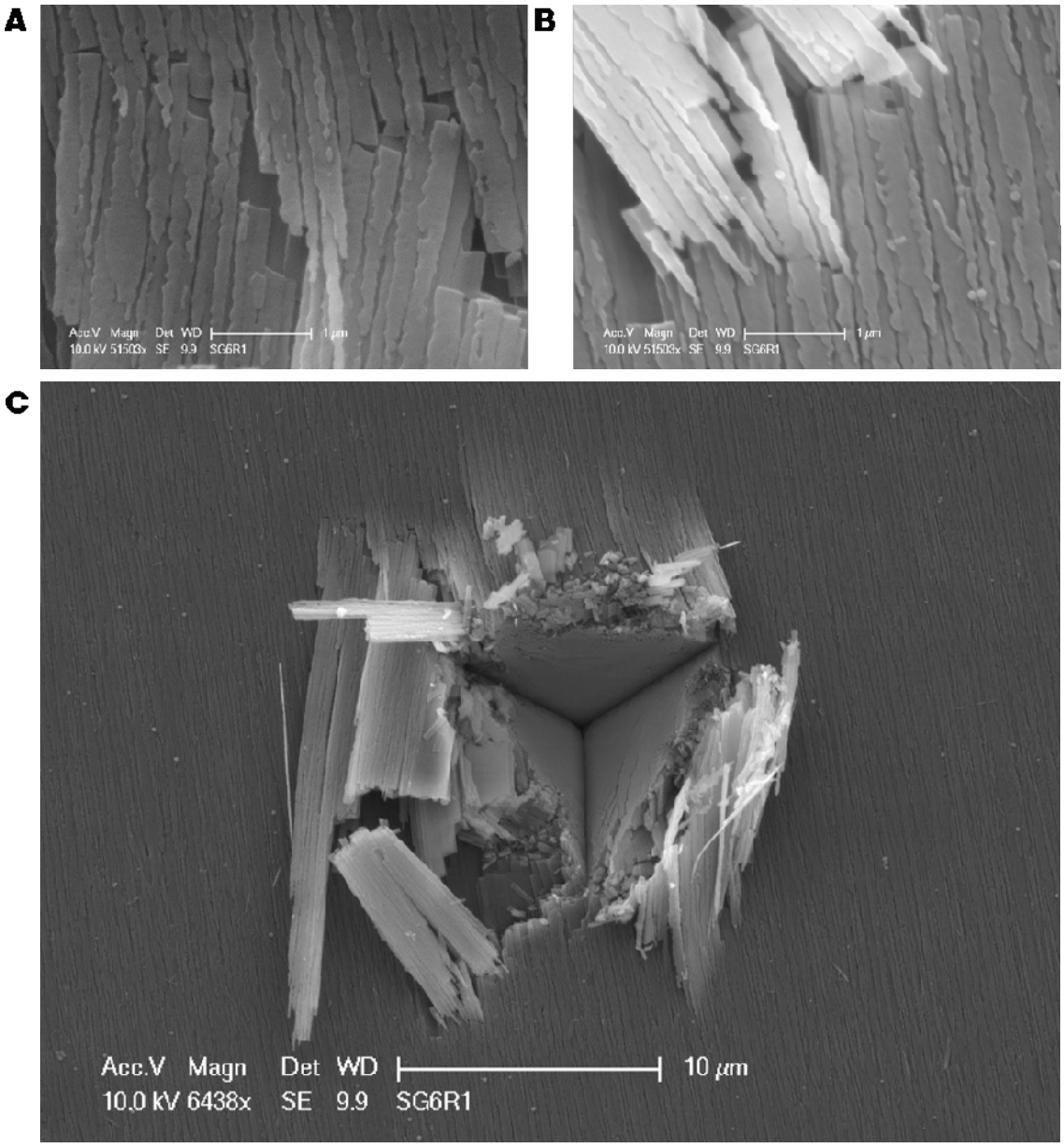

Figure 3-21 Fracture of 3rd order lamellae. Lateral forces are applied by pyramidal indenter. Fracture surface of 3rd order lamellae appears smooth across the width of the fiber (A). Variation of bending fracture is observed due to variations in direction of applied force (B). Combination of both deformation types observed around the location of an indent. Changes in appearance are due to the variance of angle between the 3rd order lamellae and the facets of the cube corner indenter (C).

Additional fracture patterns were observed along the non-parallel indenter faces. When β=90°, 3rd order lamellae are displaced laterally away from the indent

where they eventually fracture across the 3rd order lamellae at a considerable distance away from the indent (Figure 3-20). When β=0°, the 3rd order lamellae in the zone surrounding the indent are rotated/twisted during the indent, allowing the structure to absorb the displacement caused by the indenter. The rotated lamellae typically found in bands between two regions of 3rd order lamellae that have not been rotated (Figure 3-21).

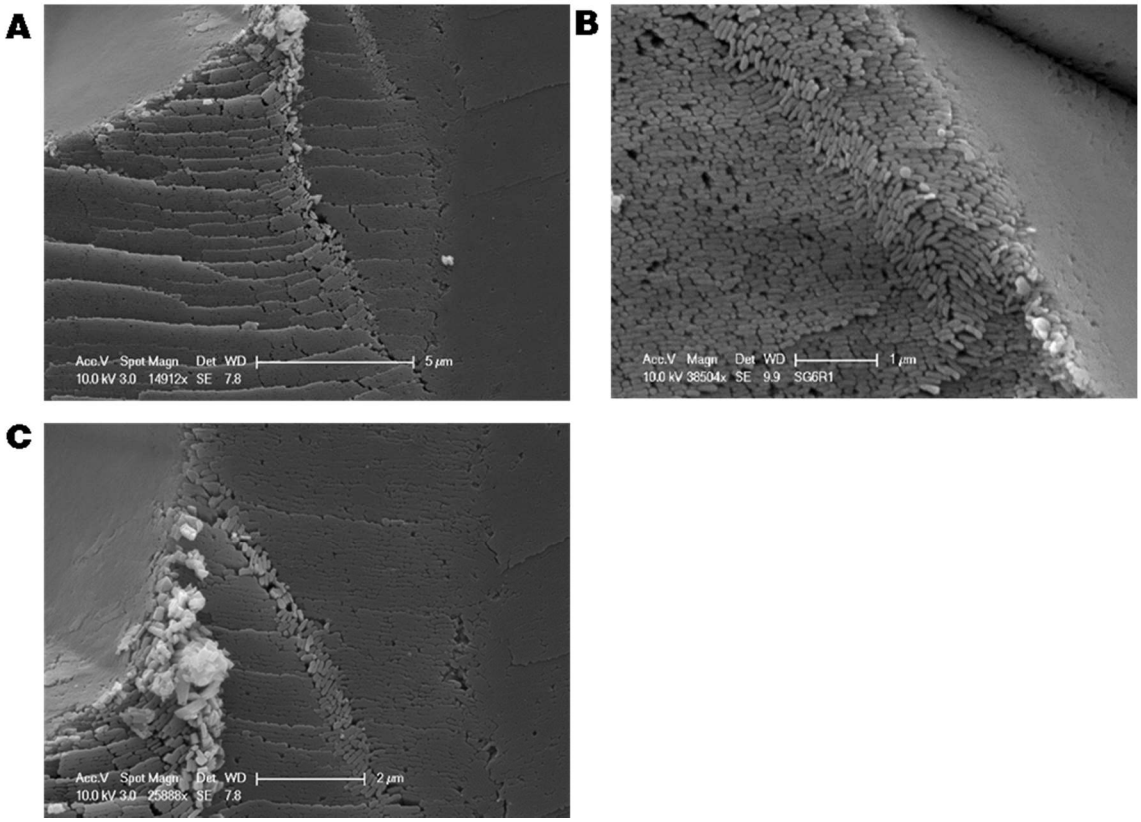

Figure 3-22 Rotation of 3rd order lamellae in the area surrounding an indent. Bands of 3rd order lamellae are sheered and rotated during deformation. Allowing the structure to absorb large displacements (A). Near the surface of the indent the 3rd order lamellae are rotated in both directions (B). The rotation band may act to arrest lateral fractures within a 1st order lamella (C).

3.5.2. **Anisotropic Indentation**

The measured resistance to penetration and observed residual indentation impressions depend greatly on the orientation of both α and β. However, calculated properties, such as elastic modulus, do not show a similar trend. (*2, 3, 6-19*) Distinct differences are observed in the fitting parameters used to determine the elastic modulus, m, in 1st order lamellae of *Strombus gigas* shell (Figure 3-23).

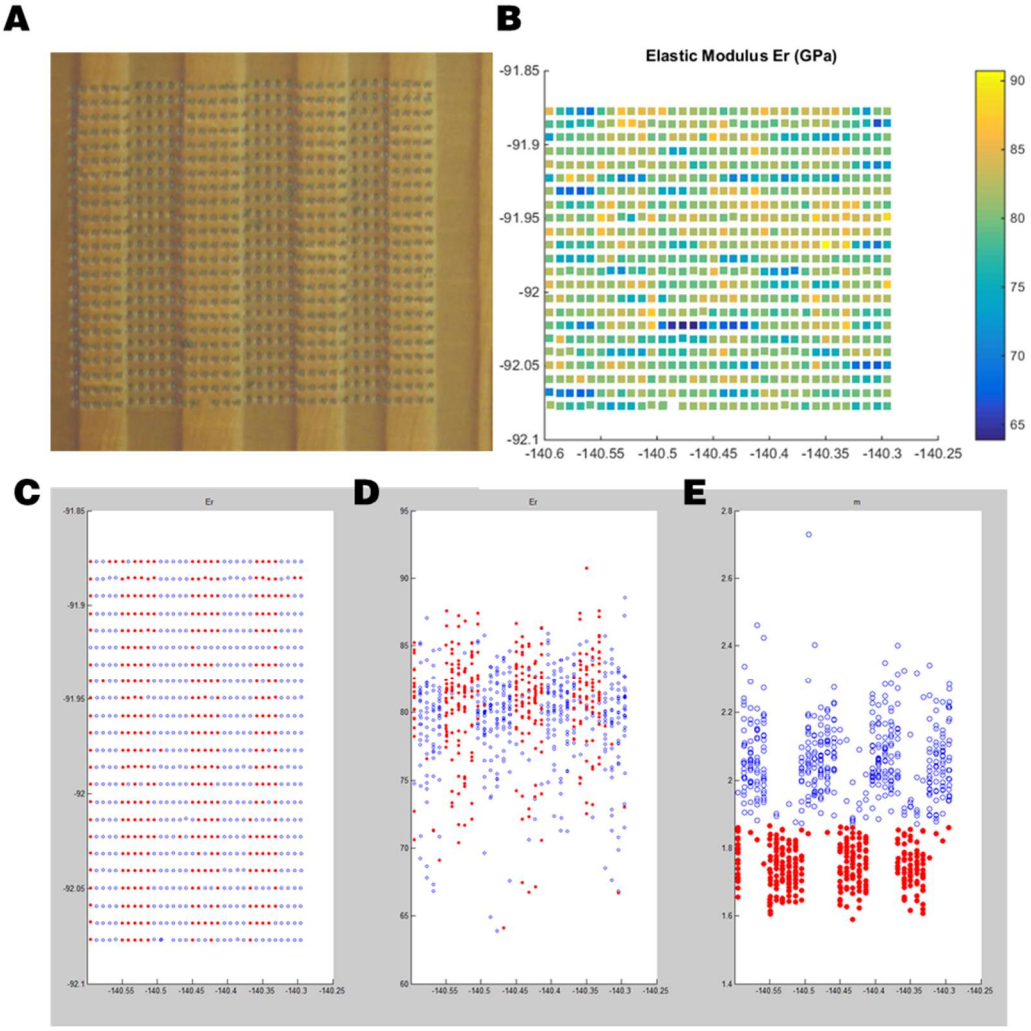

Figure 3-23 Elastic modulus analysis of nanoindentation from *Strombus gigas*. Optical micrograph of grid of indentation events, from the inner crossed lamellar layer $\beta = \pm 45°$ (A). Map of elastic modulus values calculated showing no significant correlation with the observed microstructure (B). XY map of the value of m exponential coefficient from the power law fit to determine the elastic modulus, points where m <1.85 and m>1.85 are colored red ($\beta = -45°$) and blue ($\beta = +45°$) respectively (C). Elastic modulus vs distance in X (D). The m parameter vs distance in X (E). The m value for a 1st order lamellae depends on the tilt of the fibers from the surface.

3.6. Discussion

The crossed lamellar structure is a hierarchical structure composed of nanometer to millimeter length scale features. The bulk toughening features found in the 1st and 0th order lamellae have been investigated in previous studies and

were primarily identified as crack bridging and crack bifurcation (*2*). Within a single 1st order lamella, we observed additional potential toughing agents between and within the 3rd order lamellae. Each 3rd order lamella is enveloped in an organic material sheath, separating it from adjacent mineral planks, which can dissipate energy through crack deflection as well as plastic deformation upon displacement. While the 3rd order lamellae are described as plank-like in profile, it is observed that the profile of the plank undulates and forms an interlocking wavy interface between adjacent 3rd order lamellae (Figure 3-24). The wavy nature of this interface provides resistance to 3rd order lamellae sliding, as the lamellae slide the undulations transfer the load in a perpendicular direction increasing the frictional force resisting motion in the loading direction, analogous to interlocking mechanism between mineral tablets in gastropod nacre.(*8, 20*)

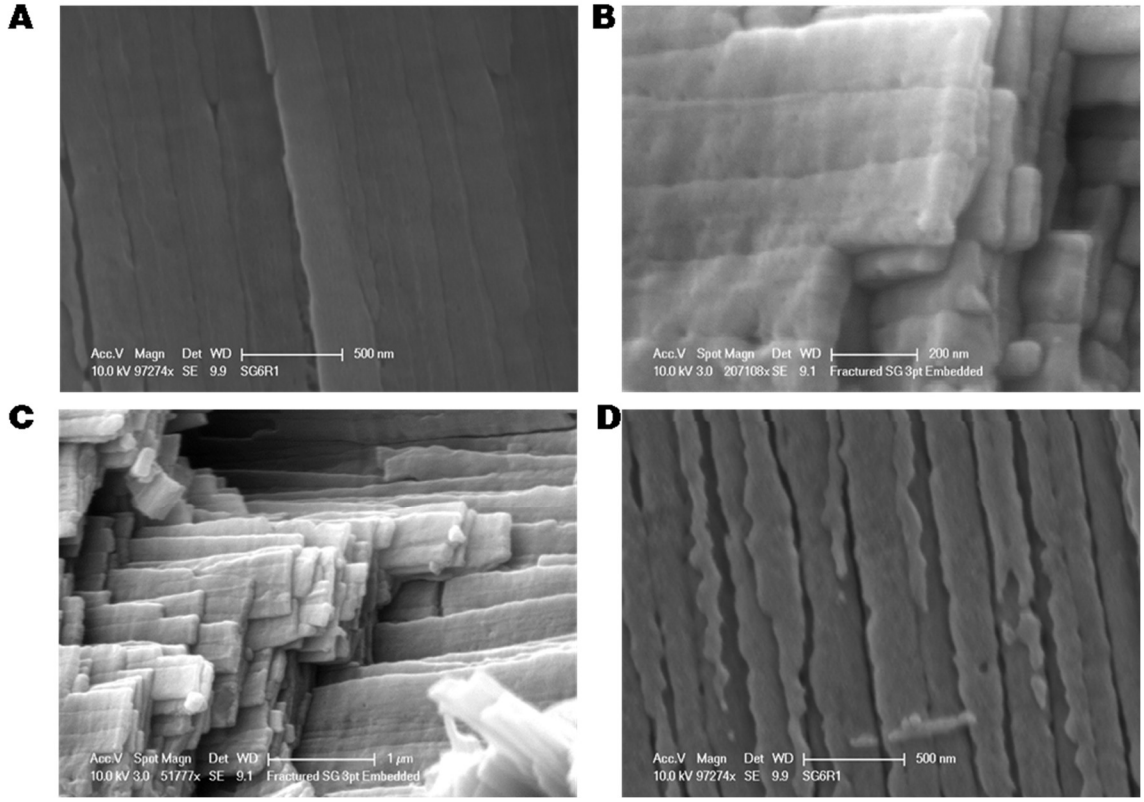

Figure 3-24 Surface features of 3rd order lamellae of *S. gigas*. Undulating wavy interfaces between 3rd order lamellae (A). Ridges span multiple 3rd order lamellae (B). Ridges spanning the width of 3rd order lamellae (C). Preferential removal of material during polishing, edge of fiber is softer than core (D).

Mineral asperities and potential mineral bridges are found along the long faces of the 3rd order lamellae and act as either sources of friction (i.e., mineral asperities) or as weak sacrificial mineral bonds between adjacent rows of lamellae, which must be severed during the lateral displacement of the lamellae. Evidence of mineral asperities is found on the surfaces of disaggregated 3rd order lamellae as islands or rough clusters of mineral. These are also observed along the faces of 3rd order lamellae that have become delaminated during indentation, where they are observed as pits or mounds in the surface of the lamellae.

The inter-reinforcement features found in the crossed lamellar system are similar to those observed in the other gastropod microstructures, such as the nacre structure, where mineral bridges, mineral-asperities, tablet thickness undulations, and inter-tablet organic are responsible for the three orders of magnitude toughness increase over geologic aragonite (*21-23*).

In addition to the inter-3rd order lamellae toughening features, there are structural features found within a 3rd order lamella. The 3rd order planks are composed of at least one more level of hierarchy, which are the spherical-like 4th order particles, which are irregular in size and shape but grow to form a densely packed structure within the 3rd order lamellae. Potential rotation and translation of these 4th order particles under loading increases the plasticity of the 3rd order lamellae as compared to a monolithic aragonite plank. The plastic nature of these 3rd order lamellae is observed at the surface of the indentation impression, where a blocky and dense structure occurs as the 4th order lamellae are displaced from their 3rd order lamellae (Figure 3-16).

The 4th order particles possess numerous {110} twins, which have their (110) planes aligned parallel to 1st order interfaces. The density of twins found in crossed lamellar gastropod shells is significantly higher than the density of twins observed in the geologic aragonite and nacreous aragonite (*24*). The numerous intrinsic twins in the crossed lamellar aragonite increases the energy required to form new twins within the mineral, which results in an increase in the hardness in the [110] direction. The high density of polysynthetic twins in the [110] direction

decreases the plasticity of the 4th order particles in the lateral direction across the 1st order to overcome the intrinsic anisotropicity of aragonite.(*25*)

Though the 3rd order lamellae are composed of smaller particles, they diffract as a nearly single crystalline plank and they form a crystallographic coherent structure the spans across numerous 1st order lamellae. The c-axis of the aragonite mineral within a 3rd order is tilted approximately 30° from the long axis of the 3rd order plank. Indentation experiments on geologic aragonite have shown that the hardness is greatest parallel to the c-axis with a hardness of 6.2 GPa, while the hardness perpendicular to the c-axis is 3.1 GPa (*5*). In gastropod shells the crossed lamellar structure is typically arranged with the 3rd order lamellae ±45° from the radial direction, resulting in the c-axis tilted approximately ±15° from the radial direction. The tilted crystallographic structure enables the crossed lamellar system to benefit from a combined fracture resistant microstructure and maximized hardness of the mineral in the loading direction.

3.7. Conclusions

In this study, the careful control of the alignment of the crossed lamellar microstructure is enabled by the large, thick, and relatively flat areas found within the shell of the *Strombus gigas*. Our observations show a significant correlation between microstructure and indenter geometry, with the alignment of the crossed lamellar system found in gastropods, the β=-45°and β=45° alignment, provides a significant resistance to penetration (hardness), superior maximum load before critical failure, and invariance with indenter rotation when compared to the β=-

0°/90°. Additionally we only examined two parameters within the crossed lamellar system and did not vary the 1st order tilt angle. Tilting of the 1st order lamellae is partially responsible for the many previously confusing descriptions of the crossed lamellar microstructure. The significant variation of measured mechanical properties with gastropod shells and other highly architectured biominerals implies a great need to couple nanoindentation and microstructural morphological evaluation techniques to further our understanding of the indentation mechanics of complex biomineral systems. However, obtaining sections that are uniform and well aligned can be quite challenging due to the geometric limitations of many systems and must be carefully controlled and verified.

References

1. C. Salinas, D. Kisailus, Fracture Mitigation Strategies in Gastropod Shells. *Jom-Us* **65**, 473-480 (2013).

2. S. Kamat, H. Kessler, R. Ballarini, M. Nassirou, A. H. Heuer, Fracture mechanisms of the Strombus gigas conch shell: II - Micromechanics analyses of multiple cracking and large-scale crack bridging. *Acta Mater* **52**, 2395-2406 (2004).

3. S. Kamat, X. Su, R. Ballarini, A. H. Heuer, Structural basis for the fracture toughness of the shell of the conch Strombus gigas. *Nature* **405**, 1036-1040 (2000).

4. L. T. KuhnSpearing *et al.*, Fracture mechanisms of the Strombus gigas conch shell: Implications for the design of brittle laminates. *J Mater Sci* **31**, 6583-6594 (1996).

5. L. Romana *et al.*, Use of nanoindentation technique for a better understanding of the fracture toughness of Strombus gigas conch shell. *Materials Characterization* **76**, 55-68 (2013).

6. L. K. Grunenfelder *et al.*, Stress and Damage Mitigation from Oriented Nanostructures within the Radular Teeth ofCryptochiton stelleri. *Advanced Functional Materials* **24**, 6093-6104 (2014).

7. H. Z. Li, Y. H. Yue, X. D. Han, X. D. Li, Plastic Deformation Enabled Energy Dissipation in a Bionanowire Structured Armor. *Nano Lett* **14**, 2578-2583 (2014).

8. F. Barthelat, H. Tang, P. Zavattieri, C. Li, H. Espinosa, On the mechanics of mother-of-pearl: A key feature in the material hierarchical structure. *J Mech Phys Solids* **55**, 306-337 (2007).

9. F. Barthelat, C. M. Li, C. Comi, H. D. Espinosa, Mechanical properties of nacre constituents and their impact on mechanical performance. *J Mater Res* **21**, 1977-1986 (2006).

10. F. Auricchio, R. L. Taylor, Two material models for cyclic plasticity: nonlinear kinematic hardening and generalized plasticity. *International Journal of Plasticity* **11**, 65-98 (1995).

11. C. Kearney *et al.*, Nanoscale Anisotropic Plastic Deformation in Single Crystal Aragonite. *Phys Rev Lett* **96**, (2006).

12. H. Z. Li, Z. H. Xu, X. D. Li, Multiscale hierarchical assembly strategy and mechanical prowess in conch shells (Busycon carica). *Journal of structural biology* **184**, 409-416 (2013).

13. H. D. Espinosa, P. D. Zavattieri, A grain level model for the study of failure initiation and evolution in polycrystalline brittle materials. Part II: numerical examples. *Mech Mater* **35**, 365-394 (2003).

14. Y.-T. Cheng, C.-M. Cheng, Scaling, dimensional analysis, and indentation measurements. *Materials Science and Engineering: R: Reports* **44**, 91-149 (2004).

15. W. C. Oliver, G. M. Pharr, An Improved Technique for Determining Hardness and Elastic-Modulus Using Load and Displacement Sensing Indentation Experiments. *J Mater Res* **7**, 1564-1583 (1992).

16. A. K. Dastjerdi, M. Pagano, M. Kaartinen, M. McKee, F. Barthelat, Cohesive behavior of soft biological adhesives: experiments and modeling. *Acta biomaterialia* **8**, 3349-3359 (2012).

17. A. K. Dastjerdi, E. Tan, F. Barthelat, Direct measurement of the Cohesive Law of adhesives using a rigid double cantilever beam technique. *Exp Mech* **53**, 1763-1772 (2013).

18. L. Han, L. Wang, J. Song, M. C. Boyce, C. Ortiz, Direct quantification of the mechanical anisotropy and fracture of an individual exoskeleton layer via uniaxial compression of micropillars. *Nano Lett* **11**, 3868-3874 (2011).

19. T. L. Anderson, *Fracture mechanics: fundamentals and applications*. (CRC press, 2005).

20. R. Rabiei, S. Bekah, F. Barthelat, Nacre from Mollusk Shells: Inspiration for High-performance Nanocomposites. *Rsc Green Chem Ser*, 113-149 (2012).

21. F. Barthelat, H. D. Espinosa, An experimental investigation of deformation and fracture of nacre-mother of pearl. *Exp Mech* **47**, 311-324 (2007).

22. J. Currey, J. Taylor, The mechanical behaviour of some molluscan hard tissues. *J Zool* **173**, 395-406 (1974).

23. A. Jackson, J. Vincent, R. Turner, The mechanical design of nacre. *Proceedings of the Royal society of London. Series B. Biological sciences* **234**, 415-440 (1988).

24. M. Suzuki, H. Kim, H. Mukai, H. Nagasawa, T. Kogure, Quantitative XRD analysis of {110} twin density in biotic aragonites. *Journal of structural biology* **180**, 458-468 (2012).

25. L. Li, C. Ortiz, Pervasive nanoscale deformation twinning as a catalyst for efficient energy dissipation in a bioceramic armour. *Nat Mater* **13**, 501-507 (2014).

4. Biomimetic Composites & Future Work

Abstract

Light-weight and high strength fiber reinforced plastics have revolutionized the automobile and aerospace industries by decreasing weight while improving performance. However, reinforced plastics still suffer issues with catastrophic failure after being damaged. The crossed lamellar microstructure is a biological fiber reinforced composite that over 400 million years of evolution has managed to increase the fracture toughness of the calcium carbonate within gastropod shells by over 3 orders of magnitude compared to abiotic mineral. This remarkable toughness allows the shell to fail gracefully, giving the animal a greater chance at surviving an attack by a predator. We examine methods to fabricate mimics of the crossed lamellar structure using a conventional epoxy and glass fiber system.

4.1. Introduction

With the introduction of fiber reinforced Bakelite in 1907, applications for fiber reinforced plastics (FRP) have expanded greatly. Due to the high material and manufacturing cost, fiber reinforced plastics were initially limited to spacecraft and high performance military fighter aircraft. Reductions in manufacturing costs have allowed fiber reinforced plastics to expand into other markets and are now increasingly found in recreational sporting equipment, consumer automobiles, and passenger airliners. While FRPs typically have excellent strength to weight ratios, their durability is quite low and FRP components can experience a significant reduction in mechanical properties after minor damage. In order to be safely

implemented into use for the general public, the next generation of fiber reinforced plastics for automobiles or sports equipment will need to be strong, light weight, and impact resistant.

Fiber reinforced plastics combine a relatively weak and low weight plastic matrix with long high strength fibers that act as the reinforcement phase. The resulting material combines the properties of the matrix and reinforcing phases to yield composites that are typically light-weight and possess relatively high stiffness. The mechanical properties of the reinforcing fibers are highly anisotropic, resisting tensile forces acting along the length of the fiber, while providing little to no resistance to forces not along the fiber's long axis. To overcome this highly anisotropic behavior, reinforcing fibers are woven into 2-dimensional fabrics that contain multiple fiber directions. Composite parts are formed by arranging multiple plies of the woven fiber fabrics into a mold cavity and infusing the spaces within the fabric with a plastic matrix.

Undamaged fiber reinforced plastic have exceptionally high strength for their weight, once damaged the mechanical properties rapidly decrease once fractures have been initiated. Without a mechanism to arrest the fractures, the material will fail catastrophically. The reinforcement fibers are only to resist fractures that act on the fiber in tension; due to the highly anisotropic properties, they provide little to no reinforcement in perpendicular directions. The fracture toughness of fiber reinforced plastic can be increased by incorporating microstructural features to prevent or resist the growth of fracture.

4.2. Materials and Methods

Fiber reinforced composites were fabricated using an out of oven vacuum bagging method. Multiple plies of biaxial stitched glassed fiber reinforcement (Saertex 450, Fibre Glast USA) were infused with epoxy resin (Fibre Glast system 2000, Fibre Glast USA). Composites were fabricated on steel mold plates and were covered with a nylon bagging material. Vacuum was pulled on the mold to remove air and compact the fiber / resin system (Figure 4-1). Panels were cured for 24hr at 25°C. Cured panels were cut into sections using a water cooled saw equipped with a diamond bonded blade (MK101 MK-Diamond, USA). Sections were then rebounded with differing orientations using a Cyanoacrylate adhesive (Loctite USA).

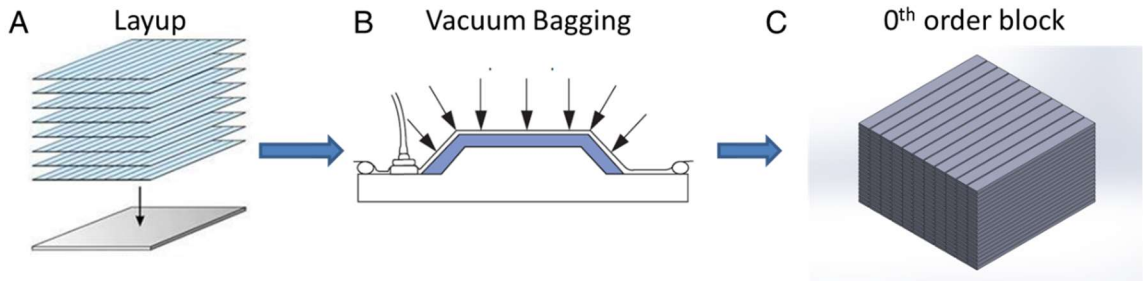

Figure 4-1 Layup procedure for vacuum bagging of bulk composites. Reinforcement and resin and stacked on a mold plate (A). The layup is sealed in a nylon bag, and the air is evacuated using a vacuum pump, this causes the reinforcement to become more compact and removes trapped gasses from within the fabric (B). The resulting composite is 0^{th} order block, or a bulk layer to be used for further sectioning (C).

Mechanical test specimens were prepared for 3pt-bend from bonded glass fiber and epoxy composites, according to ASTM D790 (*1*). Rectangular bars were tested with an Instron Universal Testing Machine (Instron USA), with a steel 3pt

bend apparatus. Load and displacement data were recorded in real time using a laboratory computer.

4.3. Results & Discussion

From the initial bi-axial epoxy and fiber composite there are four types of sections that can be produced depending on the direction on how the substrate is cut. We have labeled these sections 1A, 1B, 2A, and 2B, these sections can be divided into two sets of groups. The first group is determined by the angle between the fibers and the long axis of the section (2) 0/90° and (1) +45/-45°. The second is the orientation of the fibers in-to (B) and out of the plane (A) of the large surface of the cut section (Figure 4-2).

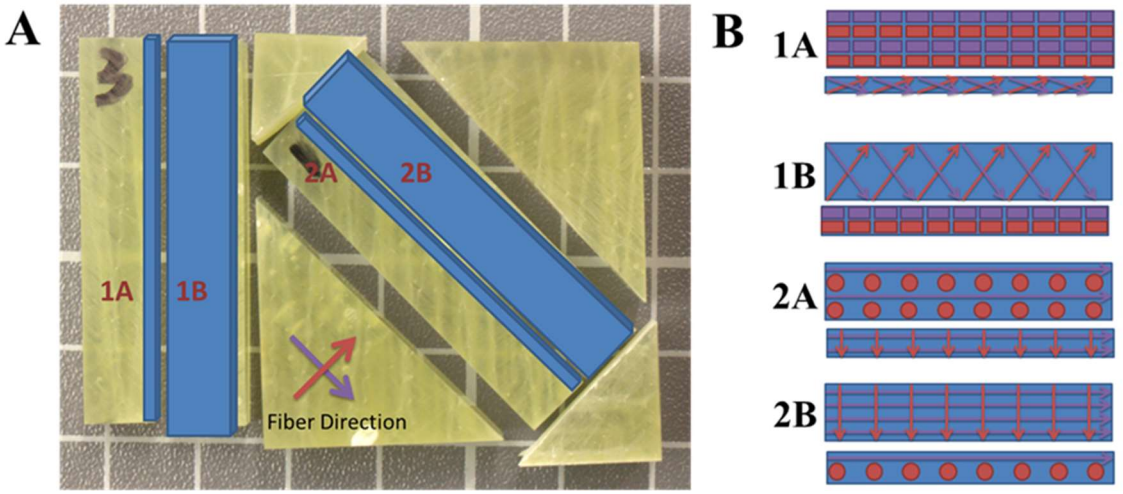

Figure 4-2 Bulk bi-axial fiberglass and epoxy composite from which the different sections are extracted, blue models show the orientation of the different sections (A). Top and side views of the different possible sections (B).

Initial mechanical testing of the bonded composites with differing structures, revealed that the 2A-2B combination had a superior strength, modulus, and fracture energy than the other samples (Figure 4-3). Most of the samples began to fail after 2.5% strain. At this strain, pop-in events are recorded in the load and

displacement data, and correspond to fractures forming and growing within the material, relieving stress that has accumulated. The work of fracture of the 2A-2B sample is more than 4 times greater than the other samples. The difference in the mechanical behavior is due to the geometry of the reinforcement materials, with respect to the loading conditions. The 2A-2B sample has long fibers traversing the length of the lower face of the sample, which is loaded in tension during 3pt-bend. Delamination between bonded sections was not observed in any of the tested specimen, nor was their catastrophic failure near or around this interface.

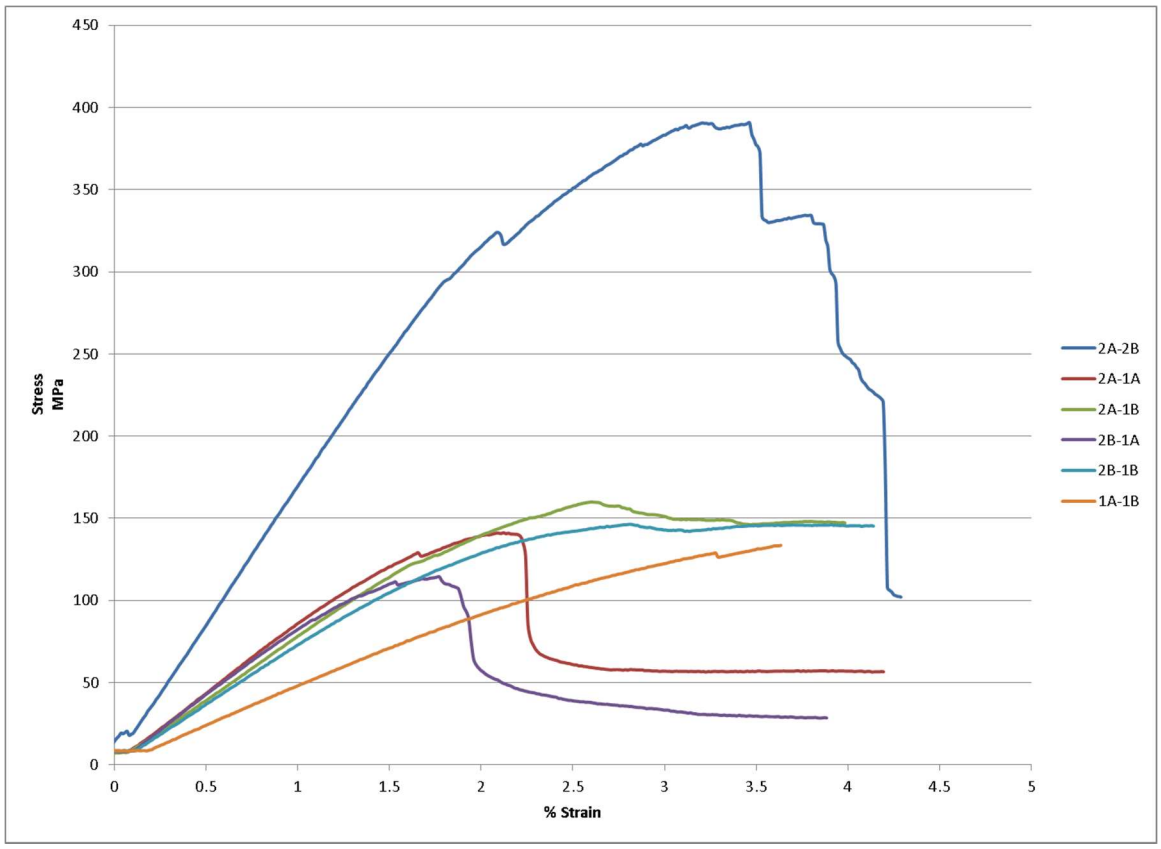

Figure 4-3 Plot of stress vs % strain for bonded bi-axial composite combinations. The initial linear slope of the stress-strain curve corresponds to the bending modulus. The maximum load obtained before failure is the strength. The work of fracture can be qualitatively determined from the area under the stress-strain curve.

The initial success of the bonded composites suggests that further investigation of bonded, sectioned, and re-bonded composites is feasible. There are a number of potential areas for further initial investigation, such as the types of interfaces and the number of layers in the resulting panel or part. Additional interfaces can be introduced within one of the layers of the bi-layer composite. These additional interfaces would occur during the fabrication of the 0th order block (Figure 4-1C) by fabricating and curing single ply panels, or the equivalent of crossed lamellar "1st order" layers. These one-ply panels would then be bonded to form a 0th order block with 1st order interfaces. The strength of the 1st order interfacial bond provides additional design parameters which can be tuned to influence the fracture mechanics of the layer and the bulk, as is seen in the crossed lamellar shell (*2, 3*). The interface between 1st order layers, allows for the distribution of stress between adjacent layers (Figure 4-4).

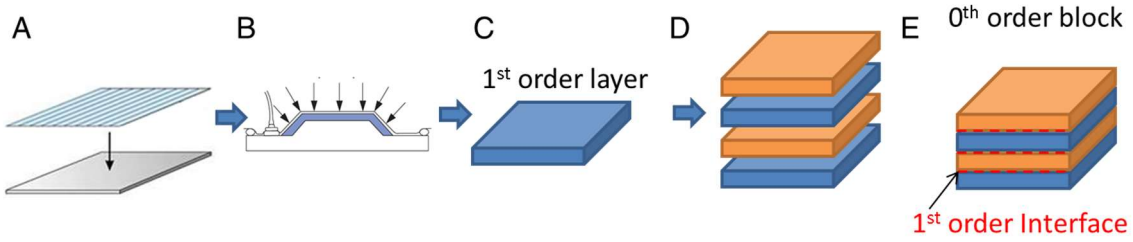

Figure 4-4 Fabrication method for 0th order block with 1st order interface. Layup (A), vacuum bagging (B). Individual 1st order layers (C), are stacked and bonded (D), resulting in a 0th order block (E).

The addition of 1st order laminates, allows for the direction of the laminate to be altered in the fabrication of the 0th order block (Figure 4-5). The choice of laminate directions will depend on the loading conditions**.** In the *Strombus gigas* shell, the laminates are stacked along the length of the 0th order lamellae (Figure

4-5D). When the material is loaded in tension, numerous fractures are formed at the interface between 1st order lamellae (*4*). Some of the potential sectioning-bonding schemes become redundant when the geometery of the test specimen is changed. For instance laminates formed by bonding along the width (Figure 4-5.B) and laminates bonded along the lamellae thickness (Figure 4-5.D), become identical if the lamella lengthis equal to the width.

Following design cues from crossed lamellar shells, the addition of a third 0th order lamellae is a natural progression after the evaluation of the bi-layer designs (Figure 4-6). Cracks are redirected and arrested at in the interface between perpendicular 0th order layers (*5*). The fabrication of tri-layer composite is the same as a bi-layer composite, with the addition of one more bonding step.

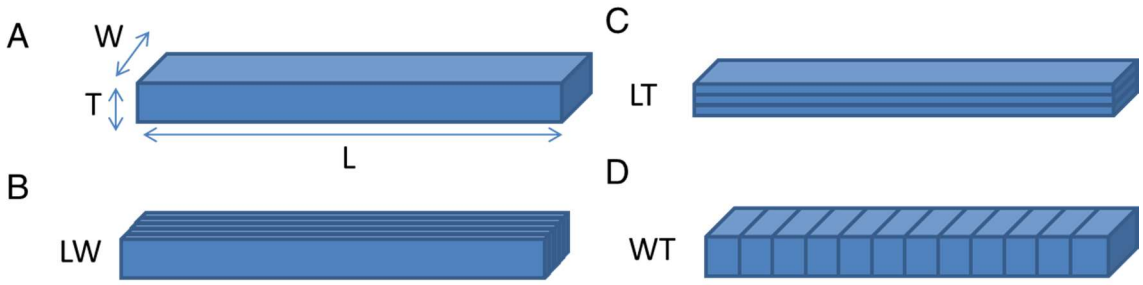

Figure 4-5 Different basic 1st order directions within a 0th order block. No interfaces (A). Laminates in the width direction (B), laminates in the thickness direction (C), and laminates in the length direction (D).

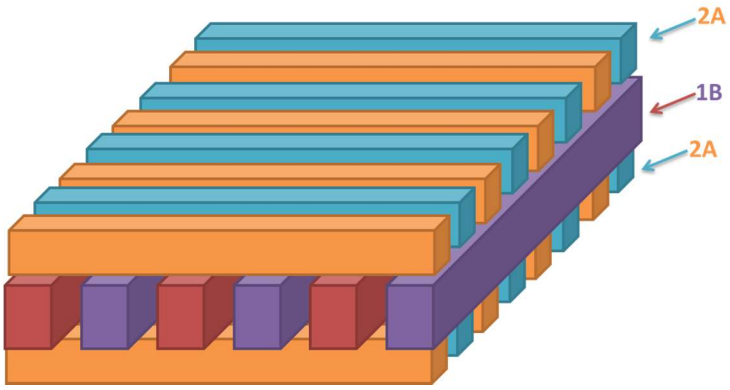

Figure 4-6 Proposed tri-layer composite with alternating perpendicular laminate direction. Each layer is composed of one of the primitive types defined in Figure 4-2

4.1. Conclusion

The crossed lamellar structure from gastropod shells is a biological fiber reinforced composite that over hundreds of millions of years, evolved a unique and complex architecture that has a toughness three orders of magnitude greater than its constituent materials. Reproducing this crossed lamellar structure using conventional laminate processing techniques is not feasible due to the multiple fiber and laminate directions. However, through the technique of sectioning and bonding, it is possible to make panels that mimic the design of the gastropod crossed lamellar structure.

5. References

1. ASTM, in *Test Methods for Flexural Properties of Unreinforced and Reinforced Plastics and Electrical Insulating Materials*. (ASTM International, 2010).

2. S. Kamat, X. Su, R. Ballarini, A. H. Heuer, Structural basis for the fracture toughness of the shell of the conch Strombus gigas. *Nature* **405**, 1036-1040 (2000).

3. S. Kamat, H. Kessler, R. Ballarini, M. Nassirou, A. H. Heuer, Fracture mechanisms of the Strombus gigas conch shell: II - Micromechanics analyses of multiple cracking and large-scale crack bridging. *Acta Mater* **52**, 2395-2406 (2004).

4. J. D. Currey, A. J. Kohn, Fracture in Crossed-Lamellar Structure of Conus Shells. *J Mater Sci* **11**, 1615-1623 (1976).

5. L. T. KuhnSpearing *et al.*, Fracture mechanisms of the Strombus gigas conch shell: Implications for the design of brittle laminates. *J Mater Sci* **31**, 6583-6594 (1996).